GENERALIZED MODELING OF METAL CUTTING MECHANICS

by

MUSTAFA KAYMAKCI
M.Sc. Koc University, Turkey, 2007

A THESIS SUBMITTED IN PARTIAL FULFILLMENT OF
THE REQUIREMENTS FOR THE DEGREE OF

MASTER OF APPLIED SCIENCE

in

The Faculty of Graduate Studies
(Mechanical Engineering)

THE UNIVERSITY OF BRITISH COLUMBIA
(Vancouver)

August 2009

Abstract

Metal cutting is the most commonly used manufacturing process for producing parts with final dimensions. The aim of engineering science is to model the physics of the process which allows the simulation of part machining operations ahead of costly trials. There is a need to develop generalized models of cutting process which is applicable to various tool geometries and cutting processes in order to simulate machining of industrial parts in virtual environment. This thesis presents a generalized mathematical model which can be used to predict turning, drilling, boring and milling processes.

The tool geometry is adopted from ISO 13399 standards. The rake face of the tool is mathematically modeled from ISO13399 model by considering tool geometry, engagement with the workpiece, feed and speed directions of cutting motion. Various geometric features of the tool, such as chamfer, nose radius, and cutting edge angles, are considered in developing coordinate transformation models between the machine motion and tool coordinate systems.

The cutting forces on the rake face are defined in the direction of chip flow and perpendicular to the rake face. The cutting force coefficients in the two directions are either identified mechanistically by conducting experiments specific to the tool geometry, or using orthogonal to oblique transformation of shear angle, average friction angle and shear stress. The friction and normal forces on the rake face are transformed to both stationary and rotating tool coordinate systems defined on the machine tool.

Table of Contents

Abstract ii

Table of Contents ii

List of Tables v

List of Figures vi

Acknowledgements xiii

Nomenclature x

1. Introduction 1

2. Literature Survey 4

    2.1 Overview 4

    2.2 Mechanics of Metal Cutting 4

    2.3 Cutting Force Models 6

        2.3.1 Orthogonal Cutting 6

        2.3.2 Forces in Turning 7

        2.3.3 Forces in Milling 10

    2.4 Inserted Cutters 12

    2.5 Generalized Mechanics of Machining 13

3. ISO Cutting Tool Geometry… 14

    3.1 Overview 14

    3.2 Planes 14

    3.3 Points and Angles 16

    3.4 Dimensional Quantities 20

    3.5 Insert Shapes 21

        3.5.1 Equilateral Equiangular Insert 21

        3.5.2 Equilateral Nonequiangular Insert 22

3.5.3 Nonequilateral Equiangular Insert 22
3.5.4 Nonequilateral Nonequiangular Insert 22
3.5.5 Round Insert 23
3.6 Tool Coordinate Frames and Transformations 24
3.6.1 Turning Operations 25
3.6.2 Transformation of Rotary Tools 31
3.7 Summary 38
4. Generalized Geometric Model of Inserted Cutters 39
4.1 Overview 39
4.2 Mathematical Modeling of an Insert 40
4.3 Tool Coordinate Frames and Transformations 42
4.3.1 Frame $\boldsymbol{F0}$ to Frame $\boldsymbol{F1}$ Rotation 43
4.3.2 Frame $\boldsymbol{F1}$ to Frame $\boldsymbol{F2}$ Rotation 44
4.3.3 Frame $\boldsymbol{F2}$ to Frame $\boldsymbol{F3}$ Rotation 45
4.4 Mathematical Relationships between Angles 46
4.4.1 Normal Rake Angle 46
4.4.2 True Cutting Edge Angle 47
4.4.3 Inclination (Helix) Angle 48
4.5 Examples 51
4.5.1 Rectangular Insert with Corner Radius 51
4.5.2 Rectangular Insert with Corner Chamfer 59
4.5.3 Rhombic Turning Insert 63
4.6 Summary 67
5. Generalized Mechanics of Metal Cutting 68
5.1 Overview 68
5.2 Rake Face Based General Force Model 68
5.3 Identification of Specific Cutting Coefficients 72

5.3.1 Orthogonal to Oblique Transformation 72
5.3.2 Mechanistic Identification 79
5.4 Cutting Force Simulations and Validations 91
5.4.1 Turning Process Simulations 91
Rhombic (ISO Style C) Insert: 95
5.4.2 Milling Process Simulations 102
5.5 Summary 115
6. Conclusions 116
Bibliography 118

List of Tables

Table 3-I: Summary of Angles for Definition of Orientation of Cutting Edge and Rake Face. 20
Table 3-II: Insert Shapes Defined in ISO 13399. 23
Table 4-I: Inputs Used in the Model. 51
Table 4-II: Inputs Used in the Analysis of the Insert with Chamfer. 59
Table 4-III: Inputs for the Rhombic Turning Insert. 63
Table 5-I: Cutting Coefficients and Tool Geometry Used in the Analysis. 86
Table 5-II: Comparison of the Methods for the Solution of Oblique Shear Parameters. 88
Table 5-III: Orthogonal Turning Validation Experiments Cutting Conditions. 93
Table 5-IV: Tool Geometry and Cutting Conditions for Rhombic Insert. 95
Table 5-V: Tool Geometry and Cutting Conditions for Square Insert. 100

List of Figures

Figure 2-1: Orthogonal Cutting Process [5]. 4
Figure 2-2: Illustration of Cutting Force Components [12][5]. 5
Figure 2-3: Turning Operation Using a Tool with a Nose Radius and Colwell's Approach..... 8
Figure 2-4: Different Approaches for Predicting Chip Flow Direction: (a) Colwell, (b) Okushima and Minato, (c) Young et al. 9
Figure 3-1: Planes Defined in ISO 3002 and ISO 13399. 16
Figure 3-2: Illustration of the Cutting Reference Point (CRP). 17
Figure 3-3: Demonstration of Tool Angles in ISO Standards for a Turning Tool. 19
Figure 3-4: Dimensional Quantities Defined in the ISO Standards. 21
Figure 3-5: Mechanics of Oblique Cutting Process. 25
Figure 3-6: RTA and the Machine Coordinate Systems on a Lathe. 27
Figure 3-7: Cutting Edge Coordinate System along with the RTA Coordinate System. 28
Figure 3-8: Rake Face Coordinate System (System 3): Rotation around the $\boldsymbol{YII}$ Axis by the Amount of Rake Angle $\boldsymbol{\gamma n}$. 29
Figure 3-9: Chip Flow Coordinate System (System 4): Rotation around the $\boldsymbol{XIII}$ Axis by the Amount of Chip Flow Angle $\boldsymbol{\eta}$. 30
Figure 3-10: Illustration of System * on a Rotary Tool with Four Flutes. 32
Figure 3-11: Transformation between System 1 and System *. 34
Figure 3-12: Transformation between System 1 and System 2 for Rotary Tools. 35
Figure 3-13: Transformation between Rake Face Coordinate System (System 3) and Cutting Edge Coordinate System (System 2). 36
Figure 3-14: Representation of the Chip Flow Coordinate System on a Milling Tool. .. 37
Figure 4-1: Local Coordinate Systems and Cutting Reference Points on Different Inserts. 40
Figure 4-2: Control Points on a Parallelogram Insert. 41
Figure 4-3: Frame $\boldsymbol{F0}$ to Frame $\boldsymbol{F1}$ Rotation. 43
Figure 4-4: Frame $\boldsymbol{F1}$ to Frame $\boldsymbol{F2}$ Rotation. 44

Figure 4-5: Frame $\boldsymbol{F2}$ to Frame $\boldsymbol{F3}$ Rotation. 45
Figure 4-6: Derivation of Normal Rake Angle. 47
Figure 4-7: Derivation of the True Cutting Edge Angle. 48
Figure 4-8: Definition of Frame $\boldsymbol{Fs}$ and Frame $\boldsymbol{F0}$ to Frame $\boldsymbol{Fs}$ Rotation. 49
Figure 4-9: Definition of the Inclination (Helix) Angle. 50
Figure 4-10: Illustrations of the Insert and the Cutter Body [55]. 51
Figure 4-11: Analytical Model of an Insert with a Corner Radius and Wiper Edge. 52
Figure 4-12: Control Points of the Insert before the Rotations. 54
Figure 4-13 : Control Points of the Insert after the Rotations. 55
Figure 4-14: CAD Model of the Insert. 56
Figure 4-15: Change of Local Radius along the Tool Axis. 57
Figure 4-16: Change in Normal Rake Angle along the Tool Axis. 58
Figure 4-17: Change in Helix Angle along the Tool Axis. 58
Figure 4-18: Catalogue Figure of the Insert Taken from Sandvik Coromant [55]. 59
Figure 4-19: Illustration of Control Points and Dimensions for an Insert with Chamfer. 60
Figure 4-20: Change in the Local Radius along the Tool Axis for a Chamfered Insert. . 61
Figure 4-21: Change in Normal Rake Angle along the Tool Axis. 62
Figure 4-22: Change in Helix Angle along the Tool Axis. 62
Figure 4-23: Catalogue Figures of the Turning Insert [55]. 63
Figure 4-24: Control Points of the Rhombic Turning Insert. 64
Figure 4-25: Position of the Cutting Edge for a Rhombic Turning Insert. 65
Figure 4-26: Change in the Normal Rake Angle along the Cutting Edge. 66
Figure 4-27: Change in the Helix Angle along the Cutting Edge. 66
Figure 5-1: Mechanics of Oblique Cutting [11]. 69
Figure 5-2: Summary of the Proposed Mechanistic Approach. 71
Figure 5-3: Shear Plane Area Comparison: Orthogonal Cutting (Left) and Oblique Cutting (Right). 73
Figure 5-4: Cutting Forces, Velocities, and Angles in Oblique Cutting [11]. 74
Figure 5-5: Illustration of angle $\boldsymbol{\theta n}$. ($\boldsymbol{FN}, \boldsymbol{FuN}$, and $\boldsymbol{FvN}$ Are Projections of Forces onto Normal Plane). 75
Figure 5-6: Summary of the Classical Approach in Cutting Coefficient Identification. . 78

Figure 5-7: Block Diagram of the Iterative Method to Enhance the Theoretical Models. 84
Figure 5-8: Results of Helix Angle Predictions for Ti6Al4V..... 86
Figure 5-9: Results of Helix Angle Predictions for Al7075. 87
Figure 5-10: Theoretical Identification Procedure. 89
Figure 5-11: Effect of Chip Thickness on the Cutting Coefficients. 90
Figure 5-12: Effect of Chip Thickness on the Chip Flow Angle. 90
Figure 5-13: Workpiece and 3- Component Dynamometer Fixed to Turret for Cutting Tests. 92
Figure 5-14: Sample Output Screen in CutPro 8.0 for Cutting Forces. 92
Figure 5-15: Forces simulated and measured for an orthogonal tool with 75° cutting edge angle for V=100 m/min. 94
Figure 5-16: Forces simulated and measured for an orthogonal tool with 75° cutting edge angle for V=150 m/min. 94
Figure 5-17: Illustration of Insert and the Holder Body [55]. 95
Figure 5-18: Geometric Control Points of a Rhombic Turning Insert..... 97
Figure 5-19: Comparison of Measured and Calculated Forces for the Rhombic Tool while the Width of Cut is 2 mm..... 99
Figure 5-20: Comparison of Measured and Calculated Forces for the Rhombic Tool while the Width of Cut is 4 mm..... 99
Figure 5-21: Illustration of Insert and the Holder Body [55]. 101
Figure 5-22: Comparison of Measured and Calculated Forces for the Square Insert while the Width of Cut is 2 mm. 101
Figure 5-23: Comparison of Measured and Calculated Forces for the Square Insert while the Width of Cut is 4 mm. 102
Figure 5-24: Workpiece and 3-Component Dynamometer Fixed to Machine Table for Cutting Tests. 103
Figure 5-25: Illustration of the Experimental Setup for Measurement of Cutting Forces. 104
Figure 5-26: 25 mm Diameter Shoulder End Mill from Sandvik Coromant [55]. 104
Figure 5-27: Illustration of Control Points for the Shoulder Milling Insert. 106

Figure 5-28: Measured and Predicted Forces for Al7050 Half Immersion Up-Milling. 107
Figure 5-29: Measured and Predicted Forces for Al7050 Slot Milling. 108
Figure 5-30: 20 mm Diameter Bull-Nose Mill from Sandvik Coromant [55]. 109
Figure 5-31: Measured and Predicted Forces for Al7050 Half Immersion Up-Milling. 110
Figure 5-32: Measured and Predicted Forces for Al7050 Slot Milling. 111
Figure 5-33: 20 mm Diameter Ball-End Mill from Sandvik Coromant [55]. 112
Figure 5-34: Control Points of a Round Milling Insert 113
Figure 5-35: Measured and Predicted Forces for Al7050 Half Immersion Up-Milling. 114
Figure 5-36: Measured and Predicted Forces for Al7050 Slot Milling. 115

Nomenclature

ϕ_c	:	Orthogonal shear angle
ϕ_n	:	Normal shear angle
β_a	:	Friction angle
τ_s	:	Shear Stress
A_s	:	Shear plane area
$\phi_i, \theta_n, \theta_i$	:	Oblique angles
F	:	Resultant force
F_t	:	Tangential force
F_f	:	Feed force
F_r	:	Radial force
F_x	:	Force in X direction
F_y	:	Force in Y direction
F_z	:	Force in Z direction
F_u	:	Friction force on the rake face
F_v	:	Normal force on the rake face
F_s	:	Shear force on the shear plane
F_n	:	Normal force on the shear plane
K_{tc}	:	Tangential cutting coefficient
K_{rc}	:	Radial cutting coefficient
K_{ac}	:	Axial cutting coefficient
K_{te}	:	Tangential edge coefficient
K_{re}	:	Radial edge coefficient
K_{ae}	:	Axial edge coefficient
K_{uc}	:	Friction cutting coefficient
K_{vc}	:	Normal cutting coefficient
K_{ue}	:	Friction edge coefficient
K_{ve}	:	Normal edge coefficient
K_t	:	Tangential cutting pressure
K_f	:	Feed cutting pressure

K_r	:	Radial cutting pressure
m_1 & m_2	:	Cutting constants
h	:	Uncut chip thickness
a	:	Depth of cut
b	:	Width of cut
b_{eff}	:	Effective width of cut
c	:	Feed rate
V_c	:	Cutting speed
P_t	:	Cutting power
dA_c	:	Differential chip load
$\bar{A}_c$	:	Average chip load
dS	:	Differential cutting edge length
dA	:	Differential cutting edge area
N_f	:	Number of cutting edges
K	:	Total number of discrete points along the cutting edge
ϕ	:	Immersion angle
θ_{st}	:	Tool entry angle
θ_{ex}	:	Tool exit angle
κ_r	:	Cutting edge angle
ε_r	:	Tool included angle
ψ_r	:	Approach angle
λ_s	:	Inclination (oblique) angle
K_ε	:	Corner chamfer angle
γ_n	:	Normal rake angle
γ_f	:	Radial rake angle
γ_p	:	Axial rake angle
η	:	Chip flow angle
$\bar{\eta}$	:	Average chip flow angle
P_r	:	Tool reference plane
P_f	:	Assumed working plane

P_p	:	Tool back plane
P_s	:	Tool cutting edge plane
P_n	:	Cutting edge normal plane
P_m	:	Wiper edge normal plane
A_γ	:	Rake face
CRP	:	Cutting reference point
D_c	:	Cutting Diameter
L	:	Insert length
b_s	:	Wiper edge length
iW	:	Insert width
bch	:	Corner chamfer length
r_ε	:	Corner radius
$\vec{P_i}$	:	Control Points
$\vec{u}$	:	Unit vector from center of the arc to circumference
$\vec{n}$	:	Unit vector perpendicular to arc
C	:	Center of the arc
$\overrightarrow{Z_{1.2}}$	:	Point on the tool axis

Acknowledgements

I am indebted to my supervisor, Prof. Yusuf Altintas, for the considerable guidance, support, and encouragement he has provided me throughout the duration of my studies at the University of British Columbia. I also wish to thank Dr. Doruk Merdol, who co-supervised much of this research, for his time and for teaching me many things.

I also would like to thank Dr. Farrokh Sassani and Dr. Steve Feng for reading this thesis and involving in my thesis committee.

It is an honor to work in an exceptionally professional environment in the Manufacturing Automation Laboratory. I have enjoyed every moment I spent in and out of the lab with my colleagues. They are not just colleagues, but also good friends. I have lots of good memories I will remember for the rest of my life. I also would like to thank my friends in Vancouver for their support and friendship.

Finally, I would like to thank my brother Orkun Kaymakci, my father Emin Kaymakci, and especially my mother Hamidiye Ozberk for their life-long love, for the kind of encouragement and support they have provided me throughout my entire education life, and for their absolute confidence in me. This thesis as well as all my previous success is dedicated to my family.

1. Introduction

In terms of operations that take place in industry, metal cutting is the most common manufacturing method in producing final shapes of mechanical parts with tight tolerances and complex shapes. The main metal cutting processes can be listed as turning, milling, boring, and drilling.

Metal cutting operations can be conducted manually or automatically by the help of Computer Numerical Control (CNC) tools. The motion of the machine tool on a CNC is controlled by the NC commands which are generated on computer – aided design/ computer – aided manufacturing (CAD/CAM) systems. The productivity and the output quality depends on the preparation of NC programs, process planner, cutting conditions, workpiece material, cutter geometry, cutter material, machine tool rigidity and the performance of the CNC system. Economical and efficient manufacturing in metal cutting operations are vital in order to produce parts with desired accuracy and low cost. Understanding the mechanics of the metal cutting process assists in avoiding damages to the tool, machine and workpiece while improving productivity and accuracy.

Cutting tools with replaceable inserts are widely used in machining industry. Insert geometries can vary depending on the cutting operation and workpiece material. While all turning tools are inserts, milling cutters use either inserts distributed on the cutter body or they are ground from solid carbides. Due to the geometric complexities of inserts with poorly defined rake face geometry, it is difficult to accurately model mechanics of the cutting operation. As a result, an accurate cutting force model which can include various has been a challenge.

Current literature focuses to determine separate mechanics models for each cutting process and even for each different cutter. In other words, researchers aimed to develop dedicated cutting models for turning, boring, drilling, and milling operations having different tool geometries. However, by understanding the fundamentals of metal cutting mechanics, it must be possible to develop a unified-generalized process model that can

predict the cutting forces for a wide spectrum of machining operations practiced in industry.

This thesis focuses on developing a generalized cutting mechanics model that can be applicable to most cutting processes. Cutting forces are first modeled on the rake face of the tool as friction and normal loads. The friction and normal forces are transformed to tool coordinate system. An improved and enhanced inserted cutter model has been developed based on the previous studies of Engin and Altintas [1]. Analytical model for all insert geometries defined in ISO 13399 standards have been derived. The forces are further transformed from the tool to cutting operation coordinate system to predict cutting forces, torque and power for various machining operations and cutting conditions.

The thesis is organized as follows;

Chapter 2 presents necessary background and literature review on metal cutting research. Cutting mechanics, previous models for chip thickness, chip flow models, as well as prediction of cutting forces for different operations are discussed. Previous geometric models of inserted cutters are summarized and generalization of metal cutting mechanics is reviewed.

The geometric parameters of the cutting tools are defined according to ISO 13399 standards in Chapter 3. The reference planes and points required to describe the cutting angles are presented. Angular and dimensional quantities are considered to model an extensive variety of cutting tool geometries. The coordinate transformations needed to describe the cutting forces on rake face of the tool are presented.

The geometric modeling of inserted cutters is presented in Chapter 4. Using the geometric identities described in Chapter 3, geometric control points are calculated analytically at the local coordinate system of the insert, which is placed on the cutter body using the orientation angles. Physical angles of the cutter required for cutting mechanics models are calculated with sample illustrations.

The generalized modeling of cutting forces using friction and normal forces on the rake face of the cutter is presented in Chapter 5. The proposed mechanics model is

compared with the current force models found in the literature. In addition to cutting forces, material model and calibration methods are also discussed and the transformations between the models are summarized. Using the geometric modeling of inserted tools which is described in Chapter 4, experimental validations of the model are presented. Simulations and measurements are presented for turning and milling operations for various types of inserted cutters and cutting conditions.

The thesis is concluded in Chapter 6 with the summary of contributions and future research.

2. Literature Survey

2.1 Overview

A literature review of past research on modeling of cutting tool geometry and mechanics are presented. The distribution of chip along the cutting edge is discussed, and the corresponding approaches in predicting the cutting forces are presented.

2.2 Mechanics of Metal Cutting

Mechanics of metal cutting has been a subject of research for the last 60 years [2][3][4] [5]. The process of mechanics are affected by parameters such as feed rate, depth of cut, cutting speed, cutting edge angle, rake angle, helix angle, and workpiece material [6]. Researchers have been trying to establish a relationship between these parameters and process mechanics. The early work done by Merchant [7][8] has been a foundation used in the modeling of cutting forces [9][10]. Merchant's model is based on the concept of a steady process in which a chip is produced by shearing a strip of uncut metal continuously and uniformly, and the deformation of the chip takes place along a shear plane.

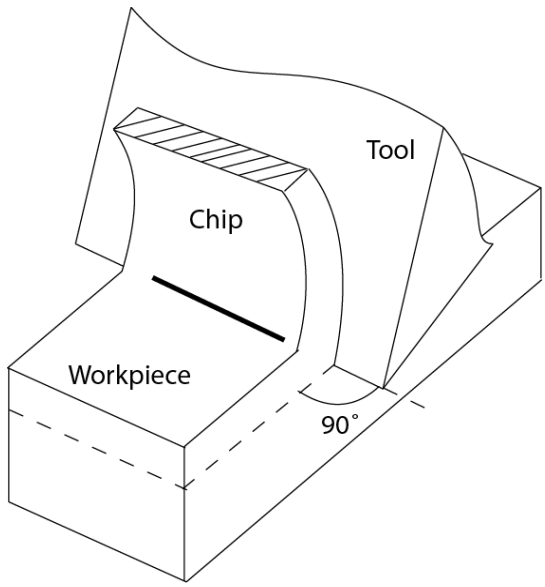

Figure 2-1: Orthogonal Cutting Process [5].

As shown in Figure 2-1, the uncut material approaches to the tool, sheared, and leaves parallel to the rake face of the tool with a new chip thickness. The width of the chip is assumed to be constant throughout the process. When the face of the tool is perpendicular to the plane of cutting (Figure 2-1), it is called orthogonal cutting, otherwise the process is considered to be oblique.

Cutting forces occur in three directions in oblique cutting as shown in Figure 2-2 [11]. The component of the force acting on the rake face of the tool, normal to the cutting edge, is the tangential cutting force. The force component, acting in the radial direction, tending the push the tool away from the workpiece, is called the radial force. The third component is acting on the tool in the horizontal direction, parallel to the direction of feed, is referred as the feed force [12][13][5].

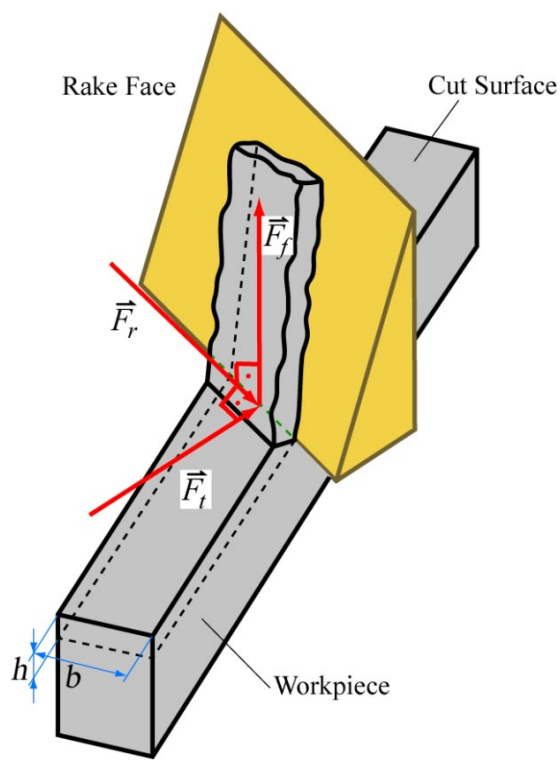

Figure 2-2: Illustration of Cutting Force Components [12][5].

Researchers [14] attempted to improve the models developed by Merchant. They included sophisticated mathematical formulations of frictional behavior on the tool rake face, high strain rate, work hardening of the workpiece material, and high temperature. Endres et al. [15] developed a cutting force model incorporating parameters of tool

geometry. Lee and Shaffer [16] developed a more sophisticated model by introducing plasticity of the workpiece material into the solution.

2.3 Cutting Force Models

Cutting force models using the tool geometry have been developed starting with simple orthogonal geometries and extended to the general turning and to milling processes. Following sections present a background on various cutting force models.

2.3.1 Orthogonal Cutting

Orthogonal cutting provides the simplest geometry to study metal cutting mechanics, and models of the process have been advanced in the form of shear angle solutions. The best known approach is presented by Merchant [7] who defined the rake face contact as elastic with a constant coefficient of friction. The shear angle solution of this model is derived from minimum energy principle as:

$$\phi_{Merchant} = \frac{\pi}{4} + \frac{\gamma_n}{2} - \frac{\beta_a}{2} \tag{2.1}$$

where γ_n and β_a are the normal rake angle and friction angle respectively. Lee and Shaffer [16] proposed the following shear angle relationship using a slip-line field approach:

$$\phi_{Lee} = \frac{\pi}{4} + \gamma_n - \beta_a \tag{2.2}$$

The validity of the shear angle relationships have been evaluated [17], and improved models have been presented [18][19][20]. Assuming there is only sliding friction on the rake face and there is a thin primary shear deformation area, the above models lead to the following expressions for the magnitudes of the tangential force and feed force:

$$\begin{aligned} F_t &= h\,b\left(\tau_s \frac{\cos(\beta_a - \gamma_n)}{\sin\phi_c \cos(\phi_c + \beta_a - \gamma_n)}\right) \\ F_f &= h\,b\left(\tau_s \frac{\sin(\beta_a - \gamma_n)}{\sin\phi_c \cos(\phi_c + \beta_a - \gamma_n)}\right) \end{aligned} \tag{2.3}$$

where h is the uncut chip thickness, b is the width of cut and τ_s is the shear yield stress of the workpiece material. Since it is difficult to predict the shear and the friction angles, a simplified mechanistic model of cutting forces has been developed. The normal approach in practice is to combine the effects of shear angle, rake angle, and friction angle under a parameter called as the specific cutting pressure:

$$\begin{aligned} F_t &= hbK_t \\ F_f &= hbK_f \end{aligned} \tag{2.4}$$

where K_i is the specific cutting pressure of direction i. Another approach to calculate the forces is using an exponential force model in which specific cutting force pressures have been expressed as an exponential function of the chip thickness. Sabberwal and Koenigsberger [21][22] used this approach and obtained specific cutting coefficients experimentally. Their cutting force equation has been stated by:

$$\begin{aligned} F_t &= K_t bh^{m_1} \\ F_r &= K_r bh^{m_2} \end{aligned} \tag{2.5}$$

where K_t, K_r, m_1, and m_2 are experimentally calibrated empirical constants. It is possible to account for the edge forces by linearizing the cutting force expression. Linearization leads to a formulation of total cutting forces that are proportional to the undeformed chip cross sectional area and ploughing forces that are proportional to the length of the active cutting edge:

$$\begin{aligned} F_t &= K_{tc} bh + K_{te} b \\ F_r &= K_{rc} bh + K_{re} b \end{aligned} \tag{2.6}$$

In this thesis, a linear cutting force model with edge coefficients is used. The advantage of linear cutting coefficient model is that it is more compatible with other process models, i.e. stability calculations require constant cutting coefficient in order to solve the differential equations. With the nonlinear coefficient model, the differential equations in stability calculation will be nonlinear.

2.3.2 Forces in Turning

Most turning tools have oblique geometry with a nose radius (r_ε), a cutting edge angle (κ_r), and an inclination (oblique) angle (λ_s). It is possible to extend the orthogonal cutting model by introducing the concept of equivalent chip thickness [23]. The equivalent chip thickness combines the effects of nose radius and cutting edge angle on the cutting forces. At constant velocity, it has been found that the cutting forces can be expressed as a function of equivalent chip thickness [23][24]. In this model, the direction of the in-plane feed force is described by the chip flow angle η, using the following equations (Figure 2-3):

$$F_y = F_f \sin\eta$$
$$F_z = F_f \cos\eta \tag{2.7}$$

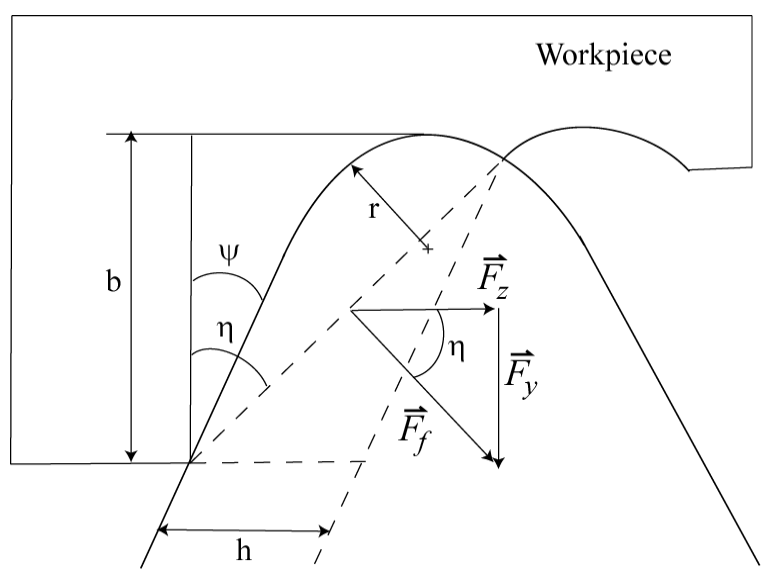

Figure 2-3: Turning Operation Using a Tool with a Nose Radius and Colwell's Approach.

The chip flow angle (η) has been modeled mostly empirically without considering the mechanics of the process. Nevertheless, these models are fairly successful in predicting chip flow angle, provided they are used at certain cutting conditions. Colwell [25] suggested that, without obliquity, the feed force is perpendicular to the line connecting the two end points of the active cutting edge. Okushima and Minato [26] proposed that the average chip flow ($\bar{\eta}$) is the summation of elemental flow angles over the entire length of cutting edge:

$$\bar{\eta} = \frac{\int \eta(s) ds}{\int ds} \tag{2.8}$$

where $\eta(s)$ is the direction of each unit's elemental surface normal and s is the arc length along the cutting edge. For the case of a straight oblique cutting edge, Stabler [27] stated that the chip flow angle is equal to the inclination angle. Young et al. [28] published a combined approach which assumed Stabler's chip flow rule was valid for infinitesimal chip widths and summed the directions of the elemental friction forces in order to obtain the direction of chip flow. Dividing the tool – chip interface into small elements and calculating the force contribution of each element in X and Y directions, they estimated the direction of chip flow as (Figure 2-4):

$$\bar{\eta} = \tan^{-1}\left(\frac{\int \sin \eta(s)\, dA}{\int \cos \eta(s)\, dA}\right) \tag{2.9}$$

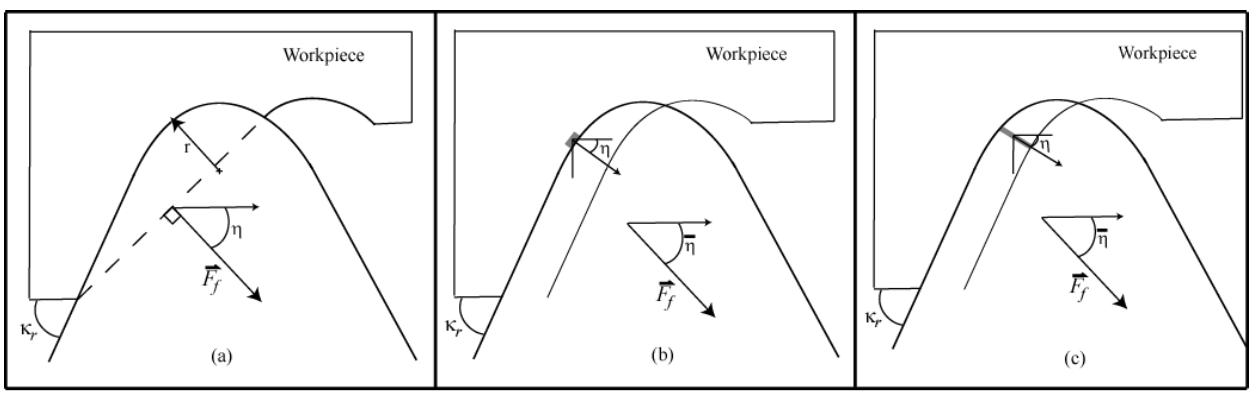

Figure 2-4: Different Approaches for Predicting Chip Flow Direction: (a) Colwell, (b) Okushima and Minato, (c) Young et al.

Wang [29] improved Young et al.'s method [28] by incorporating tool inclination angle and normal rake angle. In Wang's model, cutting region is also divided into many local cutting elements and he assumed that the local chip flow for each element is collinear with that element's friction force, i.e. , Stabler's chip flow rule is applied for each element. The above methods for obtaining the direction of chip flow and feed force are empirical methods and cannot be applicable to all cutting operations. Usui et al. [30][31] have proposed and upper bound model for oblique cutting with a non-straight cutting edge.

The first step in this thesis is to develop a simplified but complete cutting force model for oblique non-straight cutting edges. The model uses the mechanics on the rake face of the tool to account for friction and shear forces. This model is described in Chapter 5.

2.3.3 Forces in Milling

The milling process differs from the turning process, because the generated chips, hence the forces are discontinuous, and periodic. Cutting forces occurred during milling is one of the most important parameters in order to improve the productivity and part quality, because deflection, tool breakage, surface quality, and form errors are mainly influenced by cutting forces.

Determination of chip formation is the first step in mechanistic modeling of cutting forces. Early study of Martelotti [32][33] showed that the path of the tool is trochoidal, rather than circular because of the combined rotation and translation of the tool towards the workpiece. Martelotti also claimed that when the feed per tooth is much smaller than the tool radius, circular tool path assumption is valid and the error is negligible:

$$h(\phi) = c \sin \phi \tag{2.10}$$

where h is the instantaneous chip thickness, c is the feed rate, and ϕ is the immersion angle of a tooth. Milling force models in the literature can be classified into two categories. In mechanistic models, the focus is to derive a relationship between cutting forces and process parameters such as tool geometry, workpiece material, and cutting conditions. Early work by Koeingsberger and Sabberwal [22] used experimentally determined cutting coefficients and related chip load to calculate cutting forces:

$$\begin{aligned} F &= K_s a h \\ K_s &= C h^x \end{aligned} \tag{2.11}$$

where K_s is the cutting pressure, a is the radial depth of cut, h is the instantaneous chip thickness, C and x are empirical constants. This model is considered as the first complete model in this category. However, calibration method used in this study is far from the physics of the process, because an empirical curve fitting technique was used

instead of employing cutting laws. Tlusty and McNeil [34], Kline et al. [35], Sutherland and DeVor [36], and Altintas and Spence [37] have improved and adopted the empirical method in their models. Armarego and Deshpande [38] proposed linear cutting force model by introducing edge force components:

$$\begin{aligned} F_t &= K_{tc}\,ah + K_{te}\,a \\ F_r &= K_{rc}\,ah + K_{re}\,a \\ F_a &= K_{ac}\,ah + K_{ae}\,a \end{aligned} \tag{2.12}$$

In Eq. (2.12), indices e and c represent the edge and cutting force components, respectively. Specific cutting coefficients and specific edge coefficients can be determined by applying linear regression to average cutting forces measured at different feed rates and this method is widely used in literature [39].

Mechanistic approach has limitations on milling with complex tools which have variable geometry along the axis of tool. Therefore, specific cutting coefficients are calculated as functions of shear stress, shear angle and friction angle [40] [41]. This method is called mechanics of milling model. In mechanics of milling model, oblique cutting force model is implemented to calculate the cutting coefficients [42][43]. This model is useful for general application to different cutters and it is applicable to cutters with variable geometry. Although orthogonal cutting database preparation is a time consuming process, it is very effective and accurate in calculating the cutting force coefficients [44].

In this thesis, since the aim is to obtain a generalized cutting force model that is capable of covering different cutting processes and cutter geometries, mechanics of milling approach is used to calculate the cutting coefficients. Adaptation of this approach into the proposed cutting force model is demonstrated in Chapter 5. It is shown that the model can accurately predict the cutting forces for different cutter geometries and processes.

2.4 Inserted Cutters

Inserted (indexable) cutters are widely used in industry. In turning operations, most of the tools use inserts with wide selection of shapes and geometries. In milling, inserted mills with large diameters are widely used for machining operations such as rough and finish machining. Compared to solid type cutters, inserted end mills have the following advantages:

- Higher material removal rate
- More stable machining without chatter
- Large cutter diameter availability
- Better chip extraction performance
- Longer tool life
- Lower setup costs

There have been only few studies available in modeling indexed cutters. Fu et al. [45] presented a model for inserted face milling cutters. They included corner radius, calculated equivalent axial and radial rake angles, and used experimentally identified cutting coefficients in their force model, which is improved in [46]. Various optimization methods with feed rate scheduling and surface error models have been studied by implementing mechanistic models in milling. Kim et al. [47] presented a feed rate scheduling algorithm for indexable end mills. Gu et al. [48] presented a model to predict the surface flatness in face milling. Ko and Altintas [49] developed a model for plunge milling operation using inserted cutters. Choudhury and Mathew [50] adopted non-uniform pitch angles to their face milling model.

Most of the work done on inserted cutters is for certain types of cutters and very few researchers attempted to generalize a cutting model which can be applied to all cutters used in industry. Engin and Altintas [1] presented a cutting force model for indexable end milling. They generalized the envelope of the indexable end mill, and predicted cutting forces to evaluate surface roughness and chatter stability. They considered the insert edge on the cutter envelope to be straight line and used average cutting coefficients varying along the axial disk elements. Also, the uncut chip thickness was calculated from a geometric model. This is the first approach to generalized inserted

cutter geometries. However, this model cannot account for corner radius, chamfer edge, and wiper edge. In addition, insert shapes used in this model are not capable of resembling all insert shapes currently being used in industry.

2.5 Generalized Mechanics of Machining

As described throughout this chapter, there are various successful cutting force models to determine the cutting mechanics for different operations. However, these models are mostly limited by specific machining process, cutter geometry and cutting conditions. There is a lack of a fundamental approach that can combine different models by using the mechanics of metal cutting. Armarego [51][52] proposed a unified cutting modeling approach by combining oblique cutting operations and defining the cutting forces in shear and friction directions. These unique studies to generalize the cutting models are the first and only approach so far, but he concluded his work by defining individual empirical equations for different cutting processes to predict the machining parameters as functions of tool geometry and cutting conditions.

The aim of this thesis is to determine the cutting forces by using fundamentals of metal cutting mechanics. The cutting forces are expressed as friction and normal forces on the rake face, and by using the cutter geometry, forces are transformed to machine coordinates. This model can be applied to different metal cutting processes, such as, turning, milling, boring, and other cutting operations.

3. ISO Cutting Tool Geometry

3.1 Overview

In this chapter, definitions of the cutting tool geometry elements stated in ISO 3002 [53] and ISO 13399 [54] standards are summarized. These standards are published by the Organization for Standardization (ISO) and include the definitions of reference planes, major and minor cutting edge geometries, tool holders, connection elements, etc. Although the illustrations and figures in this chapter are mostly for turning tools and inserted cutters, they are applicable to the geometry of different individual tools, such as single-point tools, drills, and milling cutters.

In the following sections, standard definitions are summarized and outlined in four different parts. In the first part, reference planes which are used to define the cutting angles are defined. The planes used in standards are defined for a selected point on the cutting edge. Since the most tool angles are designated by planes, so that the angles are defined for the same selected point on the cutting edge. In the second part, tool angles and other angular quantities are defined to describe the orientation of the cutting edge. In the third part, dimensional quantities necessary to describe the cutting edge are defined and finally, definitions of insert shapes, which are highly used in this thesis, are presented. For the sake of simplicity, definitions of angular and dimensional quantities related only to major cutting edge are given.

3.2 Planes

Tool Reference Plane (P_r): A plane through the selected point on the cutting edge, so chosen as to be either parallel or perpendicular to a plane or axis of the. It is generally oriented perpendicular to the assumed direction of primary motion.

For an ordinary turning system, it is a plane parallel to the base of the tool. For a milling cutters and drills, it is a plane containing the tool axis.

Assumed Working Plane (P_f): A plane through the selected point on the cutting edge and perpendicular to the tool reference plane P_r and so chosen as to be either parallel or perpendicular to a plane or an axis of the. It is generally oriented parallel to the assumed direction of feed motion.

For ordinary lathe tools it is a plane perpendicular to the tool axis. For drills, facing tools, and parting-off tools, it is plane parallel to the tool axis. For milling cutters, it is a plane perpendicular to the tool axis.

Tool Back Plane (P_p): Tool back plane is a plane through a selected point on the cutting edge and perpendicular both to the tool reference plane P_r and to the assumed working plane P_f.

Tool Cutting Edge Plane (P_s): Tool cutting edge plane is a plane tangential to the cutting edge at the selected point and perpendicular to the tool reference plane P_r.

Cutting Edge Normal Plane (P_n): Cutting edge normal plane is perpendicular to the cutting edge at the selected point on the cutting edge.

Wiper Edge Normal Plane (P_m): Wiper edge normal plane is a plane through the intersection of the reference planes P_p and P_r perpendicular to the wiper edge.

All the planes defined above are illustrated in Figure 3-1.

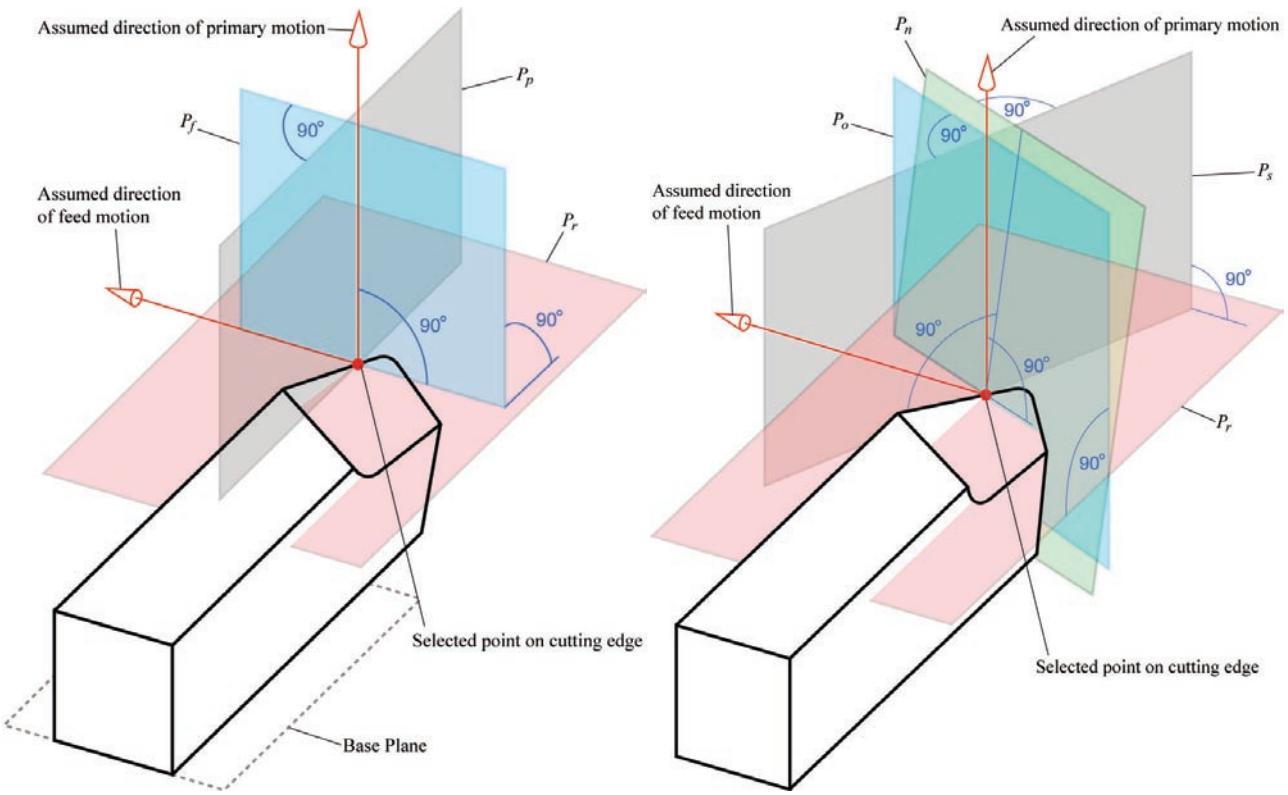

Figure 3-1: Planes Defined in ISO 3002 and ISO 13399.

3.3 Points and Angles

<u>Cutting Reference Point</u> (CRP): Cutting reference point is the theoretical point of the tool from which the major functional dimensions are taken. For the calculation of this point the following cases are applied. Figure 3-2 shows the cutting reference point for different types of cutting edges:

Case 1: Cutting Edge Angle $(\kappa_r) \leq 90°$ - the point is the intersection of: the tool cutting edge plane P_s, the assumed working plane P_f, and the tool rake plane.

Case 2: Cutting Edge Angle $(\kappa_r) \geq 90°$- the point is the intersection of: the assumed working plane P_f, a plane perpendicular to assumed working plane and tangential to the cutting corner, and the tool rake plane.

Case 3: ISO tool styles D and V (55° and 35° rhombic inserts respectively) with only axial rake. The point is the intersection of: a plane perpendicular to the primary feed

direction and tangential to the cutting edge (tangential point), a plane parallel to the feed direction through the tangential point, and the tool rake plane.

Case 4: Round inserts - a) feed direction parallel to the tool axis, primary used for turning tools. The point is the intersection of: a plane perpendicular to the primary feed direction and tangential to the cutting edge, a plane parallel to the feed direction through the tangential point, and the tool rake plane; b) feed direction perpendicular to the tool axis, primarily used for milling tools. The point is the intersection of: a plane perpendicular to the primary feed direction and tangential to the cutting edge, a plane parallel to the feed direction through the tangential point, and the tool rake plane.

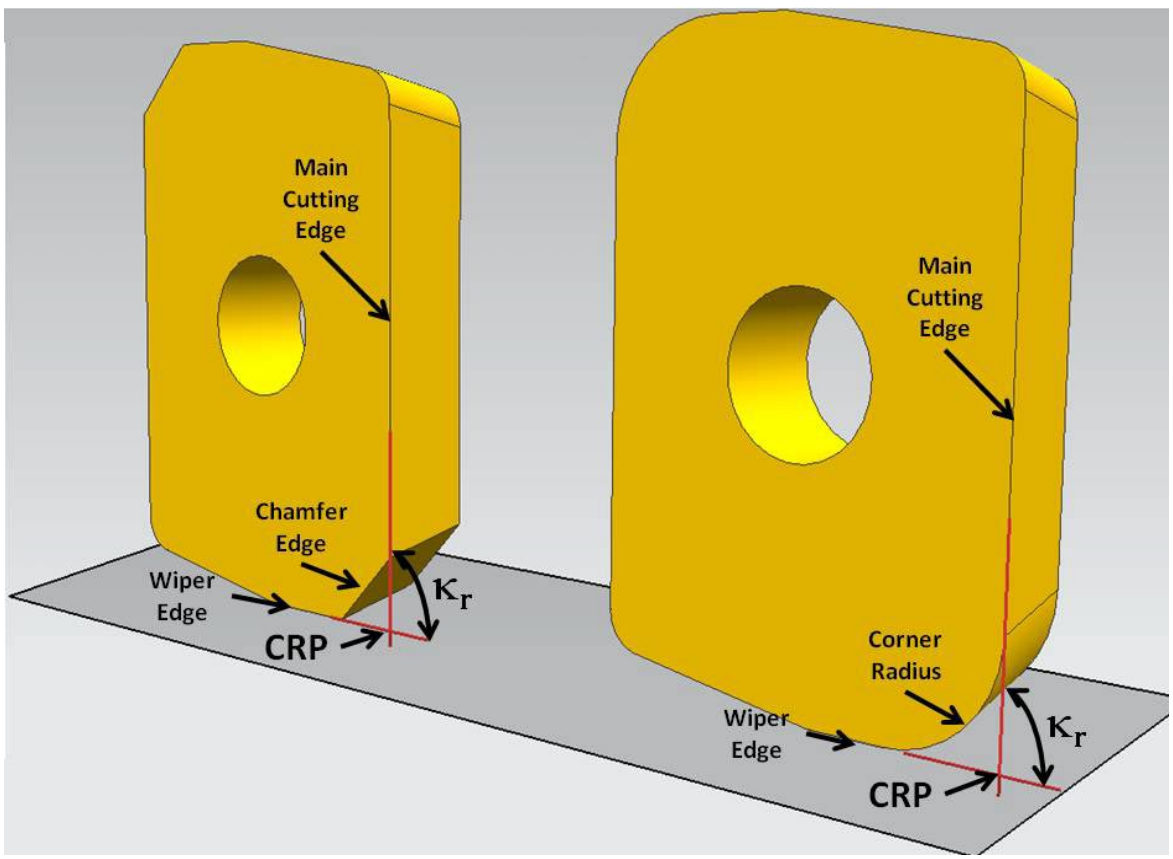

Figure 3-2: Illustration of the Cutting Reference Point (CRP).

Tool Radial Rake Angle (γ_f): Tool rake angle is the angle between rake face and tool reference plane P_r measured in assumed plane P_f. It is also called side rake angle.

Tool Axial Rake Angle (γ_p)**:** Tool axial rake angle is the angle between rake face and tool reference plane P_r measured in the tool back plane P_p. It is also called back rake angle.

Tool Normal Rake Angle (γ_n): Tool normal rake is the angle for major cutting edge between the rake face and the reference plane P_r measured in plane P_n.

Tool Included Angle (ε_r): It is the angle between the tool cutting edge plane P_s, and tool minor cutting edge plane. Simply, it is the angle between the major and minor cutting edges of a cutting item.

Tool Cutting Edge Angle (κ_r): Tool cutting edge angle is the angle between P_s and plane P_f measured in the reference plane P_r. In other words, it is the angle between major cutting edge and the direction of major feed.

Tool Approach Angle (ψ_r): The angle between the tool cutting edge plane P_s and the tool back plane P_p measured in the tool reference plane P_r. Tool approach angle is only defined for the major cutting edge. Thus at any selected point on the major cutting edge, the following equation is valid:

$$\kappa_r + \psi_r = 90° \tag{3.1}$$

Tool Cutting Edge Inclination Angle (λ_s): It is the angle between the cutting edge and the tool reference plane P_r measured in the tool cutting edge plane P_s. Tool cutting edge inclination angle is also referred as oblique angle or helix angle in milling tools.

Corner Chamfer Angle (K_ε): Corner chamfer angle is the angle of a chamfer on a corner measured from the major cutting edge.

Angles defined in this section are shown in Figure 3-3 and Figure 3-4 and the definitions of these angles are summarized in Table 3-I.

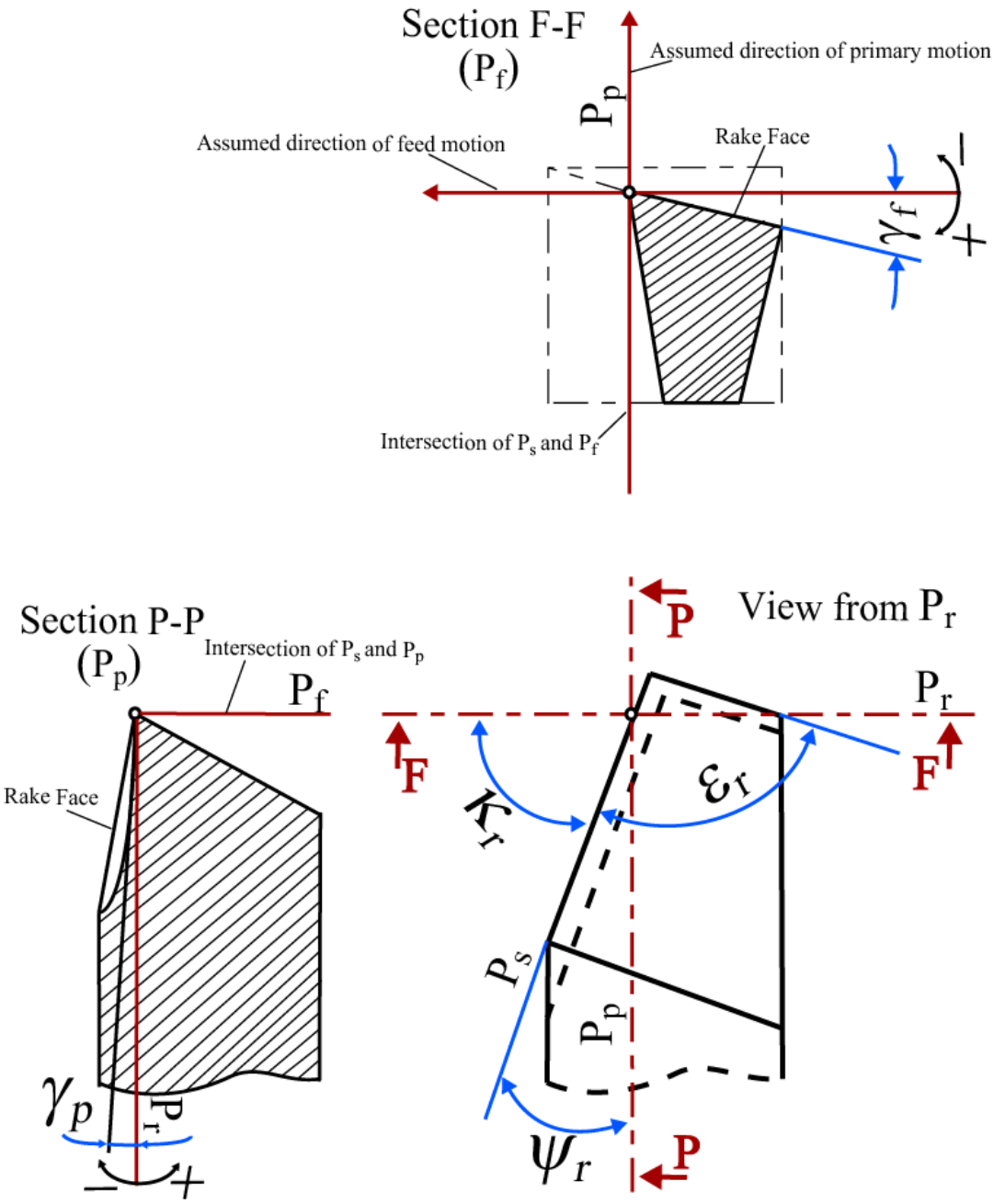

Figure 3-3: Demonstration of Tool Angles in ISO Standards for a Turning Tool.

Table 3-I: Summary of Angles for Definition of Orientation of Cutting Edge and Rake Face.

ANGLE	Definition		
	Angle Between		Measured In Plane
Orientation Of the Cutting Edge			
$\boldsymbol{\kappa_r}$ Tool Cutting Edge Angle	P_s	P_f	P_r
$\boldsymbol{\psi_r}$ Tool Approach Angle	P_s	P_p	P_r
$\boldsymbol{\lambda_s}$ Tool Cutting Edge Inclination	P_s	P_r	P_s
$\boldsymbol{\varepsilon_r}$ Tool Included Angle	P_s	P_s	P_r
Orientation of the Rake Face ($\boldsymbol{A_\gamma}$)			
$\boldsymbol{\gamma_n}$ Tool Normal Rake	A_γ	P_r	P_n
$\boldsymbol{\gamma_f}$ Tool Side Rake	A_γ	P_r	P_f
$\boldsymbol{\gamma_p}$ Tool Back Rake	A_γ	P_r	P_p

3.4 Dimensional Quantities

Dimensional quantities are illustrated in Figure 3-4.

Cutting Diameter (D_c): Cutting diameter is the diameter of a circle created by a cutting reference point (CRP) revolving around the tool axis of a rotating tool item.

Insert Length (L): Insert length is the theoretical length of the cutting edge of a cutting item over sharp corners.

Wiper Edge Length (b_s): Wiper edge length is the measure of the length of a wiper edge of a cutting item.

Insert Width (iW): Insert width is the distance between two sides of an insert when the inscribed circle cannot be used because of the shape of the insert.

Corner Chamfer Length (bch): Corner chamfer length is the nominal length of a chamfered corner measured in the P_r plane.

Corner Radius (r_ε): Corner radius is the nominal radius of a rounded corner measured in the P_r plane.

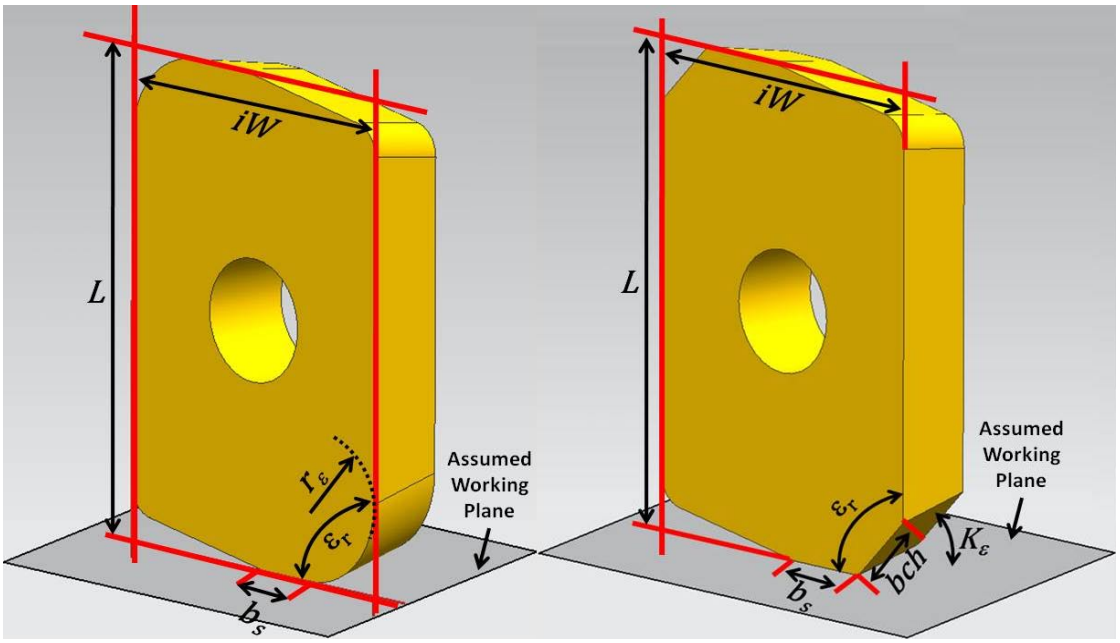

Figure 3-4: Dimensional Quantities Defined in the ISO Standards.

3.5 Insert Shapes

In ISO 13399 standard, insert shapes are categorized in five main different shapes [54]. These categories are equilateral equiangular, equilateral nonequiangular, nonequilateral equiangular, nonequilateral nonequiangular and round inserts. For each main category, there are different shapes of inserts are defined. Table 3-II summarizes the definitions stated below with sample figures.

3.5.1 Equilateral Equiangular Insert

Equilateral equiangular insert is a type of cutting item of regular geometric shape with sides of equal length and equal tool included angles. This category contains inserts with the ISO shape codes: T, S, P, O, and H.

1. **Triangular Insert (T)**: Insert with three equal sides and three equal internal angles with the included angle (ε_r) of 60°.

2. **Square Insert (S):** Insert with four equal sides and four equal internal angles with the tool included angle (ε_r) of 90°.

3. **Pentagonal Insert (P):** Insert with five equal sides and five equal internal angles with the included angle (ε_r) of 108°.

4. **Hexagonal Insert (H)**: Insert with six equal sides and six equal internal angles with the tool included angle (ε_r) of 120°.

5. **Octagonal Insert (O):** Insert with eight equal sides and eight equal internal angles with the tool included angle (ε_r) of 135°.

3.5.2 Equilateral Nonequiangular Insert

It is the type of cutting item of regular geometric shape with sides of equal length and non-equal tool included angles. This category contains inserts with the following ISO shape codes: C, D, E, M, and V for rhombic (diamond) inserts and W for trigon inserts.

1. **Rhombic (Diamond) Insert (C, D, E, M, V)**: Insert with two cutting corners, four sides of equal length and four internal angles none of which are equal to 90°.

2. **Trigon Insert (W)**: Insert with a generally triangular shape with enlarged tool included angles. The edges between the corners may be curved or straight.

3.5.3 Nonequilateral Equiangular Insert

It is the type of cutting item of regular geometric shape with sides of non-equal length and equal tool included angles. This category contains inserts with the ISO shape code L.

Rectangular Insert (L): Insert with four sides and four equal internal angles with the tool included angle (ε_r) of 90°. Opposing sides are in equal length but adjacent sides are not equal in length.

3.5.4 Nonequilateral Nonequiangular Insert

It is the type of cutting item of regular geometric shape with sides of non-equal lengths and non-equal tool included angles. This category contains inserts with the following ISO shape codes: A, B, and K.

1. **Parallelogram Insert (A, B, K)**: Insert with four sides and four internal angles none of which are equal to ninety degrees. Opposing sides are parallel and equal in length.

3.5.5 Round Insert

It is the type of cutting item with circular edges. This category contains inserts with the ISO shape code R.

Table 3-II: Insert Shapes Defined in ISO 13399.

Symbol Shape	Insert	Shape	Nose Angle
S		Square	90
T		Triangular	60
C		Rhombic (Diamond)	80
D			55
E			75
F			50
M			86
V			35
W		Trigon	80
H		Hexagonal	120
O		Octagonal	135
P		Pentagonal	108
L		Rectangular	90
A		Parallelogram	85
B			82
N/K			55
R		Round	-

3.6 Tool Coordinate Frames and Transformations

Coordinate transformations play an important role in this study, hence they are required to define and transform the cutting mechanics from machine coordinate system to the rake face of the cutting tool. Machine coordinate system is defined by axes of the machine tool or the directions of the primary feed motion and primary cutting direction. On the other hand, chip flow coordinate system is defined in two axes; one is on the rake face and aligned in the direction of chip flow, and the second one is normal to the rake face and perpendicular to the chip flow axis. By using these transformations, it is possible to remove the effects of tool geometry from the mechanics of cutting, and eliminate the complexity of different cutting operations such as, turning, milling etc.

Two different coordinate frame definitions and rotations are considered in this thesis. The following procedure is designed to transform the cutting forces or specific cutting force coefficients from machine coordinate system to the rake face. The mechanics of oblique cutting in turning operations is illustrated in Figure 3-5. In order to perform the transformations, chip flow angle (η), which is not defined in ISO standards, is used.

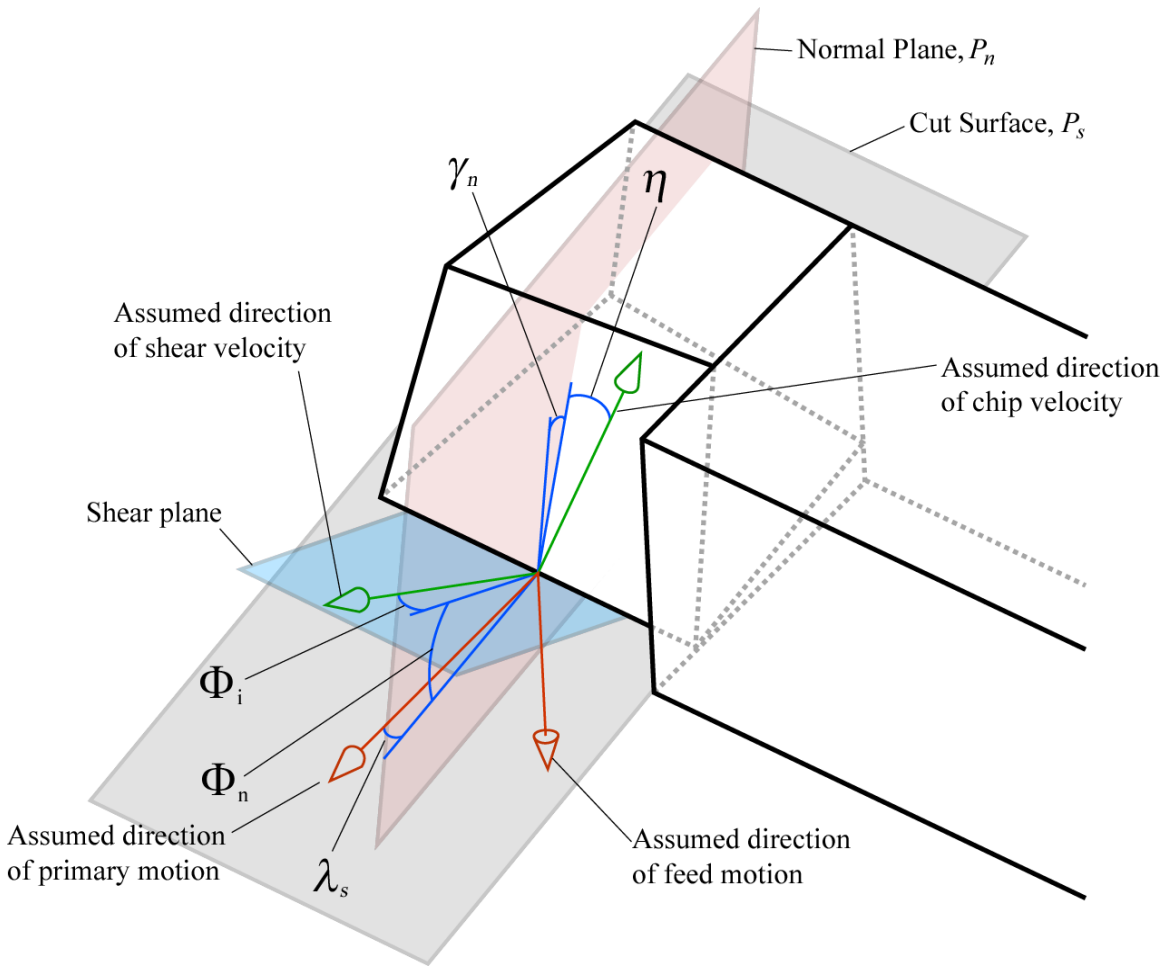

Figure 3-5: Mechanics of Oblique Cutting Process.

3.6.1 Turning Operations

Machine Coordinate System ($X^0Y^0Z^0$)

Machine coordinate system (System 0) is given by the convention of the CNC system. The orientation of the machine coordinate system depends on the specific CNC tool, or the orientation of the dynamometer used to measure the cutting forces. In the most common approach, the Z^0 axis is collinear with the main spindle axis and the X^0 and Y^0 axes are perpendicular to the Z^0 axis. On a lathe, the X^0 axis is the one on which the tool post moves to and away from the workpiece's axis of rotation. The sign convention for this coordinate system is determined such that the movement of the tool in a positive direction leads to a growing measurement of the workpiece. Figure 3-6 shows the machine coordinate system on a turning tool.

Radial – Tangential – Axial Coordinate System (RTA) ($X^I Y^I Z^I$)

RTA coordinate system is defined according to the directions of the cutting forces in orthogonal cutting. The forces in orthogonal turning are in the radial and the tangential directions, whereas the tangential direction is parallel to the direction of primary motion and the radial direction is perpendicular to the primary cutting edge and tool cutting edge plane P_s. Both tangential and radial directions point towards the tool and the coordinate frame's origin is on the cutting edge. The axial direction is perpendicular to both of these directions, pointing away from the tool shaft.

In turning, geometrical transformation from the machine coordinate system ($X^0 Y^0 Z^0$) to RTA coordinate system ($X^I Y^I Z^I$) can be performed by rotating the machine coordinate system around Y^0 axis by amount of cutting edge angle (κ_r) in negative direction. Figure 3-6 illustrates the machine coordinate system and the RTA coordinate system on a turning tool. The transformation to the machine coordinate system can be expressed by a linear rotation matrix C_{01}, so that:

$$a_0 = C_{01}\, a_1 \tag{3.2}$$

where vector a_0 is defined in System 0 and vector a_1 is defined in System 1. Rotation matrix C_{01} can be expressed as follows:

$$C_{01} = \begin{bmatrix} \cos\kappa_r & 0 & -\sin\kappa_r \\ 0 & 1 & 0 \\ \sin\kappa_r & 0 & \cos\kappa_r \end{bmatrix} = \begin{bmatrix} \cos\left(\frac{\pi}{2} - \psi_r\right) & 0 & -\sin\left(\frac{\pi}{2} - \psi_r\right) \\ 0 & 1 & 0 \\ \sin\left(\frac{\pi}{2} - \psi_r\right) & 0 & \cos\left(\frac{\pi}{2} - \psi_r\right) \end{bmatrix} \tag{3.3}$$

$$C_{01} = \begin{bmatrix} \sin\psi_r & 0 & -\cos\psi_r \\ 0 & 1 & 0 \\ \cos\psi_r & 0 & \sin\psi_r \end{bmatrix}$$

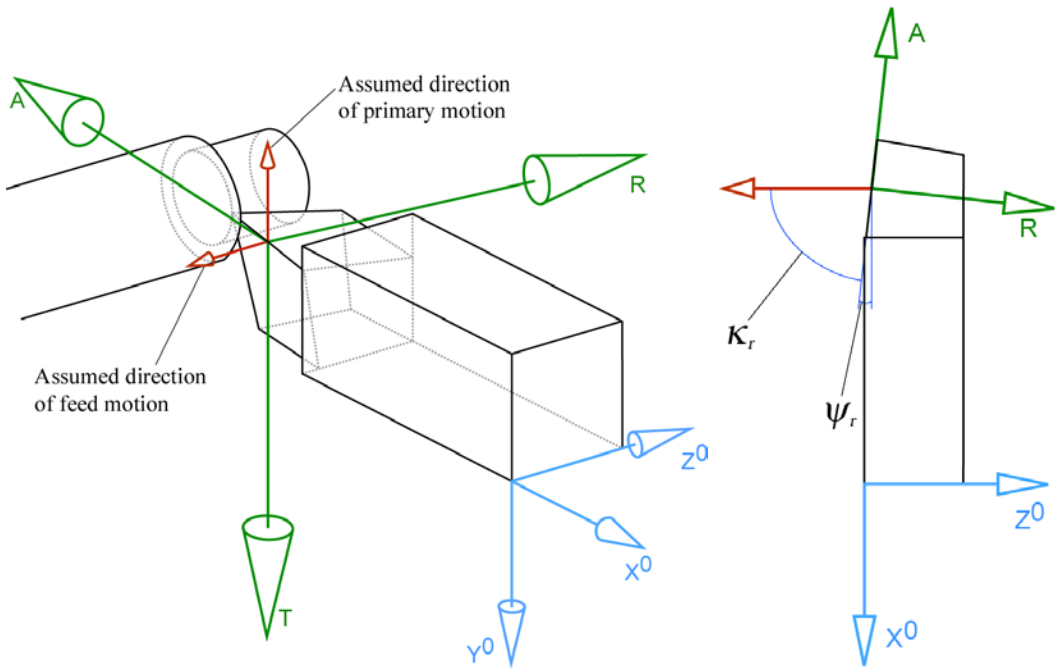

Figure 3-6: RTA and the Machine Coordinate Systems on a Lathe.

Similarly, the inverse transformation from System 0 to System 1 can be determined by calculating the inverse of C_{01}:

$$C_{10} = C_{01}^{-1} = C_{01}^{T}$$

$$C_{10} = \begin{bmatrix} \cos\kappa_r & 0 & \sin\kappa_r \\ 0 & 1 & 0 \\ -\sin\kappa_r & 0 & \cos\kappa_r \end{bmatrix} = \begin{bmatrix} \sin\psi_r & 0 & \cos\psi_r \\ 0 & 1 & 0 \\ -\cos\psi_r & 0 & \sin\psi_r \end{bmatrix} \tag{3.4}$$

Cutting Edge Coordinate System ($X^{II}Y^{II}Z^{II}$)

Figure 3-7 illustrates the cutting edge coordinate system (System 2, (X^{II}, Y^{II}, Z^{II})). The Y^{II} axis of the cutting edge coordinate system lies along the cutting edge of the tool, Z^{II} axis is collinear with R axis, and X^{II} axis is defined perpendicular to Y^{II} and Z^{II} axes. This coordinate frame is also used for the definition of the oblique cutting mechanics in Altintas [5]. In order to transform the RTA coordinate system (System 1) to cutting edge coordinate system (System 2), RTA coordinate system needs to be rotated about R axis by the amount of inclination (helix) angle (λ_s) and additionally, a 90° rotation around the A axis and 90° rotation around the R axis need to be performed, in order to get the axes pointing the proper directions.

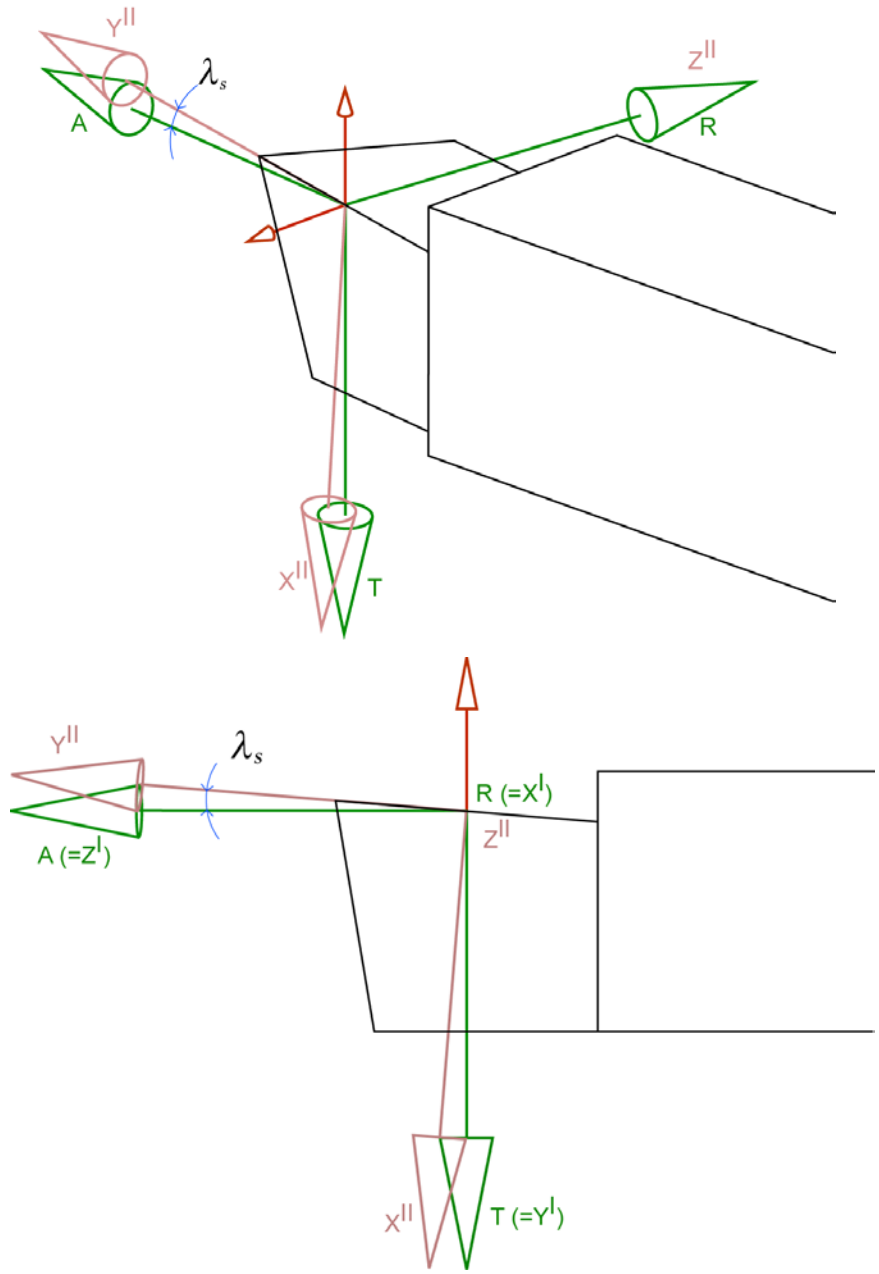

Figure 3-7: Cutting Edge Coordinate System along with the RTA Coordinate System.

Therefore, the transformation matrix is:

$$C_{21} = \left(\begin{bmatrix} 0 & 0 & 1 \\ 1 & 0 & 0 \\ 0 & 1 & 0 \end{bmatrix}\begin{bmatrix} \cos\lambda_s & -\sin\lambda_s & 0 \\ \sin\lambda_s & \cos\lambda_s & 0 \\ 0 & 0 & 1 \end{bmatrix}\right)^{-1} = \begin{bmatrix} 0 & \cos\lambda_s & \sin\lambda_s \\ 0 & -\sin\lambda_s & \cos\lambda_s \\ 1 & 0 & 0 \end{bmatrix} \quad (3.5)$$

And the resultant transformation from machine coordinate system can be accomplished by Eq. (3.6).

$$C_{20} = C_{21}\, C_{10}$$

$$C_{20} = \begin{bmatrix} -\cos\psi_r \sin\lambda_s & \cos\lambda_s & \sin\psi_r \sin\lambda_s \\ -\cos\psi_r \cos\lambda_s & -\sin\lambda_s & \sin\psi_r \cos\lambda_s \\ \sin\psi_r & 0 & \cos\psi_r \end{bmatrix} \tag{3.6}$$

Rake Face Coordinate System ($X^{III}Y^{III}Z^{III}$)

Rake face coordinate system (System 3, ($X^{III}Y^{III}Z^{III}$)) is a transitionary coordinate system used in this study. The Y^{III} axis of the rake face coordinate system is defined on the cutting edge and Z^{III} axis is defined on the rake face of the cutting tool. The transformation from cutting edge coordinate system (System 2) to the rake face coordinate system (System 3) can be accomplished by rotating the cutting edge coordinate system around Y^{II} axis by the amount of normal rake angle (γ_n). Figure 3-8 shows the orientation of the cutting edge coordinate system and rake face coordinate system, and the transformation matrix is shown in Eq. (3.7).

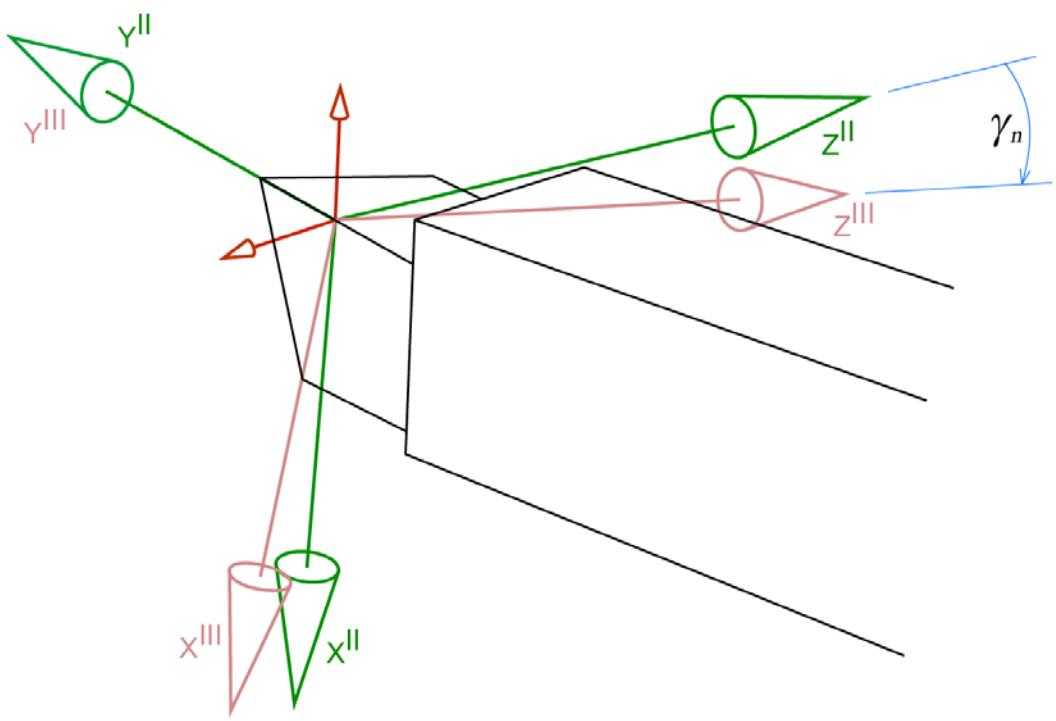

Figure 3-8: Rake Face Coordinate System (System 3): Rotation around the Y^{II} Axis by the Amount of Rake Angle γ_n.

$$C_{32} = \begin{bmatrix} \cos\gamma_n & 0 & -\sin\gamma_n \\ 0 & 1 & 0 \\ \sin\gamma_n & 0 & \cos\gamma_n \end{bmatrix} \tag{3.7}$$

Chip Flow Coordinate System (*UV*)

Chip Flow Coordinate System (System 4, ($X^{IV}Y^{IV}Z^{IV}$)) can be obtained by rotating the rake face coordinate system (System 3) by its X^{III} axis by the amount of chip flow angle (η). With this transformation operation, $U(X^{IV})$ axis of the chip flow coordinate system becomes parallel to the friction force (F_u) and the V (Y^{IV}) axis becomes collinear with the normal force (F_v) acting on the rake face. W or Z^{IV} axis has no physical meaning and will be omitted in this study. Figure 3-9 shows the relationship between the rake face coordinate system and the chip flow coordinate system. The transformation between rake face coordinate system and the chip flow coordinate system can be described by the following equation:

$$\begin{bmatrix} U \\ V \end{bmatrix} = \begin{bmatrix} 0 & -\sin\eta & \cos\eta \\ 1 & 0 & 0 \end{bmatrix} \begin{bmatrix} X^{III} \\ Y^{III} \\ Z^{III} \end{bmatrix} \tag{3.8}$$

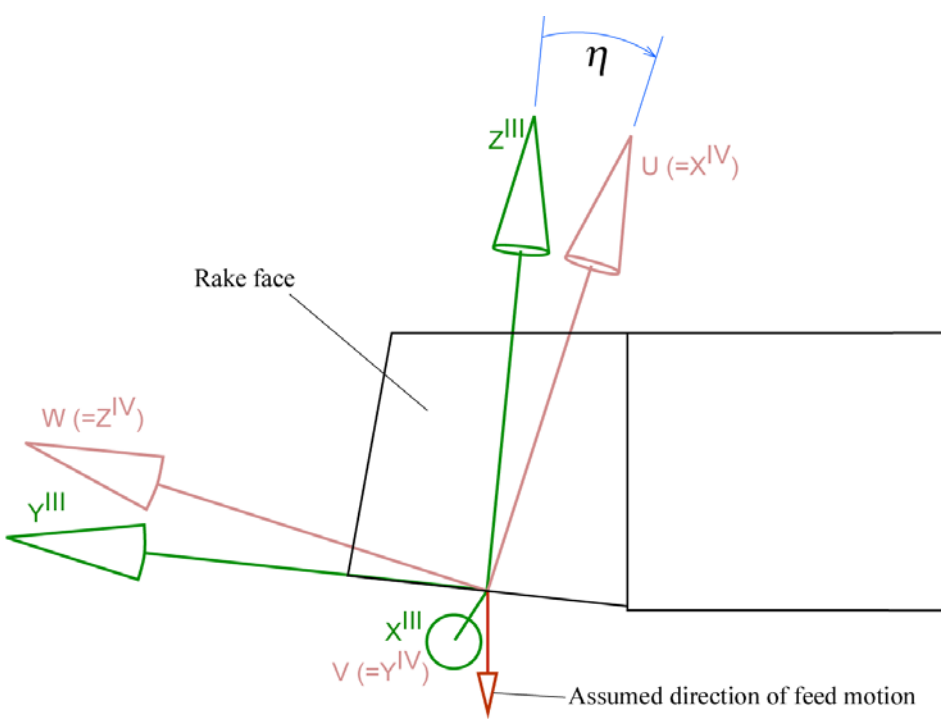

Figure 3-9: Chip Flow Coordinate System (System 4): Rotation around the X^{III} Axis by the Amount of Chip Flow Angle η.

Furthermore:

$$C_{41} = C_{43}\ C_{32}\ C_{21}$$

$$C_{41} = \begin{bmatrix} \cos\gamma_n \cos\eta & -\sin\gamma_n \\ \sin\lambda_s \sin\eta + \cos\lambda_s \sin\gamma_n \cos\eta & \cos\lambda_s \cos\gamma_n \\ -\cos\lambda_s \sin\eta + \sin\lambda_s \sin\gamma_n \cos\eta & \sin\lambda_s \cos\gamma_n \end{bmatrix}^{-1} = C_{41}^T \tag{3.9}$$

Finally, general transformation can be calculated by multiplying the transformation matrices from machine coordinate system to chip flow coordinate system. The resulting transformation is:

$$\begin{bmatrix} U \\ V \end{bmatrix} = A \times \begin{bmatrix} X \\ Y \\ Z \end{bmatrix} \tag{3.10}$$

$$A = \begin{bmatrix} 0 & -\sin\eta & \cos\eta \\ 1 & 0 & 0 \end{bmatrix} \begin{bmatrix} \cos\gamma_n & 0 & -\sin\gamma_n \\ 0 & 1 & 0 \\ \sin\gamma_n & 0 & \cos\gamma_n \end{bmatrix} \begin{bmatrix} 0 & \cos\lambda_s & \sin\lambda_s \\ 0 & -\sin\lambda_s & \cos\lambda_s \\ 1 & 0 & 0 \end{bmatrix} \begin{bmatrix} \sin\psi_r & 0 & -\cos\psi_r \\ 0 & 1 & 0 \\ \cos\psi_r & 0 & \sin\psi_r \end{bmatrix}$$

3.6.2 Transformation of Rotary Tools

As in milling and drilling, instead of workpiece, cutting tool rotates and rotary tools may have more than one cutting edge. Therefore, for each flute, following transformations should be defined individually.

Machine Coordinate System (XYZ)

Similar to a turning machine, the Z axis of the machine coordinate system (System 0, (XYZ)) is parallel to the axis of the spindle. In milling machines, the X axis is the main axis parallel to the working surface, and the Y axis can be found accordingly.

Radial – Tangential – Axial Coordinate System (RTA)

RTA coordinate system (System 1, ($X^I Y^I Z^I$)) is defined similar to a turning tool. Since the cutting edge on a rotary tool is positioned differently relative to the machine coordinate system (System 0), there is a slight difference between transformations in turning and other operations.

In order to perform the transformations from machine coordinate system to RTA coordinate system, an additional coordinate system (System *) is introduced for each flute. System * has its origin located at the selected point on the cutting edge and rotates with the tool. The angle between the machine coordinate system and this coordinate frame is the immersion angle (ϕ). Figure 3-10 illustrates the introduced coordinate system. Immersion angle ϕ is measured clockwise between the positive Y axis and the flutes of the cutting tool. The axes of the System * are aligned so that they are parallel to XYZ for a cutting flute positioned on the X axis, in which the immersion angle is equal to 90° (Flute 2 in Figure 3-10). For instance, when ϕ is equal to 0° (Flute 1 in Figure 3-10) the transformation between System 0 and System * is a rotation around the Z axis by an amount of 90°.

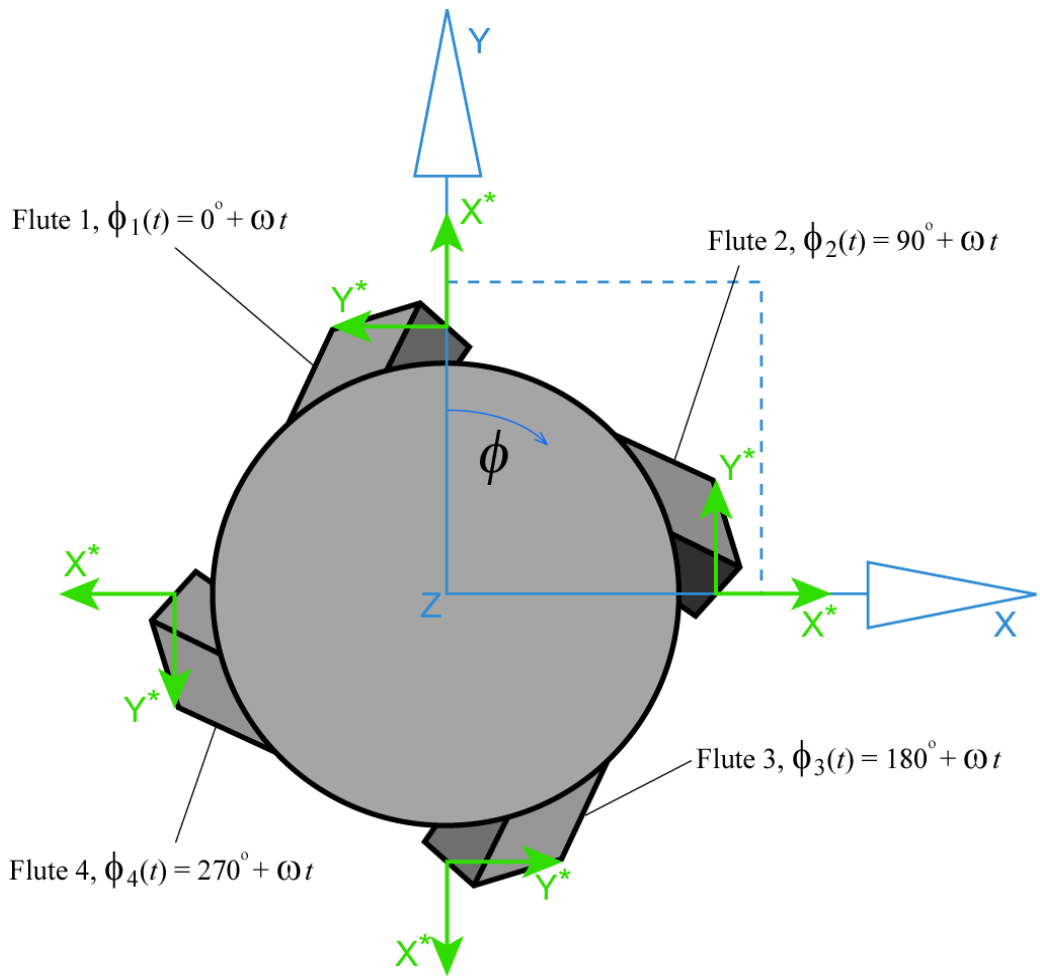

Figure 3-10: Illustration of System * on a Rotary Tool with Four Flutes.

Consequently, the transformation from tool coordinate system (System *) to machine coordinate system (System 0) is a combination of two basic rotations:

$$C_{*0} = \begin{bmatrix} \cos\phi & -\sin\phi & 0 \\ \sin\phi & \cos\phi & 0 \\ 0 & 0 & 1 \end{bmatrix} \begin{bmatrix} \cos 90° & \sin 90° & 0 \\ -\sin 90° & \cos 90° & 0 \\ 0 & 0 & 1 \end{bmatrix}$$
$$C_{*0} = \begin{bmatrix} \sin\phi & \cos\phi & 0 \\ -\cos\phi & \sin\phi & 0 \\ 0 & 0 & 1 \end{bmatrix} \tag{3.11}$$

In RTA coordinate system, T axis is defined parallel to the primary rotational motion of the tool, R axis is aligned towards the axis of the tool while being normal to the cutting edge, and A axis is defined on the cutting edge. The direction of R axis is represented with cutting element position angle $(180° - \psi_r)$. So, the transformation from RTA coordinate system (System 1) to System * is a positive rotation around the Y^* axis by an amount of $\kappa_r + 90°$. Figure 3-11 shows the transformation and the resulting transformation matrix is:

$$C_{1*} = \begin{bmatrix} \cos(\kappa_r + 90°) & 0 & \sin(\kappa_r + 90°) \\ 0 & 1 & 0 \\ -\sin(\kappa_r + 90°) & 0 & \cos(\kappa_r + 90°) \end{bmatrix} = \begin{bmatrix} -\sin\kappa_r & 0 & \cos\kappa_r \\ 0 & 1 & 0 \\ \cos\kappa_r & 0 & -\sin\kappa_r \end{bmatrix}$$
$$C_{1*} = \begin{bmatrix} \cos(180° - \psi_r) & 0 & \sin(180° - \psi_r) \\ 0 & 1 & 0 \\ -\sin(180° - \psi_r) & 0 & \cos(180° - \psi_r) \end{bmatrix} = \begin{bmatrix} -\cos\psi_r & 0 & \sin\psi_r \\ 0 & 1 & 0 \\ \sin\psi_r & 0 & -\cos\psi_r \end{bmatrix} \tag{3.12}$$

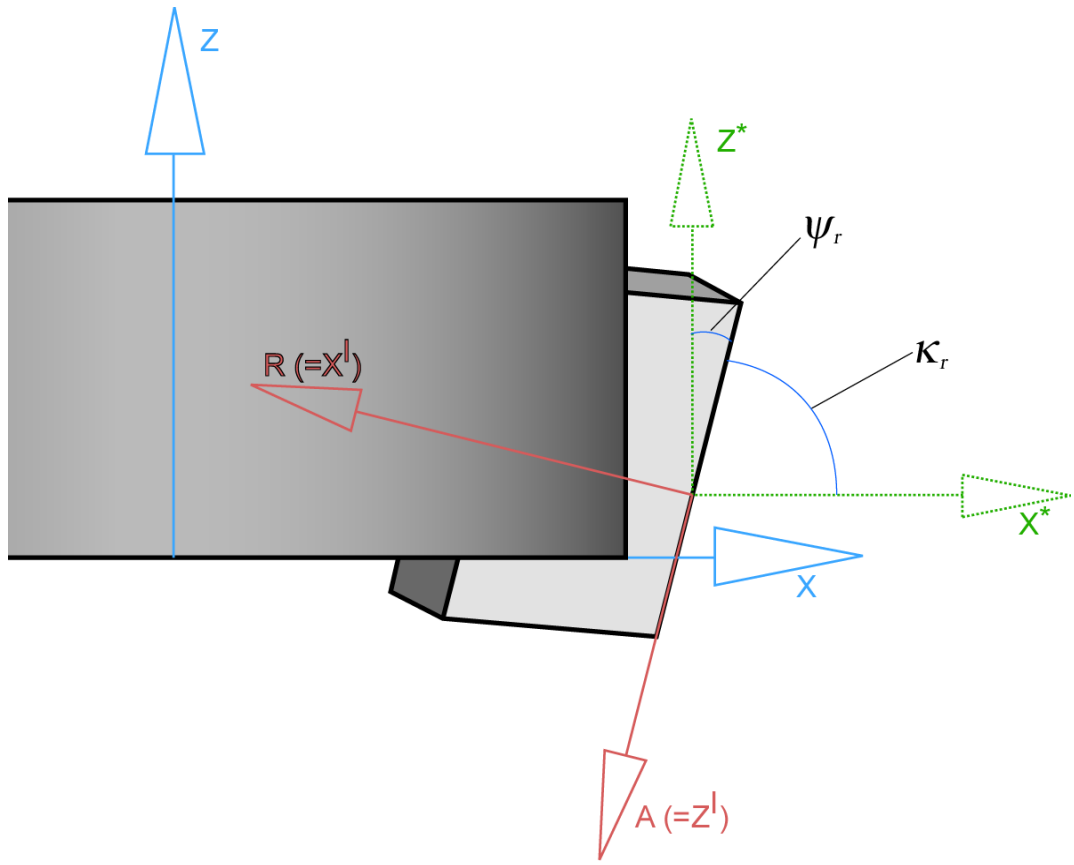

Figure 3-11: Transformation between System 1 and System *.

Thus, the resultant transformation from machine coordinate system to RTA coordinate system can be found as the following:

$$C_{10} = C_{1*}\, C_{*0} = \begin{bmatrix} -\sin\kappa_r & 0 & \cos\kappa_r \\ 0 & 1 & 0 \\ \cos\kappa_r & 0 & -\sin\kappa_r \end{bmatrix} \begin{bmatrix} \sin\phi & \cos\phi & 0 \\ -\cos\phi & \sin\phi & 0 \\ 0 & 0 & 1 \end{bmatrix}$$
$$C_{10} = \begin{bmatrix} -\sin\phi\sin\kappa_r & -\cos\phi\sin\kappa_r & \cos\kappa_r \\ -\cos\phi & \sin\phi & 0 \\ -\sin\phi\cos\kappa_r & -\cos\phi\cos\kappa_r & -\sin\kappa_r \end{bmatrix} \tag{3.13}$$

Cutting Edge Coordinate System ($X^{II}Y^{II}Z^{II}$)

For rotary tools, cutting edge coordinate system (System 2, ($X^{II}Y^{II}Z^{II}$)) is defined the same as turning operations. The transformation from cutting edge coordinate system (System 2) and the RTA coordinate system (System 1) is stated in Eq. (3.14). The coordinate system is demonstrated in Figure 3-12.

$$C_{21} = \begin{bmatrix} 0 & \cos\lambda_s & \sin\lambda_s \\ 0 & -\sin\lambda_s & \cos\lambda_s \\ 1 & 0 & 0 \end{bmatrix} \tag{3.14}$$

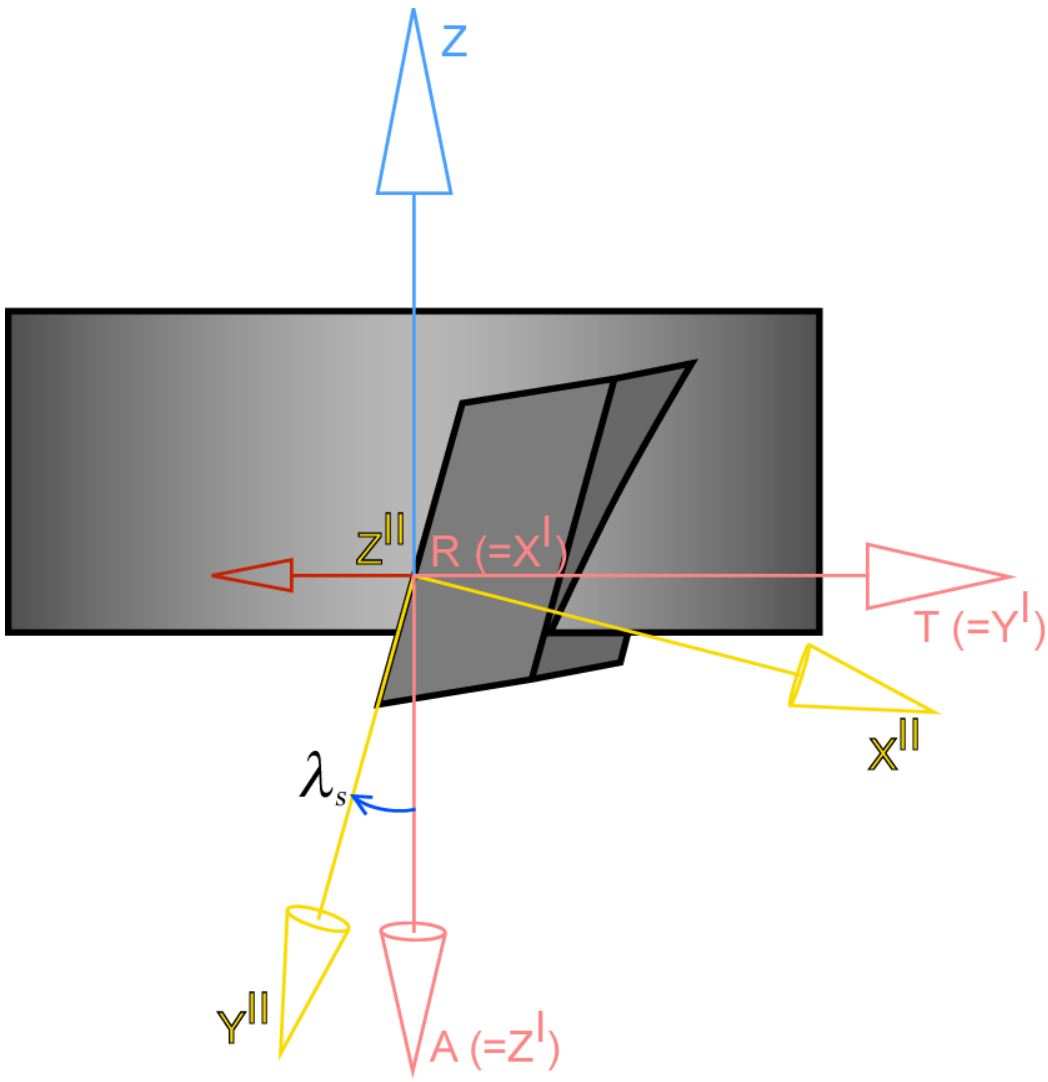

Figure 3-12: Transformation between System 1 and System 2 for Rotary Tools.

Rake Face Coordinate System ($X^{III}Y^{III}Z^{III}$)

As it can be seen from Figure 3-13, rake face coordinate system (System 3) is defined same as the turning operations, which is described in Section 0. As a result,

$$C_{32} = \begin{bmatrix} \cos\gamma_n & 0 & -\sin\gamma_n \\ 0 & 1 & 0 \\ \sin\gamma_n & 0 & \cos\gamma_n \end{bmatrix} \tag{3.15}$$

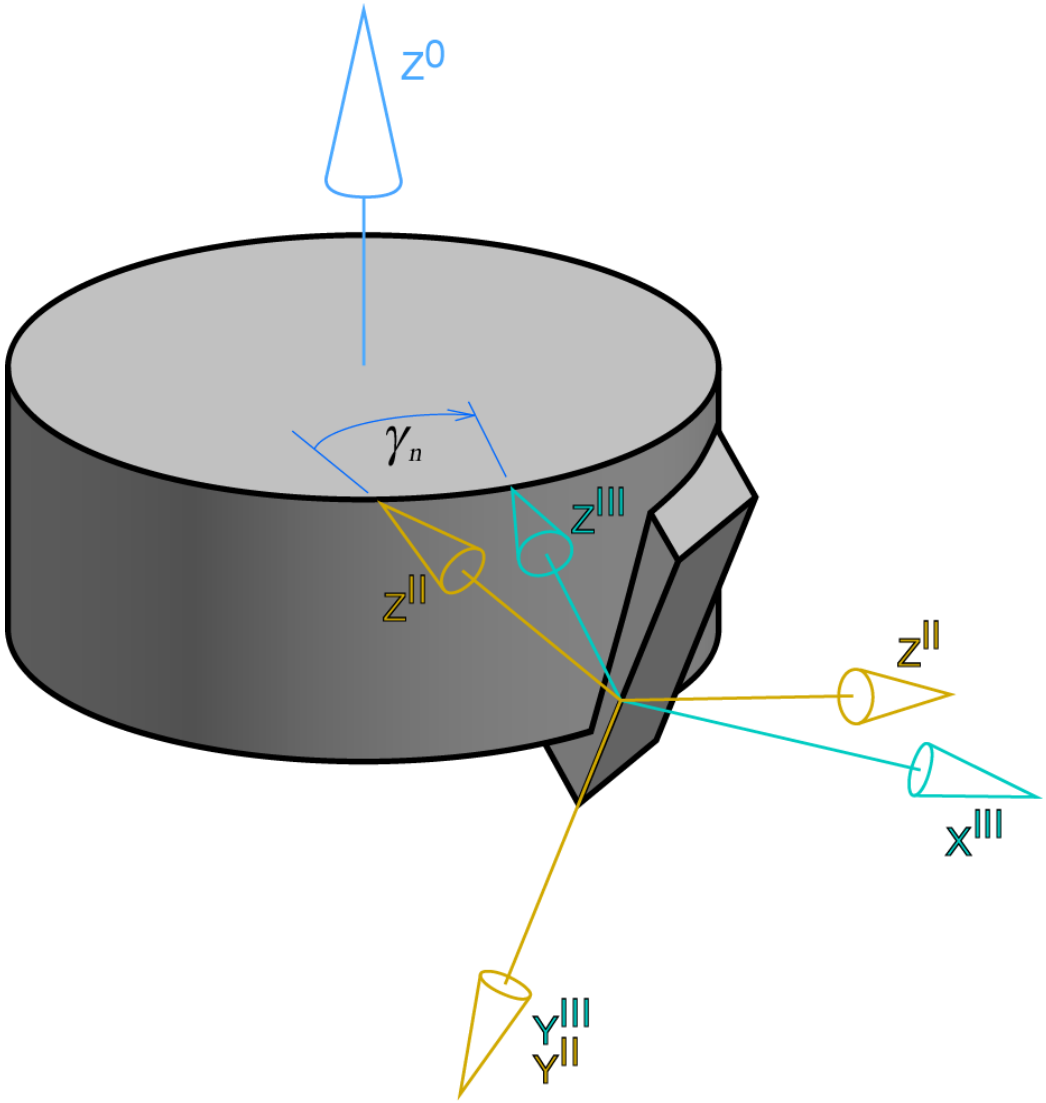

Figure 3-13: Transformation between Rake Face Coordinate System (System 3) and Cutting Edge Coordinate System (System 2).

Chip Flow Coordinate System (*UV*)

Chip flow coordinate system (System 4, ($X^{IV}Y^{IV}Z^{IV}$)) for rotary tools is defined same as turning. It has only two axes: U axis is on the rake face, aligned with the direction of chip flow, and V axis is normal to the rake face. Figure 3-14 shows the representation of chip flow coordinate system on a rotary tool. In this figure, W axis has no physical meaning and is shown only to complete the coordinate system.

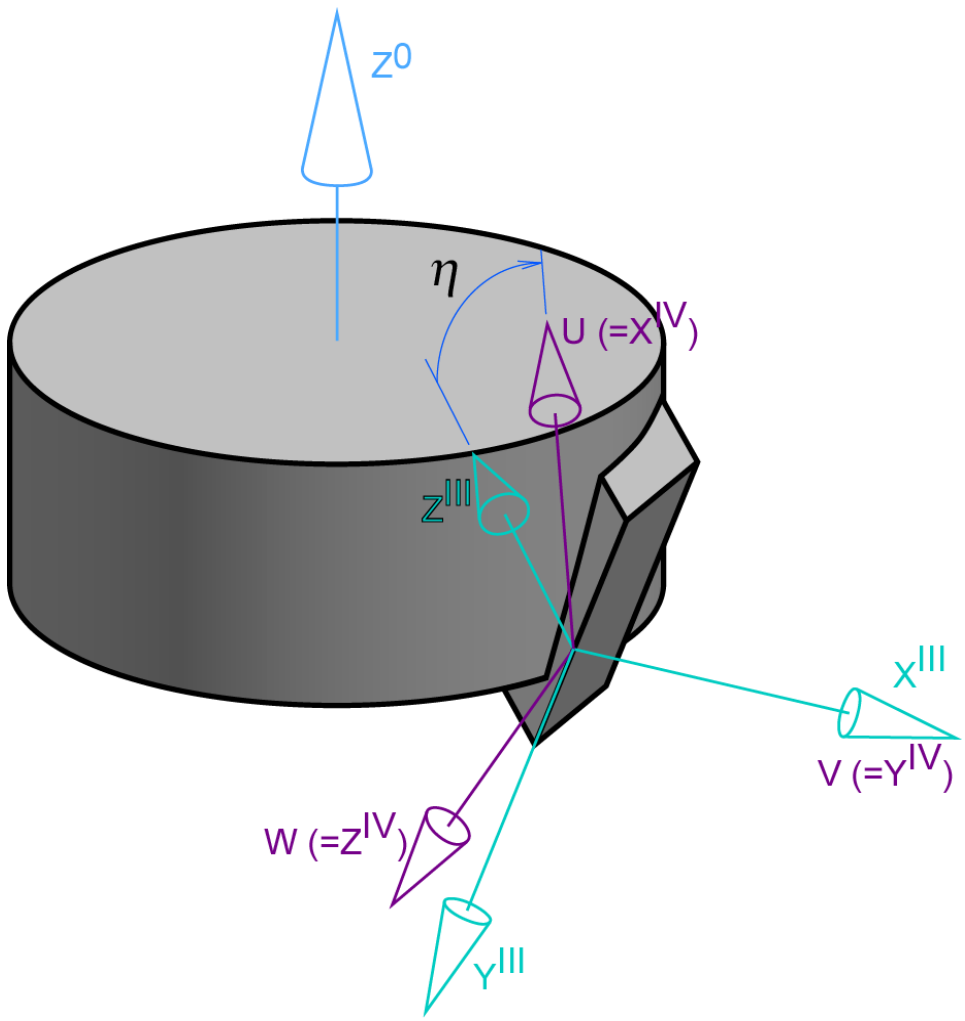

Figure 3-14: Representation of the Chip Flow Coordinate System on a Milling Tool.

The transformation between rake face coordinate system (System 3) and chip flow coordinate system (System 4) is defined by the following matrix:

$$C_{43} = \begin{bmatrix} 0 & -\sin\eta & \cos\eta \\ 1 & 0 & 0 \end{bmatrix} \tag{3.16}$$

3.7 Summary

If the transformation operations in turning and rotating tools are compared, it can be observed that the transformation matrices from RTA coordinate system (System 1) to UV coordinate system (System 4) are identical. The only difference between these operations comes from the rotation of multiple flutes in rotary tools. This difference is explained in Section 0.

By performing these transformations, it is possible to describe the kinematics of the cutting process and cutting forces on the rake face of a cutter regardless of the operation. Thus, cutting forces measurable in machine coordinate system can be described as the friction and normal forces which are in the chip flow coordinate system.

4. Generalized Geometric Model of Inserted Cutters

4.1 Overview

In this chapter, a generalized model for inserted cutters is presented. Inserted cutters are widely used in turning and milling processes, both in roughing and finishing operations because of their low cost advantage on solid cutters. When tool wear or breakage occurs, instead of replacing the cutter body, replacing the insert is sufficient. Due to their popularity and availability in different types of applications, many different inserts are available in terms of shapes and dimensions. As described in Section 3.5, 17 different insert shapes are defined in ISO 13399 standard. Details of these shapes can be seen in Table 3-II of Chapter 3. Since this thesis aims to develop a generalized model, it covers not only insert shapes defined in ISO 13399, but also any arbitrary insert geometry defined by control points.

Modeling of inserted cutters is more complicated than solid body cutters, because number of parameters used to define the insert geometry as well as to place on the cutter body is significantly higher. The output of this model is the axial locations, radii, helix / inclination angles, normal rake angles, and cutting edge angles of the cutting edge(s) at each specified point along the cutter axis. By using this data, it is possible to determine the cutting forces, tool vibrations, static deflections, and stability lobes for almost any kind of machining operations, such as, turning, boring, milling, etc.

In the model, first of all, geometry of the insert is defined insert's local coordinate system analytically and it is placed on the cutter body using the orientation angles, i.e. cutting edge angle κ_r, axial rake angle γ_p, and radial rake angle γ_f. By using these angles, cutting edge positions are transformed to global coordinate system which is located at the cutter tip.

After the transformation, for cutting mechanics which is described in Chapter 5.2, normal rake angle γ_n and helix angle λ_s are calculated using the position of the cutting edge(s). Sample examples are presented at the end of this chapter.

Inputs required to define the cutting edge on an insert are defined in Chapter 3 with illustrative figures, along with the coordinate axes used in this model.

4.2 Mathematical Modeling of an Insert

In mathematical modeling, a similar approach to Engin and Altintas' study [1] has been used with certain modifications and improvements. Firstly, using the inputs, mathematical model of one insert was developed on the local coordinate system ($X^0Y^0Z^0$) positioned at the cutting reference point (CRP) of the insert. Figure 4-1 illustrates the local coordinate system and the cutting reference point on two different inserts. The aim of this model is to calculate the control points that are sufficient to define the features (nose radius, corner chamfer, wiper edge etc.) on an insert.

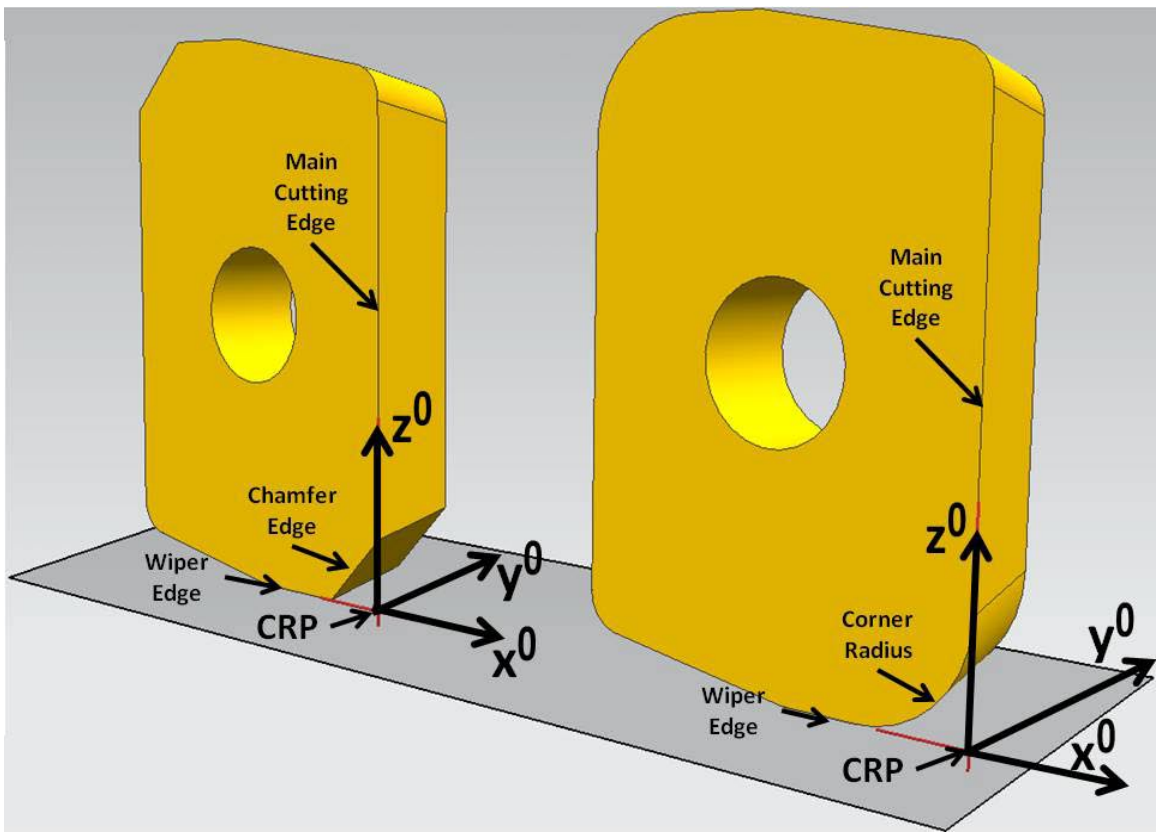

Figure 4-1: Local Coordinate Systems and Cutting Reference Points on Different Inserts.

In ISO 13399 standard, there are various shapes defined for inserts. Therefore, for this study, for each insert shape, control points were formulated for both corner chamfer and nose radius cases. Control points include the positions of the start and the end points of a feature on the cutting edge. For ISO type inserts, these control points are all in x^0z^0 plane, therefore they were all assumed to be flat inserts. For instance, Figure 4-2 shows the control points and dimensions of a parallelogram insert with a wiper edge and a corner radius. In this Figure, points $A, B, D,$ and E are the control points on the cutting edge, C and I used to locate the insert center and the center of corner radius, CRP is the cutting reference point which is the origin for specific dimensions and rotations, point F is the theoretical sharp point of the insert.

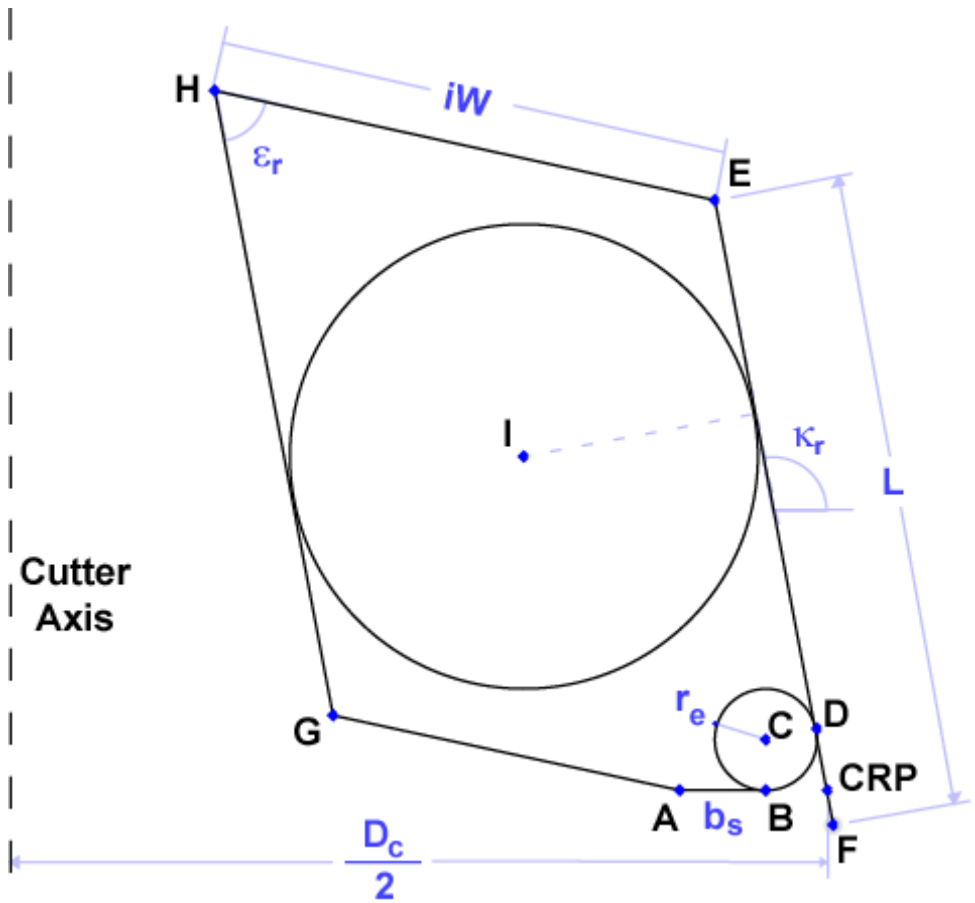

Figure 4-2: Control Points on a Parallelogram Insert.

Cutting reference point was selected as the origin of the local coordinate system. Locations of each control point as well as insert and radius centers were calculated analytically. These control points are rotated according to the given axial and radial rake angles, and transformed to the global coordinate system which is located at the tip of the cutter body. Finally, for modeling of mechanics, normal rake angle, helix angle, and true cutting edge angle were calculated for each point on the cutting edge.

In the following sections, transformations and calculations of angles are described and the whole procedure is applied as examples for two milling inserts with different corner modifications and a turning insert.

4.3 Tool Coordinate Frames and Transformations

Since the cutting reference point (CRP) is used to define all the angular and dimensional values to define an insert, all of the coordinate axes' origins used in this model to orient and place the insert on the cutter body are located at the CRP. Four different coordinate systems were defined to accomplish the required rotations for the orientation of an insert on the cutter body.

Initial coordinate frame F^0 is located with its origin at CRP and the X axis (X^0) along the primary feed direction as seen in Figure 4-3. Z axis (Z^0) of the F^0 frame is parallel to the cutter body rotation axis and positive Z^0 is pointing towards the cutter body. In F^0 frame, X^0Z^0 plane corresponds to tool reference plane P_r, and X^0Y^0 plane corresponds to assumed working plane P_f.

Final coordinate frame F^3 has its X axis (X^3) directed along the cutting edge and the Z axis (Z^3) on the rake face of the insert. In order to transform the F^0 frame to F^3 frame, two intermediate coordinate frames were defined.

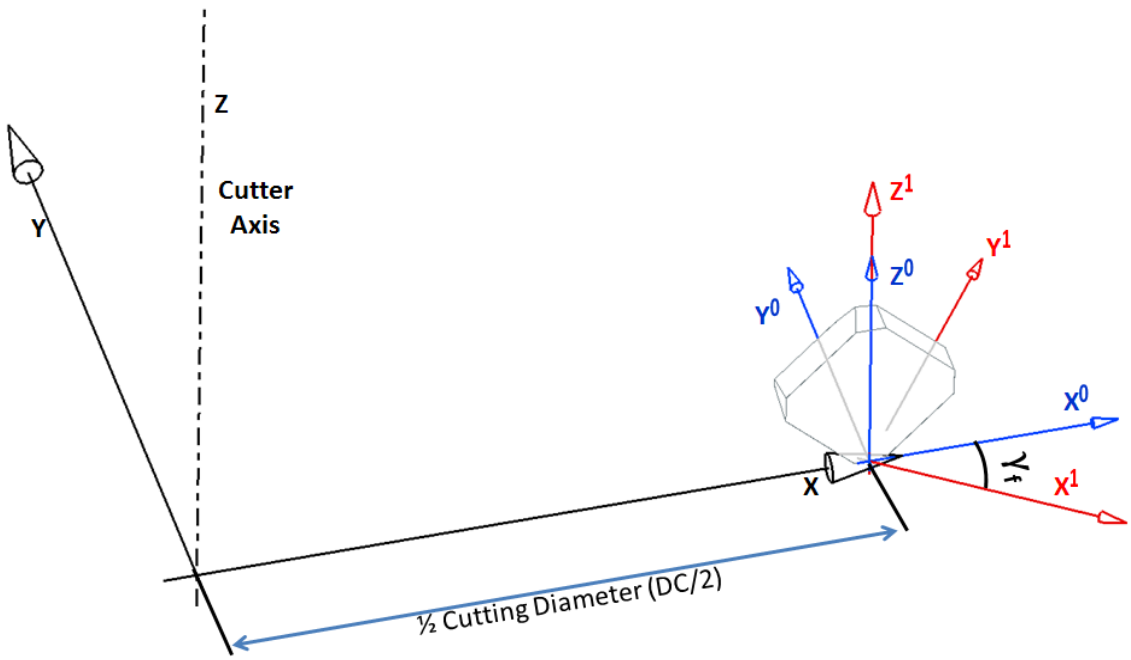

Figure 4-3: Frame F^0 to Frame F^1 Rotation.

4.3.1 Frame F^0 to Frame F^1 Rotation

The first step is to align the X^1 axis with the wiper edge or parallel land in a coordinate frame F^1 by rotating the frame F^0 around Z^0 axis by an amount of radial rake angle in the reverse direction $(-\gamma_f)$. As a result, the rotation matrix R_{01} from frame F^0 to frame F^1 becomes:

$$\theta_z^{01} = -\gamma_f$$

$$R_{01} = \begin{bmatrix} \cos(-\gamma_f) & -\sin(-\gamma_f) & 0 \\ \sin(-\gamma_f) & \cos(-\gamma_f) & 0 \\ 0 & 0 & 1 \end{bmatrix} \tag{4.1}$$

4.3.2 Frame F^1 to Frame F^2 Rotation

The second step is to align the Z^2 axis of the frame F^2 with the rake face of the insert by rotating the frame F^1 around X^1 axis by an amount of axial rake angle also in reverse direction $(-\gamma_p)$. Consequently, the rotation matrix R_{12} which defines the rotation from frame F^1 to frame F^2 becomes:

$$\theta_x^{12} = -\gamma_p$$

$$R_{12} = \begin{bmatrix} 1 & 0 & 0 \\ 0 & \cos(-\gamma_p) & -\sin(-\gamma_p) \\ 0 & \sin(-\gamma_p) & \cos(-\gamma_p) \end{bmatrix} \tag{4.2}$$

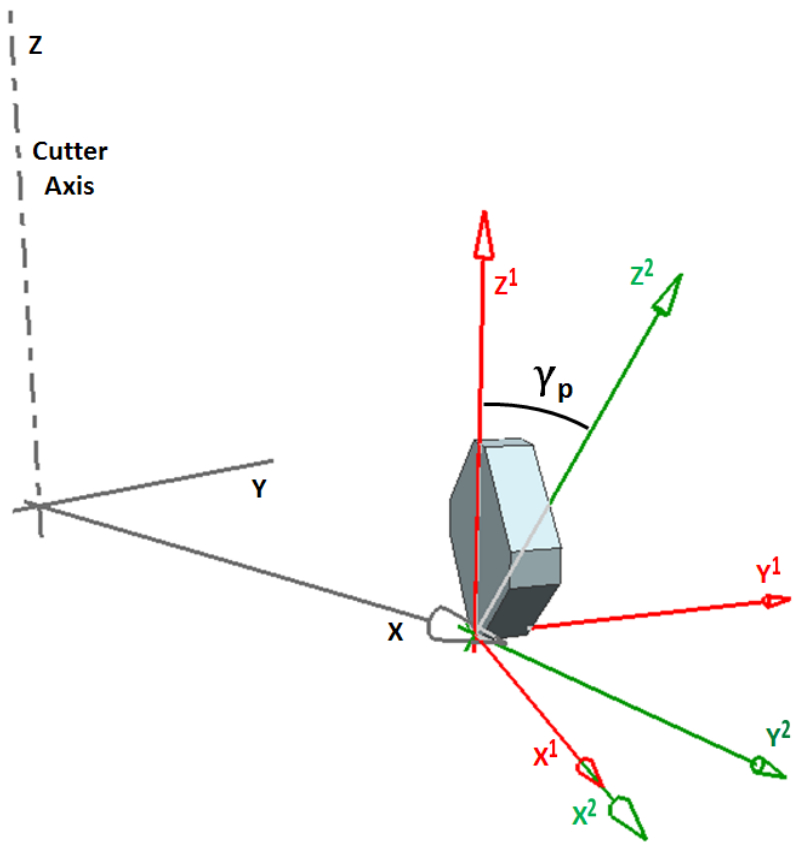

Figure 4-4: Frame F^1 to Frame F^2 Rotation.

4.3.3 Frame F^2 to Frame F^3 Rotation

The final step is to align the X^3 axis of the frame F^3 with the cutting edge of the insert by rotating the frame F^2 around the Y^2 axis by an amount of cutting edge angle in the reverse direction $(-\kappa_r)$. So that the rotation matrix R_{23} defining the rotation from frame F^2 to frame F^3 is:

$$\theta_y^{23} = -\kappa_r$$

$$R_{23} = \begin{bmatrix} \cos(-\kappa_r) & 0 & \sin(-\kappa_r) \\ 0 & 1 & 0 \\ -\sin(-\kappa_r) & 0 & \cos(-\kappa_r) \end{bmatrix} \tag{4.3}$$

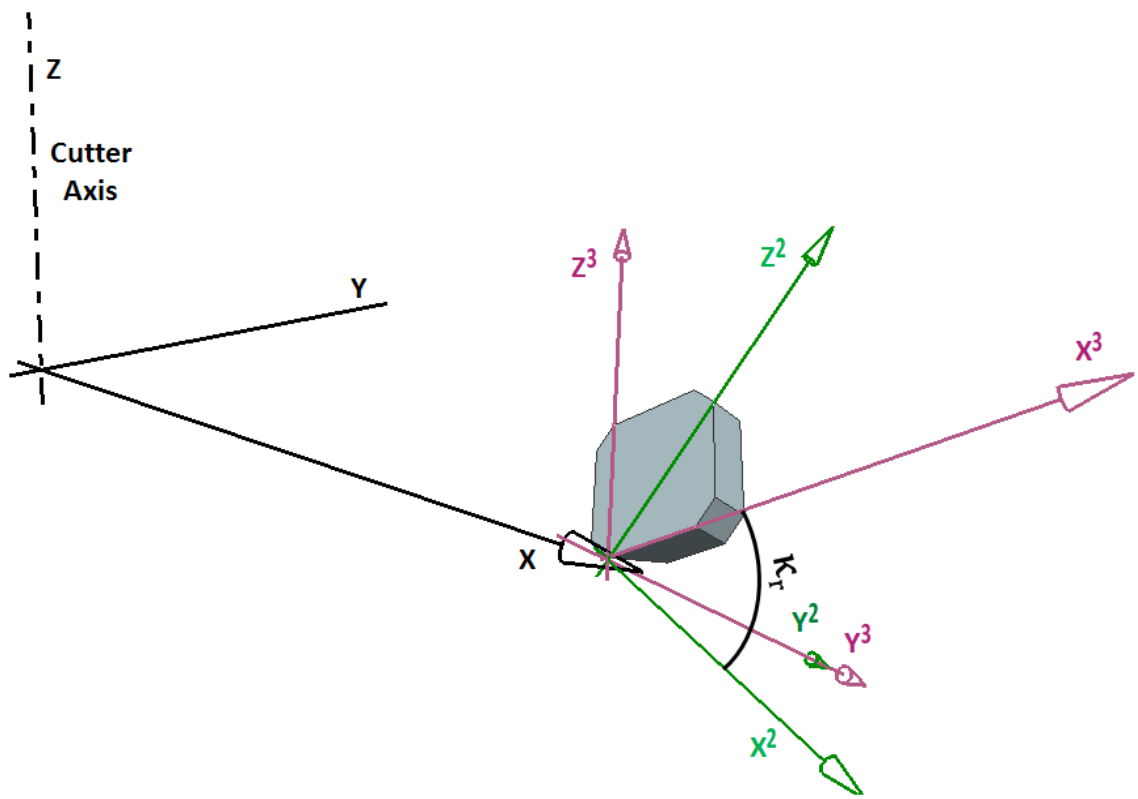

Figure 4-5: Frame F^2 to Frame F^3 Rotation.

Finally, in order to complete the rotation matrix between frames F^0 and F^3 can be calculated as the following:

$$R_{03} = R_{01}\, R_{12}\, R_{23} \tag{4.4}$$

where;

$$R_{03} = \begin{bmatrix} \cos\gamma_f \cos\kappa_r + \sin\gamma_f \sin\gamma_p \sin\kappa_r & \sin\gamma_f \cos\gamma_p & -\cos\gamma_f \sin\kappa_r + \sin\gamma_f \sin\gamma_p \cos\kappa_r \\ \sin\gamma_f \cos\kappa_r + \cos\gamma_f \sin\gamma_p \sin\kappa_r & \cos\gamma_f \cos\gamma_p & \sin\gamma_f \sin\kappa_r + \cos\gamma_f \sin\gamma_p \cos\kappa_r \\ \cos\gamma_p \sin\kappa_r & -\sin\gamma_p & \cos\gamma_p \cos\kappa_r \end{bmatrix} \tag{4.5}$$

4.4 Mathematical Relationships between Angles

Next task in mathematical modeling of insert geometry is to derive the angles used in mechanics of metal cutting which are normal rake angle γ_n, helix / inclination gle λ_s, and cutting edge angle κ_r. These angles were derived according to the definitions summarized in Chapter 3.

4.4.1 Normal Rake Angle

The normal rake angle γ_n can be described as the angle between the direction of primary motion vector ($-Y^0$) and the normal of the rake face (Y^3) measured in the cutting edge normal plane P_n (Y^3Z^3 plane). In order to determine the normal rake angle using the tool design angles (γ_f and γ_p), a vector (v_0) directed along the direction of primary motion was defined in frame F^0. Vector v_0 later can be described in frame F^3 with the inverse of the rotation matrix R_{03}. Therefore:

$$v_0 = \begin{bmatrix} 0 \\ -1 \\ 0 \end{bmatrix} \Rightarrow v_3 = R_{03}^{-1}\, v_0 = R_{03}^{T}\, v_0$$

$$v_3 = \begin{bmatrix} \cos\gamma_f \cos\kappa_r - \cos\gamma_f \sin\gamma_p \sin\kappa_r \\ -\cos\gamma_f \cos\gamma_p \\ -\sin\gamma_f \sin\kappa_r - \cos\gamma_f \sin\gamma_p \cos\kappa_r \end{bmatrix} = \begin{bmatrix} v_{3x} \\ v_{3y} \\ v_{3z} \end{bmatrix} \tag{4.6}$$

In order to measure the normal rake angle γ_n in P_n plane, x component of the v_3 vector (v_{3_x}) was set to zero. From Figure 4-6, it can be observed that:

$$\gamma_n = \text{atan}(\frac{-v_{3z}}{-v_{3y}}) = \text{atan}(\frac{v_{3z}}{v_{3y}})$$
$$\gamma_n = \text{atan}(\frac{\sin\gamma_f \sin\kappa_r + \cos\gamma_f \sin\gamma_p \cos\kappa_r}{\cos\gamma_f \cos\gamma_p}) \tag{4.7}$$

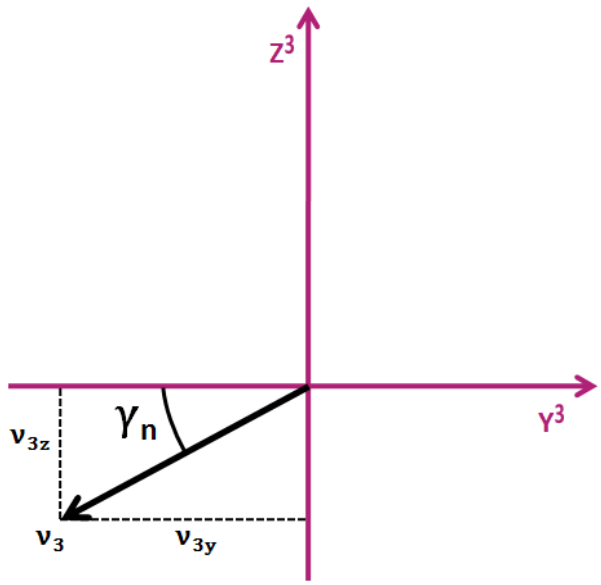

Figure 4-6: Derivation of Normal Rake Angle.

4.4.2 True Cutting Edge Angle

True cutting edge κ_r^* is defined as the angle between the cutting edge (X^3) and the assumed working plane P_f (X^0Y^0 plane) measured in the tool reference plane P_r (X^0Z^0 plane). The mathematical relationship between the true cutting edge angle κ_r^* and the tool design angles (γ_f, γ_p and κ_r) can be calculated by defining a vector, $v_{edg\,e_3}$, along the cutting edge in frame F^3 and using the rotation matrix R_{03} to describe the vector in F^0 coordinate frame. In order to measure the angle in tool reference plane P_r, $v_{edg\,e_{0y}}$ component of the vector $v_{edg\,e_3}$ was set to zero. As a result, true cutting edge angle κ_r^* can be determined as the angle between the cutting edge vector $v_{edg\,e_0}$ and the X^0 axis.

$$v_{edge\,3} = \begin{bmatrix}1\\0\\0\end{bmatrix}, v_{edge\,0} = R_{03}\ v_{edge\,3} = \begin{bmatrix}v_{edge\,0x}\\v_{edge\,0y}\\v_{edge\,0z}\end{bmatrix}$$
$$v_{edge\,0} = \begin{bmatrix}\cos\gamma_f\cos\kappa_r + \sin\gamma_f\sin\gamma_p\sin\kappa_r\\ -\sin\gamma_f\cos\kappa_r + \cos\gamma_f\sin\gamma_p\sin\kappa_r\\ \cos\gamma_p\sin\kappa_r\end{bmatrix} \tag{4.8}$$

$$\kappa_r^* = \operatorname{atan}\left(\frac{v_{edge\,0z}}{v_{edge\,0x}}\right)$$
$$\kappa_r^* = \operatorname{atan}\left(\frac{\cos\gamma_p\sin\kappa_r}{\cos\gamma_f\cos\kappa_r + \sin\gamma_f\sin\gamma_p\sin\kappa_r}\right) \tag{4.9}$$

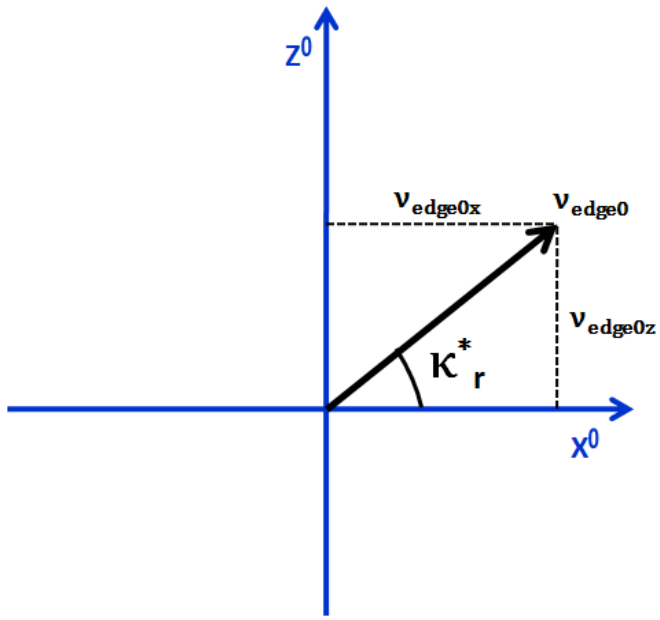

Figure 4-7: Derivation of the True Cutting Edge Angle.

4.4.3 Inclination (Helix) Angle

The inclination angle λ_s is defined as the angle between the cutting edge (X^3) and the tool reference plane P_r (X^0Z^0 plane) measured in tool cutting edge plane P_s. In order to relate the tool design angles, a new coordinate frame must be defined such that the frame F^s has its X^s axis aligned with the tool cutting edge plane P_s, and its Y^s axis aligned with Y^0 axis of the coordinate frame F^0. Figure 4-8 illustrates the frame F^s. Since a rotation of $-\left(\frac{\pi}{2} - \kappa_r\right)$ around the Y^0 axis is needed to align the X^s axis with the plane P_s, the rotation matrix between frames F_0 and F_s becomes:

$$R_{0s} = \begin{bmatrix} \cos(-\kappa_r) & 0 & \sin(-\kappa_r) \\ 0 & 1 & 0 \\ -\sin(-\kappa_r) & 0 & \cos(-\kappa_r) \end{bmatrix} = \begin{bmatrix} \cos(\kappa_r) & 0 & -\sin(\kappa_r) \\ 0 & 1 & 0 \\ \sin(\kappa_r) & 0 & \cos(\kappa_r) \end{bmatrix} \tag{4.10}$$

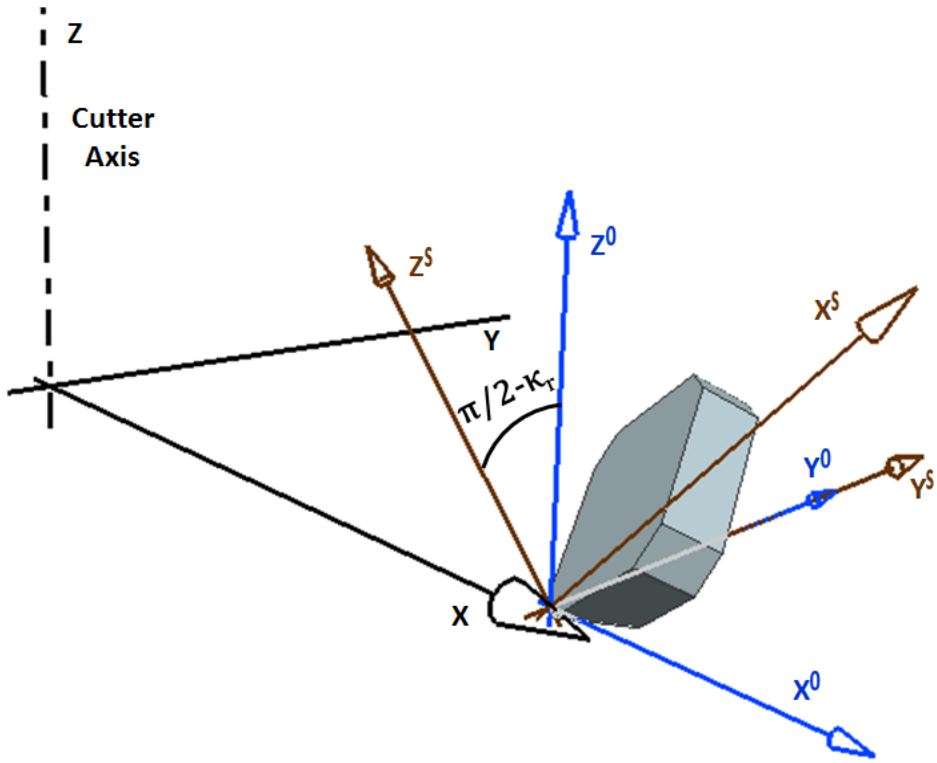

Figure 4-8: Definition of Frame F^s and Frame F^0 to Frame F^s Rotation.

As a result, vector $v_{edg\,e_s}$ can be calculated as:

$$v_{edg\,e_s} = R_{0s}^T\, R_{03}\, v_{edge\,3} = \begin{bmatrix} v_{edg\,e_{sx}} \\ v_{edg\,e_{sy}} \\ v_{edg\,e_{sz}} \end{bmatrix}$$

$$v_{edg\,e_s} = \begin{bmatrix} \cos^2\kappa_r \cos\gamma_f + \cos\kappa_r \sin\gamma_f \sin\gamma_p \sin\kappa_r + \sin^2\kappa_r \cos\gamma_p \\ -\sin\gamma_f \cos\kappa_r + \cos\gamma_f \sin\gamma_p \sin\kappa_r \\ -\sin\kappa_r \cos\gamma_f \cos\kappa_r - \sin^2\kappa_r \sin\gamma_f \sin\gamma_p + \cos\kappa_r \cos\gamma_p \sin\kappa_r \end{bmatrix} \tag{4.11}$$

Following that, the inclination angle λ_s can be defined as the angle between the X^s axis in P_r plane and the edge vector $v_{edg\,e_s}$ with $v_{edg\,e_{sz}}$ component equal to zero.

$$\lambda_s = \operatorname{atan}\left(\frac{v_{edge\_sy}}{v_{edge\_sx}}\right)$$
$$\lambda_s = \operatorname{atan}\left(\frac{-\sin\gamma_f \cos\kappa_r + \cos\gamma_f \sin\gamma_p \sin\kappa_r}{\cos^2\kappa_r \cos\gamma_f + \cos\kappa_r \sin\gamma_f \sin\gamma_p \sin\kappa_r + \sin^2\kappa_r \cos\gamma_p}\right) \tag{4.12}$$

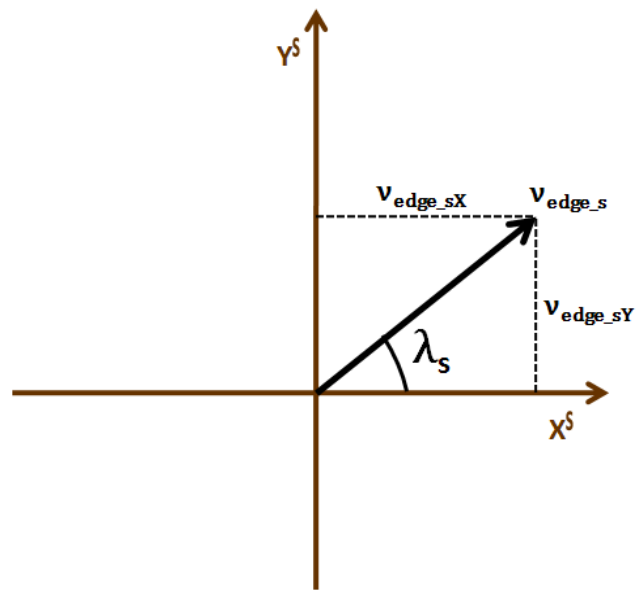

Figure 4-9: Definition of the Inclination (Helix) Angle.

Calculation of these angles is important to determine cutting forces along the cutting edge. In most cases, radial and axial rakes are constant along the cutting edge of the insert, and cutting edge angle changes with the edge modification; it becomes a different constant value along the chamfered corner, and quadratically changes along the round edges. Using the vectors and formulations derived in this chapter, it is possible to calculate the angles at each selected point on the cutting edge. In the next section, as case examples, several different inserts were selected and modeled using the proposed model.

4.5 Examples

4.5.1 Rectangular Insert with Corner Radius

The first selected sample case is a rectangular milling insert with a corner radius. Insert and cutter body geometry were taken from Sandvik Coromant [55]. These dimensions are listed in Table 4-I and illustrated in Figure 4-10.

Table 4-I: Inputs Used in the Model.

Inputs			
$\boldsymbol{L}$ (Insert Length)	11 mm	$\boldsymbol{\kappa_r}$ (Cutting Edge Angle)	90°
$\boldsymbol{iW}$ (Insert Width)	6.8 mm	$\boldsymbol{\gamma_f}$ (Radial Rake Angle)	9°
$\boldsymbol{b_s}$ (Wiper Edge Length)	0.5 mm	$\boldsymbol{\gamma_p}$ (Axial Rake Angle)	10°
$\boldsymbol{r_\varepsilon}$ (Corner Radius)	0.4 mm	$\boldsymbol{\varepsilon_r}$ (Tool Included Angle)	90°
$\boldsymbol{D_c}$ (Cutting Diameter)			20 mm

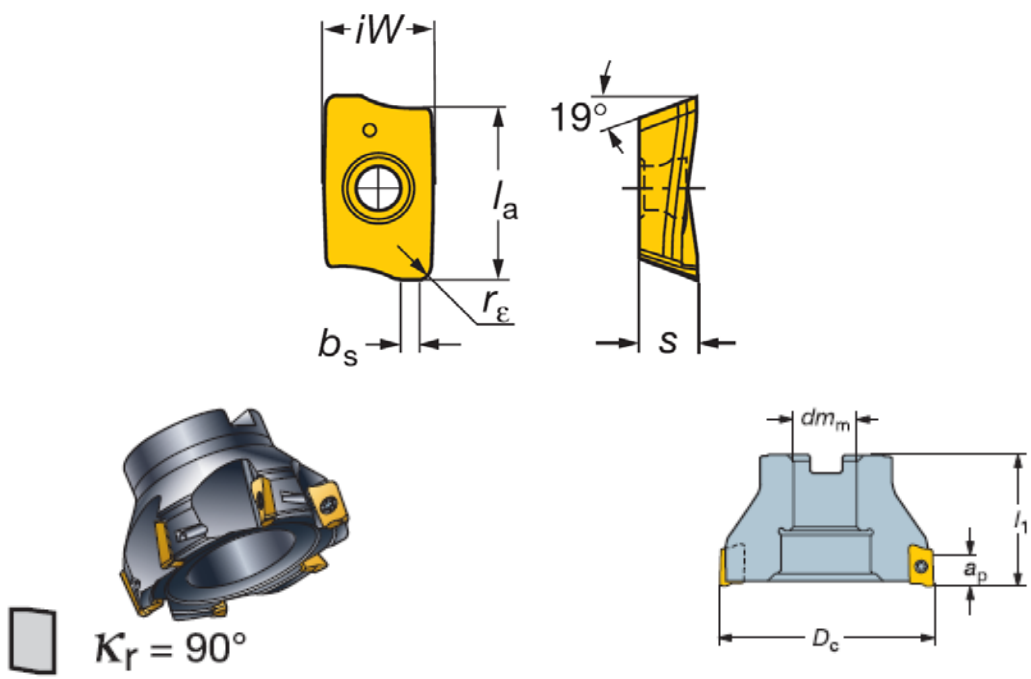

Figure 4-10: Illustrations of the Insert and the Cutter Body [55].

After obtaining the dimensions and the angles required for the placement of the insert on the cutter body, insert center is calculated in (X^0Z^0) plane. In Figure 4-11, insert center is defined by point $I(x, z)$:

$$I_x = \frac{D_c}{2} + r_\varepsilon \sin\kappa_r\,(1-\cos\kappa_r) - \frac{iW\sin\kappa_r}{2} - \frac{r_\varepsilon}{\sin\kappa_r} + \frac{L\cos\kappa_r}{2} + r_\varepsilon\cot\kappa_r - b_s\cos^2\kappa_r \tag{4.13}$$

$$I_z = \frac{-L\sin\kappa_r}{2} + r_\varepsilon\cos\kappa_r - \frac{iW\cos\kappa_r}{2} + b_s\sin\kappa_r\cos\kappa_r - r_\varepsilon\cos^2\kappa_r$$

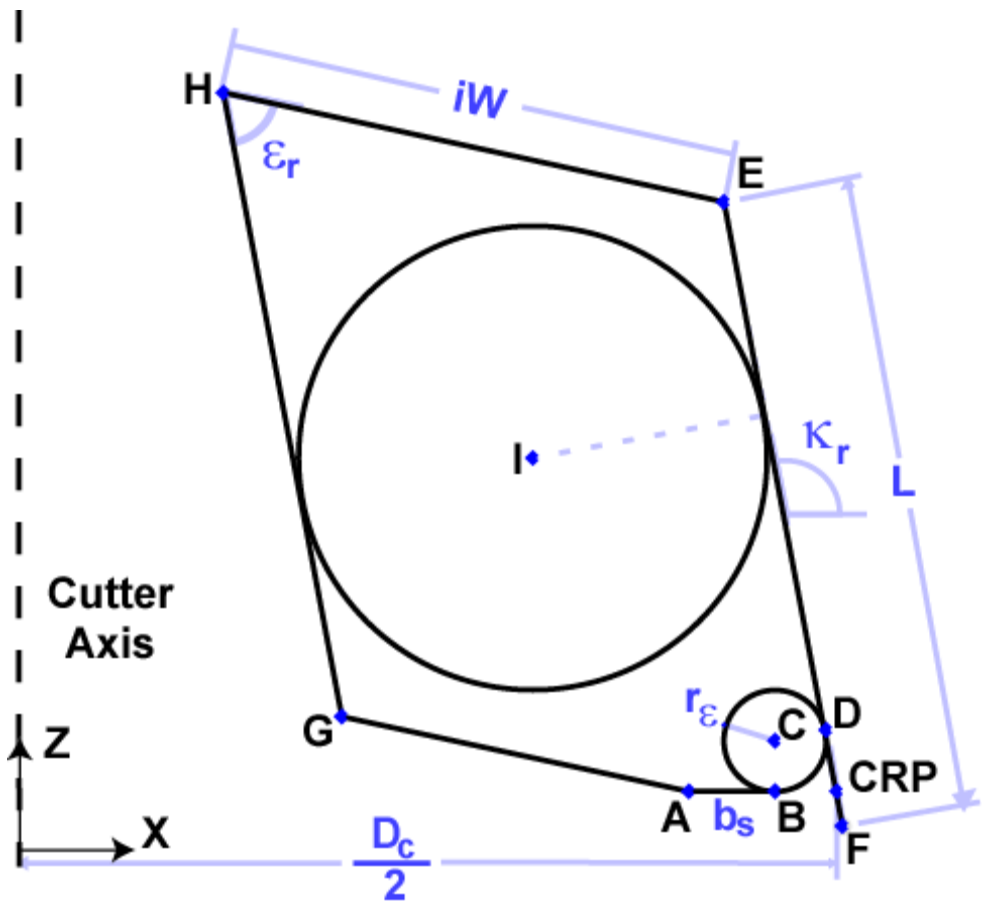

Figure 4-11: Analytical Model of an Insert with a Corner Radius and Wiper Edge.

The second step is to calculate locations of control points which define the cutting edge. In this case, these points are A, B, D, and E. Wiper edge is on the feed plane and defined by a between points A and B. The locations of these points can be calculated as:

$$A_x = -b_s + \frac{D_c}{2} - \frac{r_\varepsilon}{\sin\kappa_r} + r_\varepsilon \cot\kappa_r \quad , \quad A_z = 0 \tag{4.14}$$

$$B_x = \frac{D_c}{2} - \frac{r_\varepsilon}{\sin\kappa_r} + r_\varepsilon \cot\kappa_r \quad , \quad B_z = 0 \tag{4.15}$$

Corner edge is also defined by two points; points B and D. Similarly, location of point D can be calculated by the following equations:

$$D_x = \frac{D_c}{2} + r_\varepsilon \sin\kappa_r - \frac{r_\varepsilon}{\sin\kappa_r} + \frac{r_\varepsilon \cos\kappa_r}{\sin\kappa_r} \quad , \quad D_z = |r_\varepsilon(-1 + \cos\kappa_r)| \tag{4.16}$$

Since there are only two symmetrical edges on a rectangular insert (Figure 4-10), corner modification is present only at two corners, thus main cutting edge is defined by points D and E. The position of point E can be calculated as:

$$\begin{aligned} E_x &= \frac{D_c}{2} + r_\varepsilon \sin\kappa_r - \frac{r_\varepsilon}{\sin\kappa_r} + (-b_s + r_\varepsilon \cot\varepsilon_r)\cos^2\kappa_r \\ &\quad + \left(L - r_\varepsilon \sin\kappa_r + \frac{r_\varepsilon}{\sin\kappa_r} - r_\varepsilon \cot\varepsilon_r - b_s \sin\kappa_r \cot\varepsilon_r\right)\cos\kappa_r \\ E_z &= |-L\sin\kappa_r + b_s \cot\varepsilon_r + r_\varepsilon \sin\kappa_r \cot\varepsilon_r + (-r_\varepsilon - b_s \cot\varepsilon_r)\cos^2\kappa_r \\ &\quad + (r_\varepsilon + b_s \sin\kappa_r - r_\varepsilon \sin\kappa_r \cot\varepsilon_r)\cos\kappa_r| \end{aligned} \tag{4.17}$$

After the calculation of control points and the cutting edges between these points, cutting edge is defined in (X^0Z^0) plane in two dimensions. Rotation about Y^0 axis by κ_r has been already implemented in these equations in order to make sure that the wiper edge is parallel to (XY) plane. Moreover, these locations were defined in global XYZ coordinate frame with the tool tip as origin, therefore, these points must be translated to cutting reference point then the rotations presented in Section 4.3 must be performed.

Transformations from a fixed frame is not commonly used in robotics, however, placement of the insert on the cutter body is a fixed frame transformation. Fixed frame transformation matrix can be calculated by taking the inverse of the current frame transformation using the same rotations [56]. After the rotations, all control points were transformed back to global XYZ coordinate frame. Following figures show the locations of the control points before and after the transformations in global coordinate system.

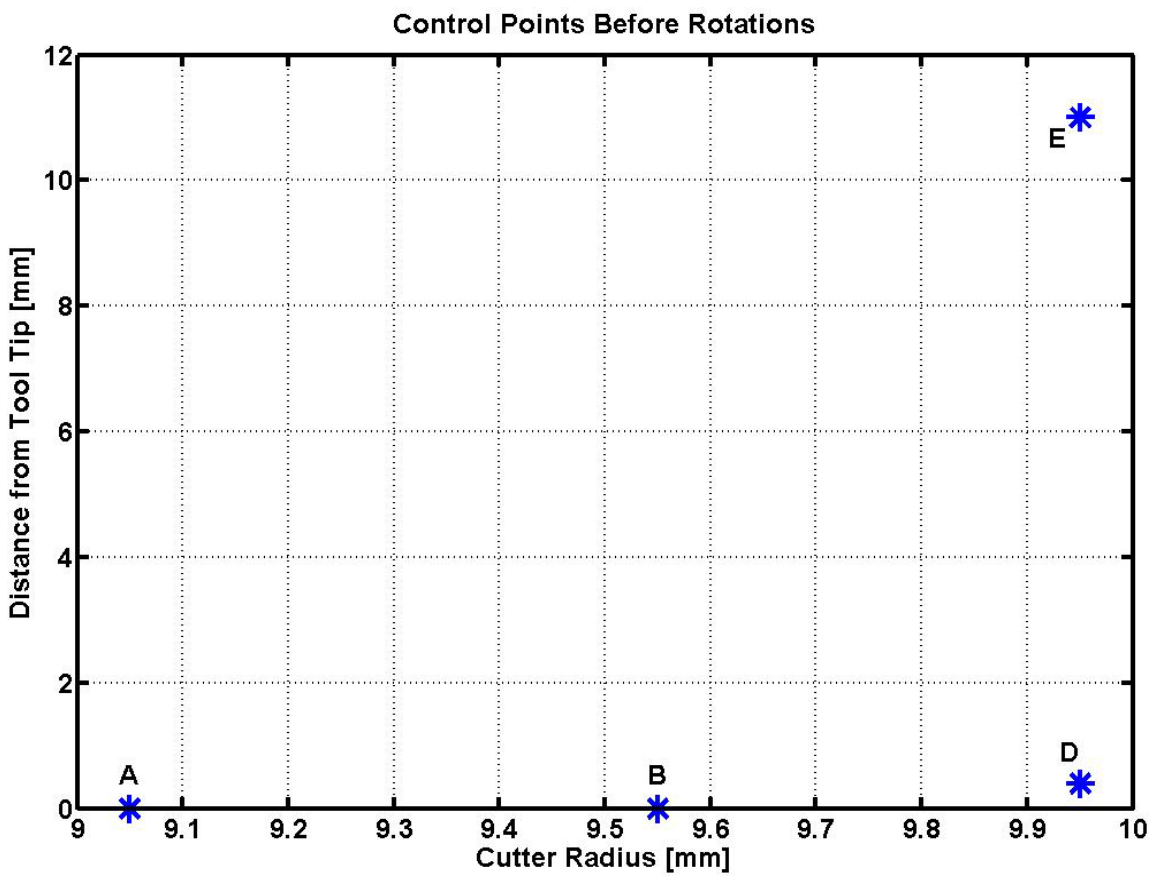

Figure 4-12: Control Points of the Insert before the Rotations.

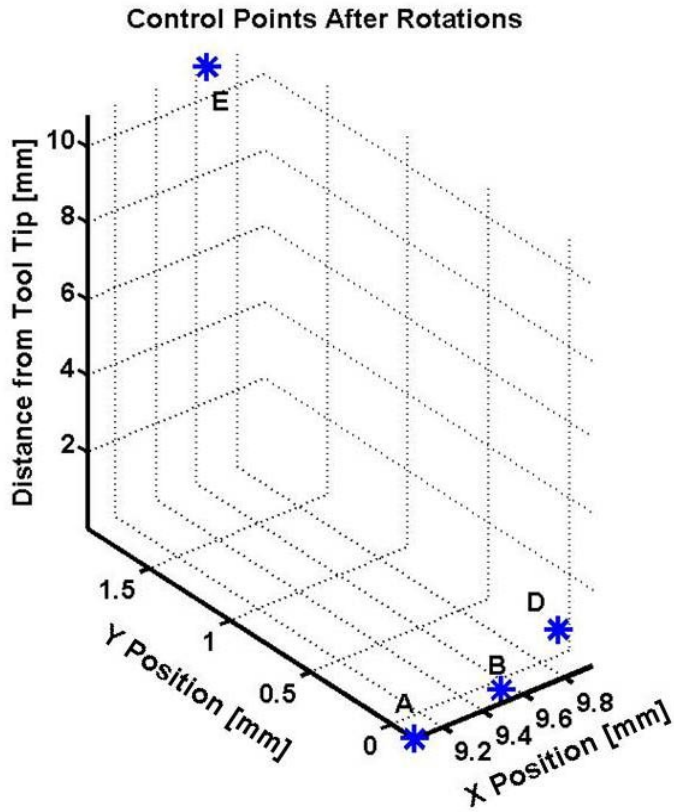

Figure 4-13 : Control Points of the Insert after the Rotations.

Following the rotations of the control points, lines and arcs between the consecutive points were defined in three dimensions. Since the performed rotations were solid body rotations, the relationship between any consecutive points would be same. However, these lines and arcs were no longer in (X^0Z^0) plane; therefore, parametric equations were defined to obtain the location of each selected point on the cutting edge.

For linear cutting edges:

$$P = \vec{P}_{i-1} + \left(\vec{P}_i - \vec{P}_{i-1}\right) t \quad , \quad 0 \leq t \leq 1 \tag{4.18}$$

For arcs:

$$P = R \cos t\, \vec{u} + R \sin t\ \vec{n} \times \vec{u} + C, \quad 0 \leq t \leq \frac{\pi}{2} \tag{4.19}$$

where P is any point between $\vec{P}_i$ and $\vec{P}_{i-1}$ which are two consecutive control points, R is the radius of the arc, $\vec{u}$ is a unit vector from the center of the arc to any point on the circumference, $\vec{n}$ is a unit vector perpendicular to the plane of the arc, and C is the center vector of the arc. Note that these equations are parametric equations, in order to calculate the positions along the cutter axis, the relationship between any axial point and corresponding parameter value should be calculated. During the calculation of geometric control points, cutting edge shape between any two consecutive points are stored and during the general model, corresponding parametric equation is called automatically. The radius of any point on the cutting edge can be calculated by a point – line distance equation in space. Hence:

$$r = \frac{\left|(\vec{Z}_2 - \vec{Z}_1) \times (\vec{Z}_1 - \vec{P})\right|}{\left|\vec{Z}_2 - \vec{Z}_1\right|} \tag{4.20}$$

where r is the local radius, $\vec{Z}_1$ and $\vec{Z}_2$ are any two points along the cutter axis. Using these formulations and rotation matrix developed in section 4.3, it is possible to calculate the local radius, normal rake angle, and helix angle of any point on the cutting edge of the insert.

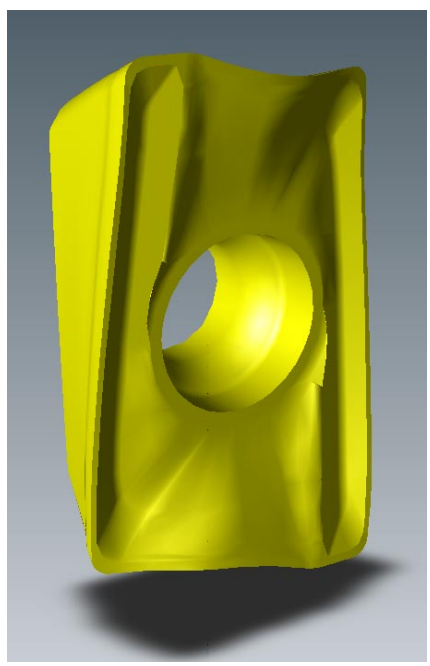

Figure 4-14: CAD Model of the Insert.

Figure 4-15 shows the local radii of the insert along the cutter axis with comparison of the local radii extracted from the CAD part of the insert which is shown in Figure 4-14. As stated before, this model is valid for flat inserts; therefore, due to the complexity of the insert geometry, mathematical model and CAD data does not match perfectly. However, the error is acceptable; since the maximum error between the model and the insert is around 50 microns. Figure 4-16 and Figure 4-17 show the change in the normal rake angle and helix angle along the cutter axis respectively.

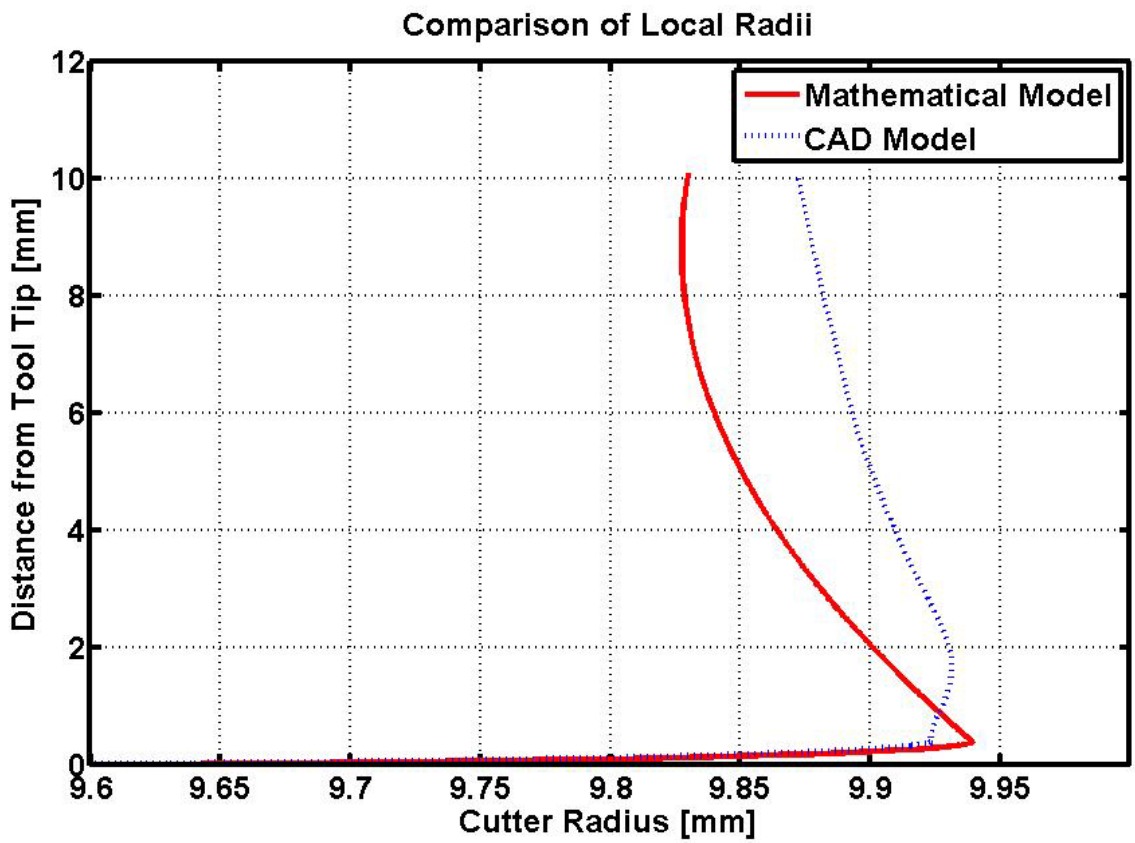

Figure 4-15: Change of Local Radius along the Tool Axis.

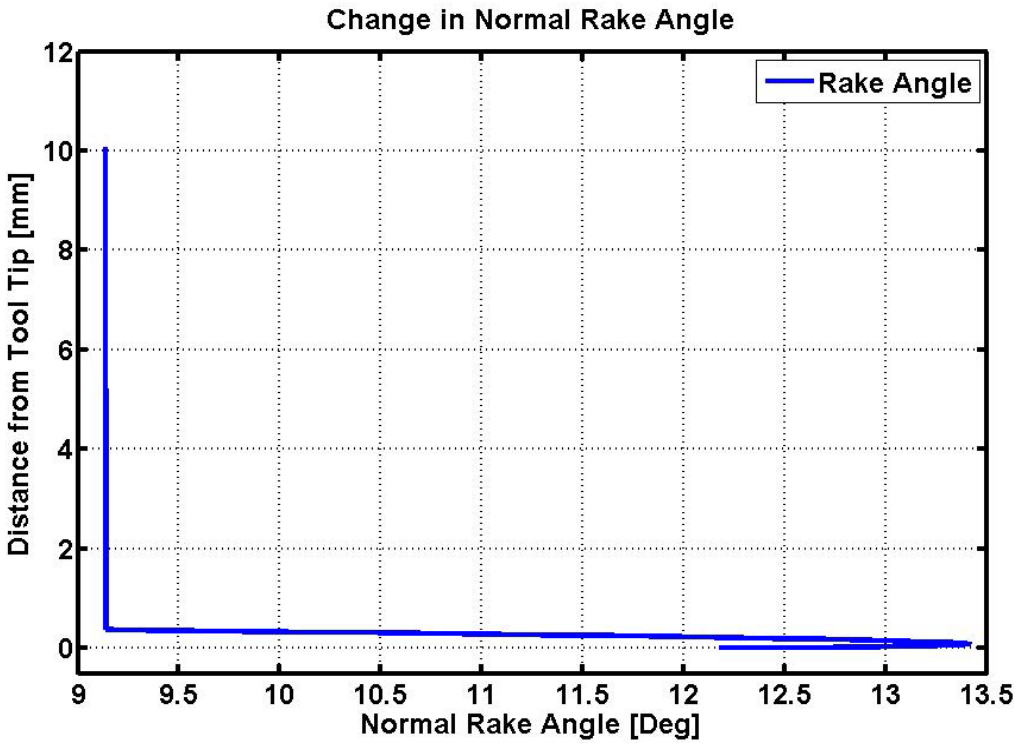

Figure 4-16: Change in Normal Rake Angle along the Tool Axis.

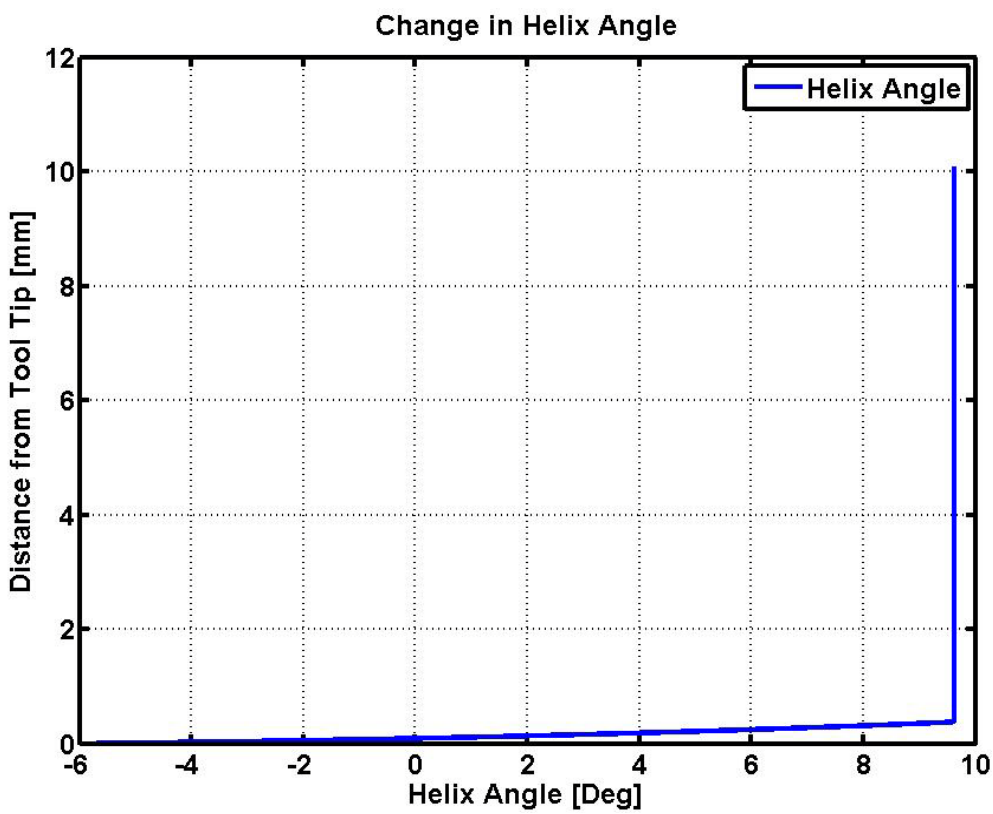

Figure 4-17: Change in Helix Angle along the Tool Axis.

4.5.2 Rectangular Insert with Corner Chamfer

Similar procedure was applied to an insert with a chamfered corner. Table 4-II and Figure 4-18 show the angles and dimensions of the insert.

Table 4-II: Inputs Used in the Analysis of the Insert with Chamfer.

Inputs			
$\boldsymbol{L}$ (Insert Length)	11 mm	$\boldsymbol{\kappa_r}$ (Cutting Edge Angle)	90°
$\boldsymbol{iW}$ (Insert Width)	11.5 mm	$\boldsymbol{\gamma_f}$ (Radial Rake Angle)	5°
$\boldsymbol{b_s}$ (Wiper Edge Length)	1.5 mm	$\boldsymbol{\gamma_p}$ (Axial Rake Angle)	5°
$\boldsymbol{K_\varepsilon}$ (Corner Chamfer)	1 mm x45°	$\boldsymbol{\varepsilon_r}$ (Tool Included Angle)	90°
$\boldsymbol{D_c}$ (Cutting Diameter)			63 mm

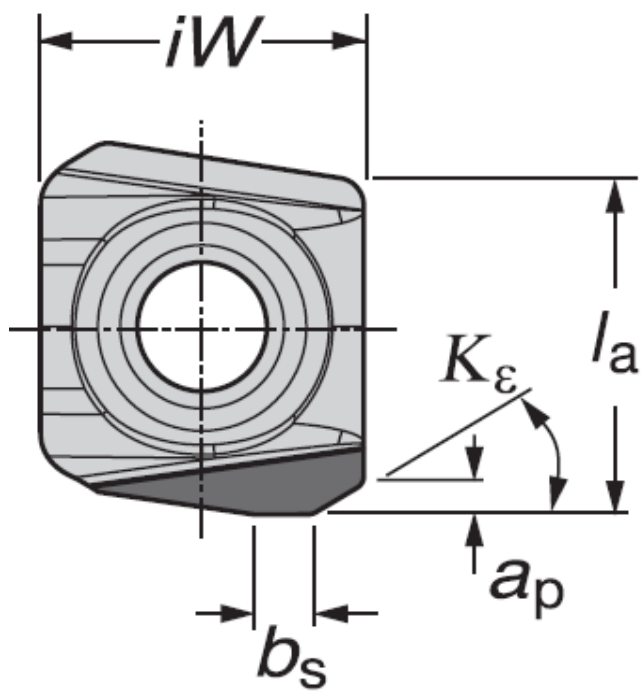

Figure 4-18: Catalogue Figure of the Insert Taken from Sandvik Coromant [55].

Analytical model of the insert can be seen in Figure 4-19. Insert center is defined by point I. Coordinates of this point in $(X^0 Z^0)$ plane is:

$$I_x = \frac{1}{2}\Big|D_c + iW\cos(\varepsilon_r + \kappa_r)\csc\varepsilon_r + \cos\kappa_r\,(L - 2b_s\csc\varepsilon_r\sin(\varepsilon_r + \kappa_r)) - 2bch\cot\kappa_r\csc\varepsilon_r\sin(\varepsilon_r + \kappa_r)\sin(\kappa_r - K_\varepsilon)\Big| \tag{4.21}$$

$$I_z = \frac{1}{2}\Big|\csc\varepsilon_r\,\big(L\sin\varepsilon_r\sin\kappa_r + \sin(\varepsilon_r + \kappa_r)\,(iW - 2b_s\sin\kappa_r - 2bch\sin(\kappa_r - K_\varepsilon))\big)\Big|$$

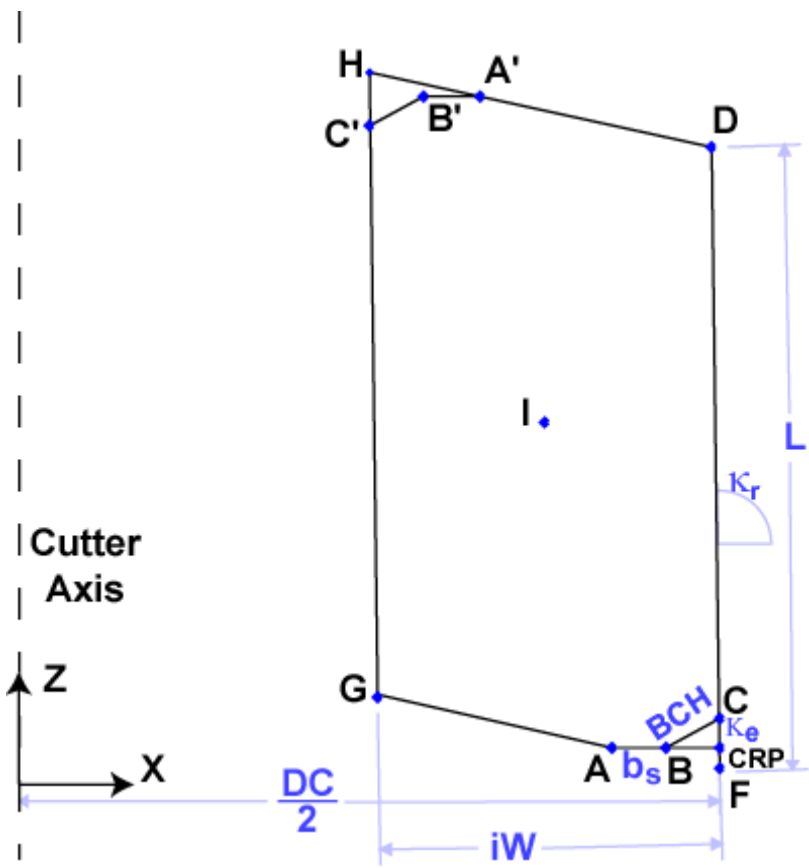

Figure 4-19: Illustration of Control Points and Dimensions for an Insert with Chamfer.

For this type of insert, control points are points $A, B, C,$ and D. Locations of these points can be calculated as the following:

$$A_x = -b_s + \frac{D_c}{2} + BCH \sin K_\varepsilon \cot \kappa_r - BCH \cos K_\varepsilon \quad , \quad A_z = 0 \tag{4.22}$$

$$B_x = \frac{D_c}{2} + BCH \sin K_\varepsilon \cot \kappa_r - BCH \cos K_\varepsilon \quad , \quad B_z = 0 \tag{4.23}$$

$$C_x = \frac{D_c}{2} + BCH \sin K_\varepsilon \cot \kappa_r \quad , \quad C_z = BCH \sin K_\varepsilon \tag{4.24}$$

$$\begin{aligned} D_x = \Big| & b_s - \frac{D_c}{2} - L \cos \kappa_r + b_s \cos(\varepsilon_r + \kappa_r) \csc \varepsilon_r \sin \kappa_r \\ & + bch \cot \kappa_r \csc \varepsilon_r \sin(\varepsilon_r + \kappa_r) \sin(\kappa_r - K_\varepsilon) \Big| \end{aligned} \tag{4.25}$$

$$D_z = |L \sin \kappa_r - \csc \varepsilon_r \sin(\varepsilon_r + \kappa_r) \, (b_s \sin \kappa_r + bch \sin(\kappa_r - K_\varepsilon))|$$

After the calculations of the locations of control points in $(X^0 Z^0)$ plane, same procedure explained in the previous example is applied. As a result, tool angles and local radii were calculated along the cutting edge of this insert. Following figures illustrate these results.

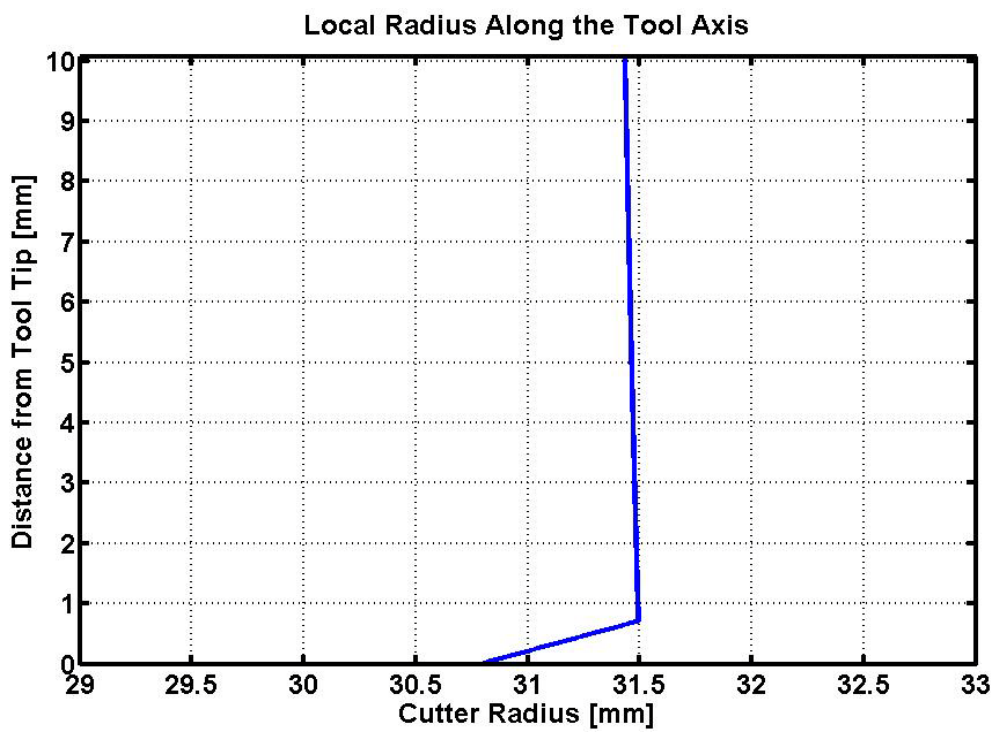

Figure 4-20: Change in the Local Radius along the Tool Axis for a Chamfered Insert.

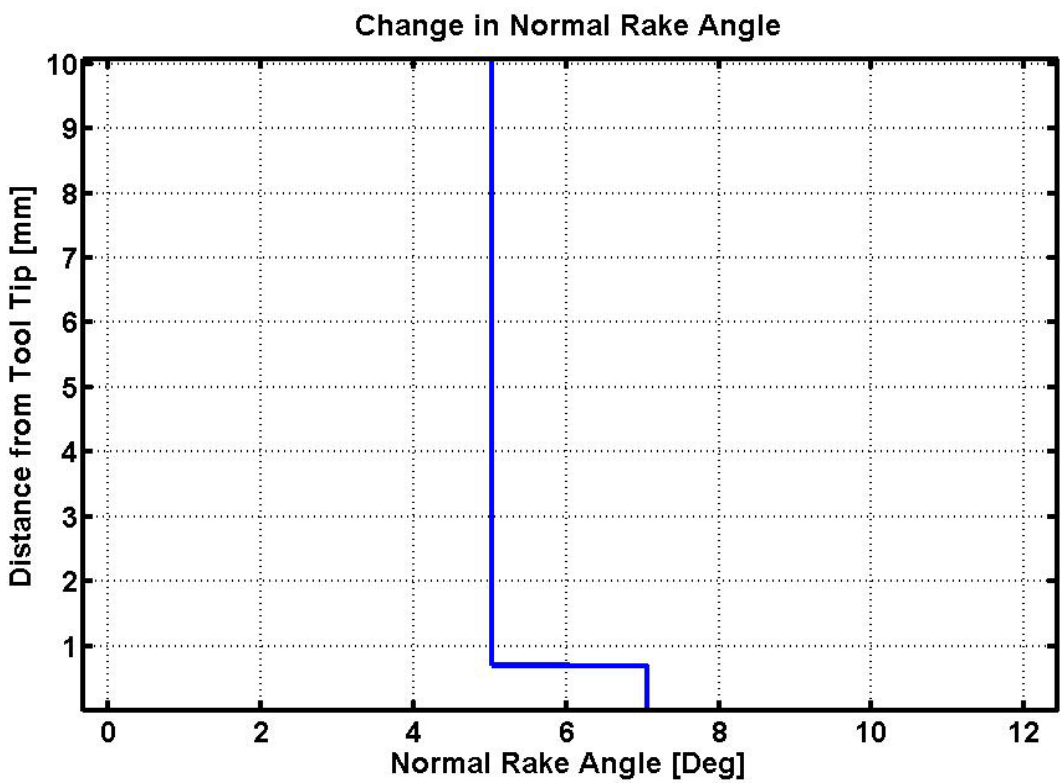

Figure 4-21: Change in Normal Rake Angle along the Tool Axis.

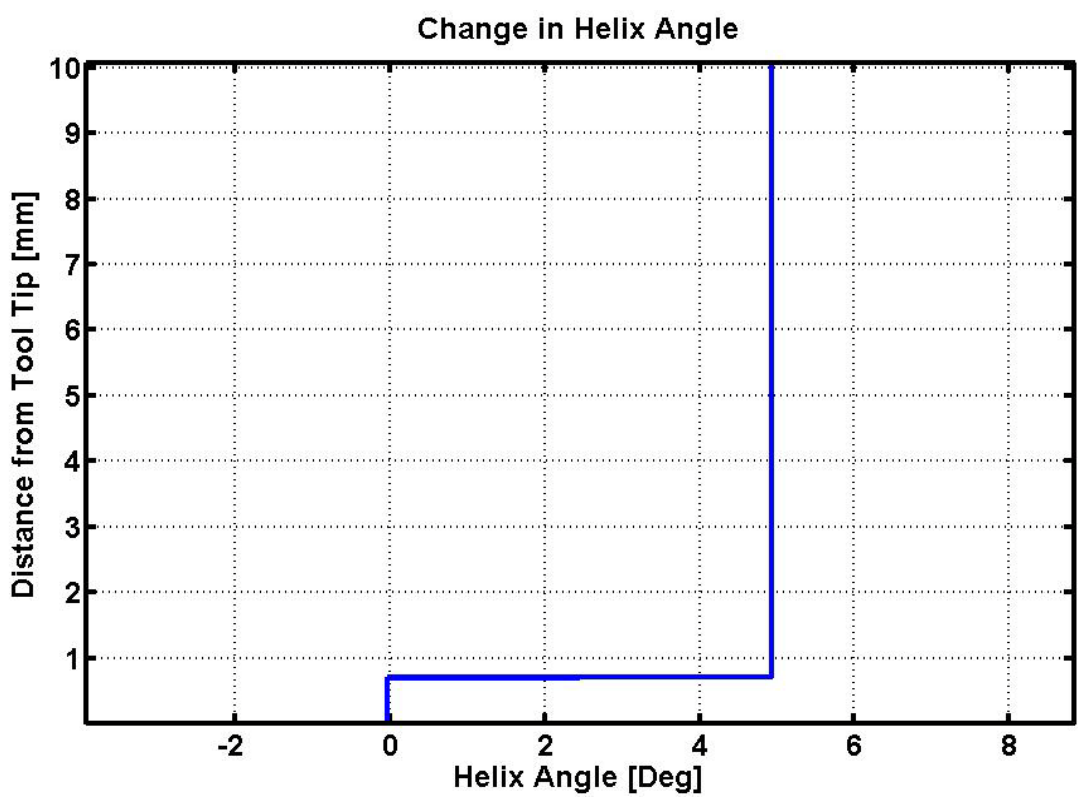

Figure 4-22: Change in Helix Angle along the Tool Axis.

4.5.3 Rhombic Turning Insert

As stated before, geometric model of inserted cutters can be applied not only for milling inserts, but also turning inserts. For that purpose, a rhombic (diamond) shaped insert was selected for analysis. Table 4-III and Figure 4-23 show the insert geometry.

Table 4-III: Inputs for the Rhombic Turning Insert.

Inputs			
$\boldsymbol{L}$ (Insert Length)	15 mm	$\boldsymbol{\kappa_r}$ (Cutting Edge Angle)	93°
$\boldsymbol{iW}$ (Insert Width)	-	$\boldsymbol{\gamma_f}$ (Radial Rake Angle)	-8°
$\boldsymbol{b_s}$ (Wiper Edge Length)	-	$\boldsymbol{\gamma_p}$ (Axial Rake Angle)	-10°
$\boldsymbol{r_\varepsilon}$ (Corner Radius)	1.6 mm	$\boldsymbol{\varepsilon_r}$ (Tool Included Angle)	55°

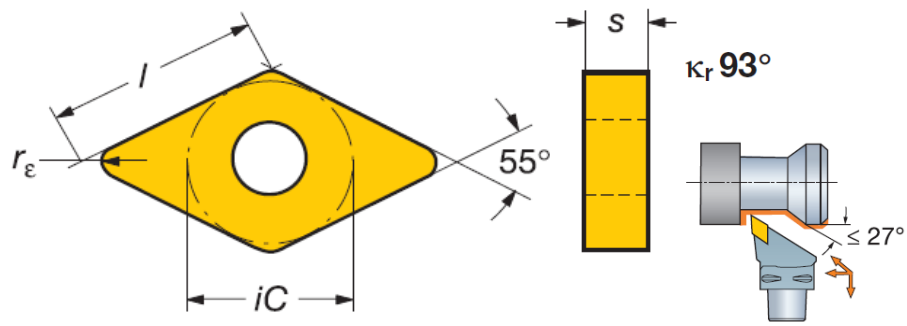

Figure 4-23: Catalogue Figures of the Turning Insert [55].

In the analysis of turning tools, similar procedure to previous examples was applied with some certain modifications. Since turning tools do not rotate, D_c (Cutting Diameter) is not defined. Moreover, wiper edge was also not considered for turning tools. As a result, instead of tool axis tip, intersection between cutting edge and feed plane (Point A in Figure 4-24) was selected as the origin of the global coordinate system. Figure 4-24 shows the variable and control points used in the analysis of this type of insert.

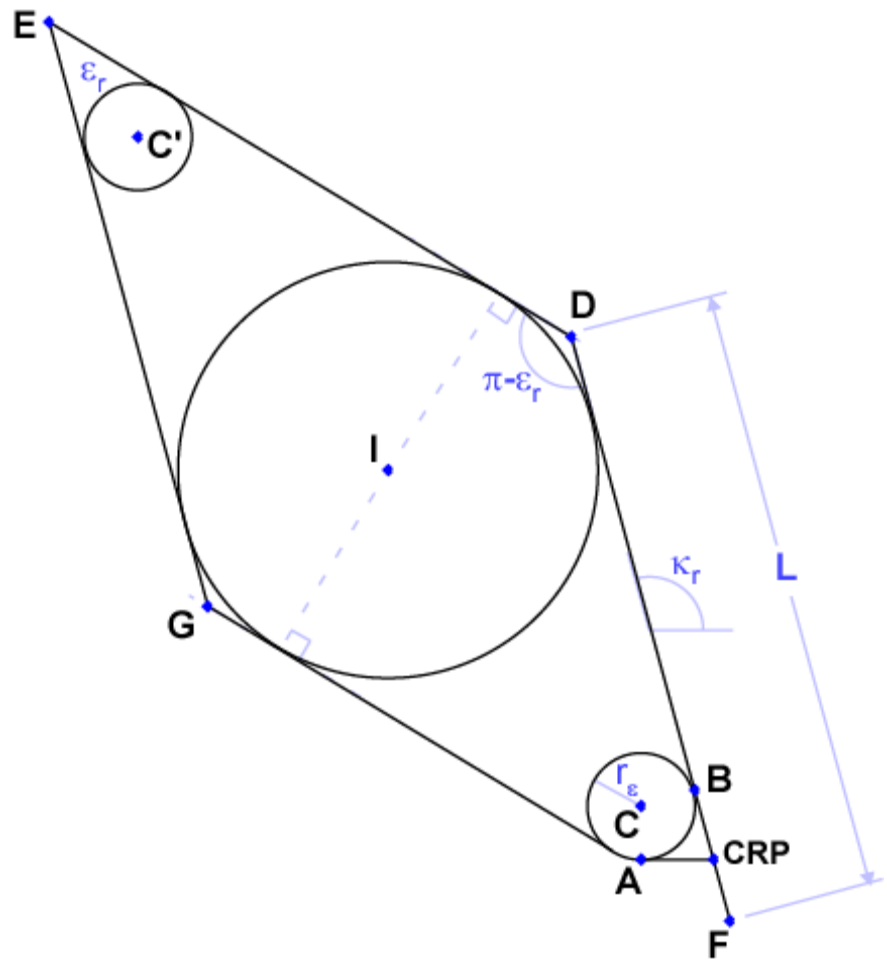

Figure 4-24: Control Points of the Rhombic Turning Insert.

Location of insert center with respect to the point A can be calculated as:

$$
\begin{aligned}
I_x &= \frac{(-L + 2r_\varepsilon \sin\varepsilon_r + L\cos^2\varepsilon_r)\sin\kappa_r}{2\sin\varepsilon_r} \\
&\quad + \frac{(-2r_\varepsilon + L\sin\varepsilon_r - 2r_\varepsilon\cos\varepsilon_r + L\sin\varepsilon_r\cos\varepsilon_r)\cos\kappa_r}{2\sin\varepsilon_r} \\
I_z &= r_\varepsilon + \frac{L\sin\kappa_r}{2}(1+\cos\varepsilon_r) - \frac{r_\varepsilon\sin\kappa_r}{\sin\varepsilon_r} - r_\varepsilon\sin\kappa_r\cot\varepsilon_r - r_\varepsilon\cos\kappa_r \\
&\quad + \frac{L\cos\kappa_r - L\cos^2\varepsilon_r\cos\kappa_r}{2\sin\varepsilon_r}
\end{aligned}
\tag{4.26}
$$

The locations of control points A, B, and D can be described as the following equations. The results of the model are shown in the following figures.

$$A_x = 0 \quad , \quad A_z = 0 \tag{4.27}$$

$$B_x = r_\varepsilon \sin \kappa_r \quad , \quad B_z = r_\varepsilon (1 - \cos \kappa_r) \tag{4.28}$$

$$\begin{aligned} D_x &= r_\varepsilon \sin \kappa_r + \left(L - \frac{r_\varepsilon}{\sin \varepsilon_r} - r_\varepsilon \cot \varepsilon_r \right) \cos \kappa_r \\ D_z &= r_\varepsilon + L \sin \kappa_r - \frac{r_\varepsilon \sin \kappa_r}{\sin \varepsilon_r} - r_\varepsilon \sin \kappa_r \cot \varepsilon_r - r_\varepsilon \cos \kappa_r \end{aligned} \tag{4.29}$$

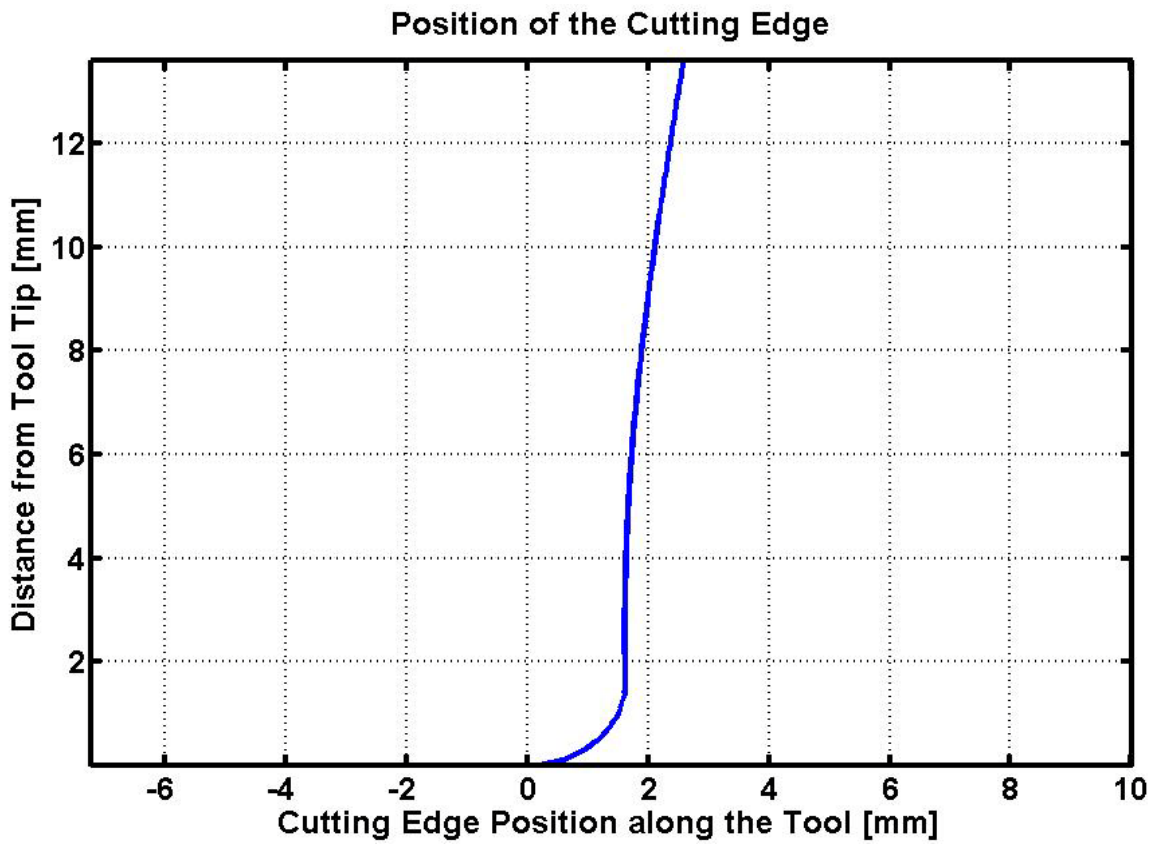

Figure 4-25: Position of the Cutting Edge for a Rhombic Turning Insert.

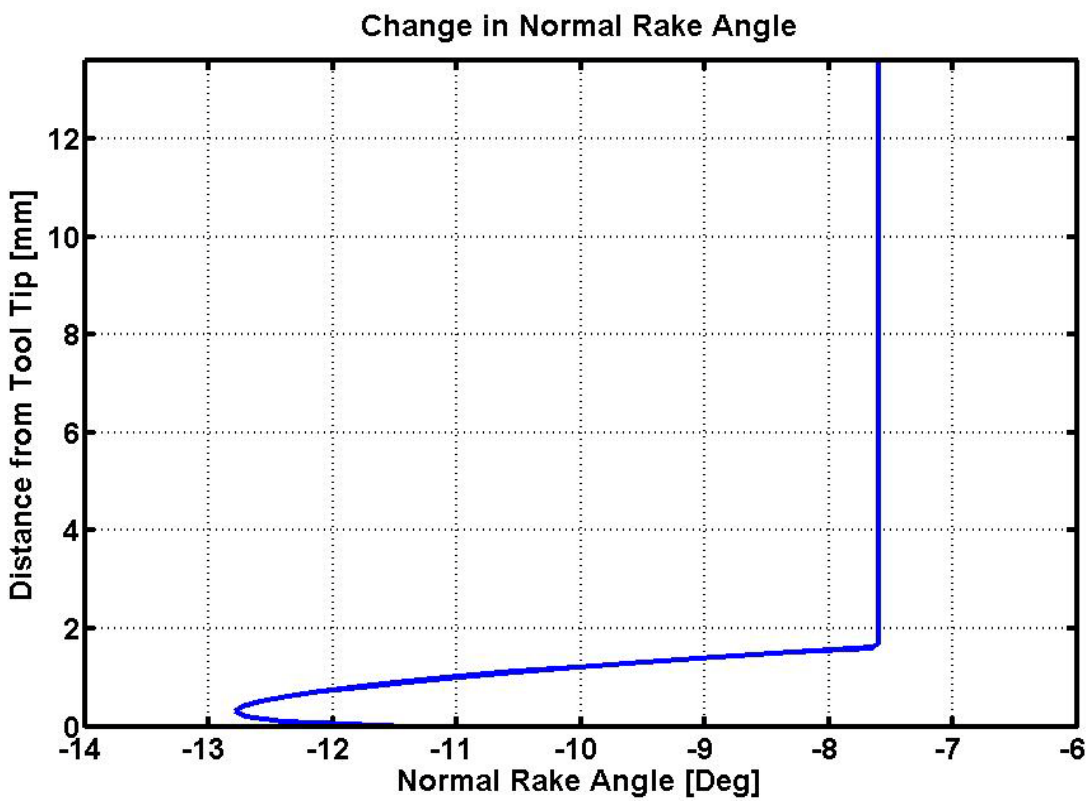

Figure 4-26: Change in the Normal Rake Angle along the Cutting Edge.

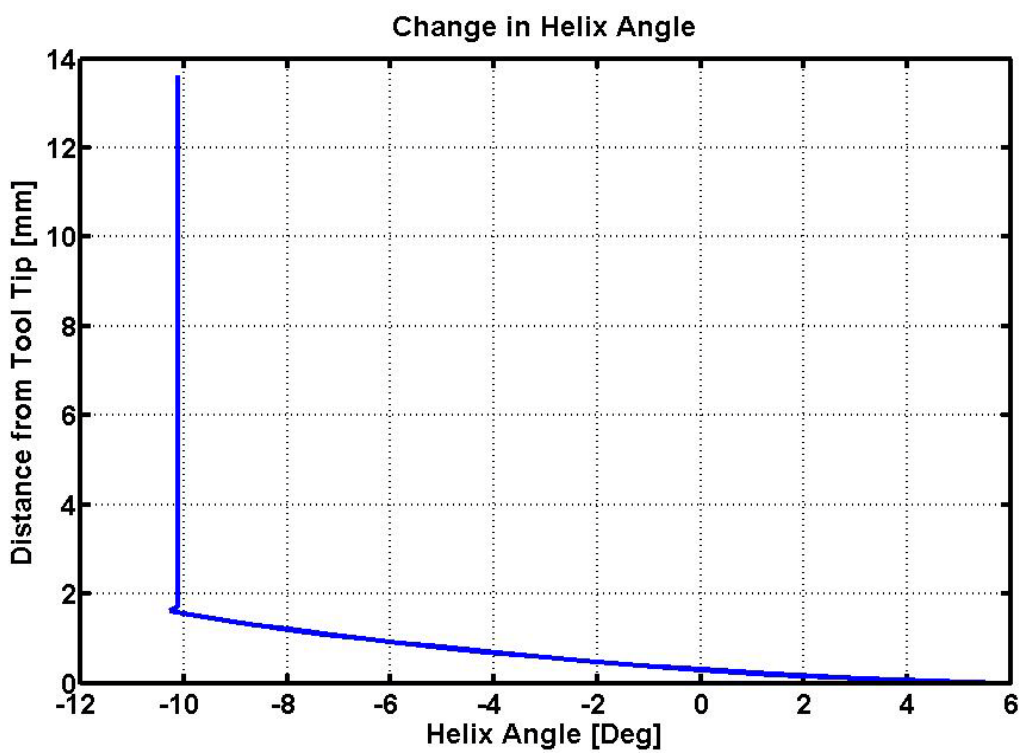

Figure 4-27: Change in the Helix Angle along the Cutting Edge.

4.6 Summary

In this chapter, the analytical calculations needed to define and orient the cutting edge on a cutter or tool holder is presented. Variables used in the equations have been obtained from ISO standards ISO 3002 and ISO 13399. It is shown that for any type of insert geometry, it is possible to define the cutting edge on the tool axis and to convert from design angles to physical angles.

From the definitions and transformation equations, it can be observed that normal rake angle γ_n and helix (inclination) angle λ_s are functions of the cutting edge angle κ_r, radial rake angle γ_f, and axial rake angle γ_p. As a result, any change in one of these angles along the cutting edge alters others. However, in this study, axial and radial rake angles are kept constant; therefore, changes observed in helix and normal rake angles in the presented figures are due to the cutting angle changes along the corner modifications. For instance, for an insert with -10° axial rake and -8° radial rake, as the cutting edge angle changes from 0° to 93°, normal rake angle changes from -13° to -9° and the helix angle changes from +6° to -10° along 1.6 mm corner radius.

In the next chapter, generalized mechanics of metal cutting is presented. A new cutting force model which is applicable to different cutting processes is introduced and simulations are presented with experimental verifications.

5. Generalized Mechanics of Metal Cutting

5.1 Overview

In this chapter, generalized modeling of cutting forces using the mechanics on the rake face, the friction force F_u and the normal force F_v, is presented. The generalized model is compared with the current cutting force models in the literature, and the relationships between the models are presented.

In addition to cutting force models, calibration and material models are summarized and their transformations to the proposed model are presented. With this information, it is possible to convert most of the models currently being used in the literature to the proposed model.

5.2 Rake Face Based General Force Model

The normal and friction forces on the rake face are used as the base in predicting the cutting forces in the machining system. Figure 5-1 shows a sample oblique cutting process with all the variables used in this study. In Figure 5-1, $\vec{F}$ is the total resultant force, $\overrightarrow{F_u}$ is the friction force on the rake face, $\overrightarrow{F_v}$ is the normal force on the rake face, $\overrightarrow{F_s}$ and $\overrightarrow{F_n}$ are the shearing and normal forces acting on the shear plane respectively, γ_n is the rake angle, λ_s is the inclination / helix angle, η is the chip flow angle, ϕ_n is the normal shear angle, β_a is the friction angle, and finally, b and h are the width of cut and uncut chip thickness respectively.

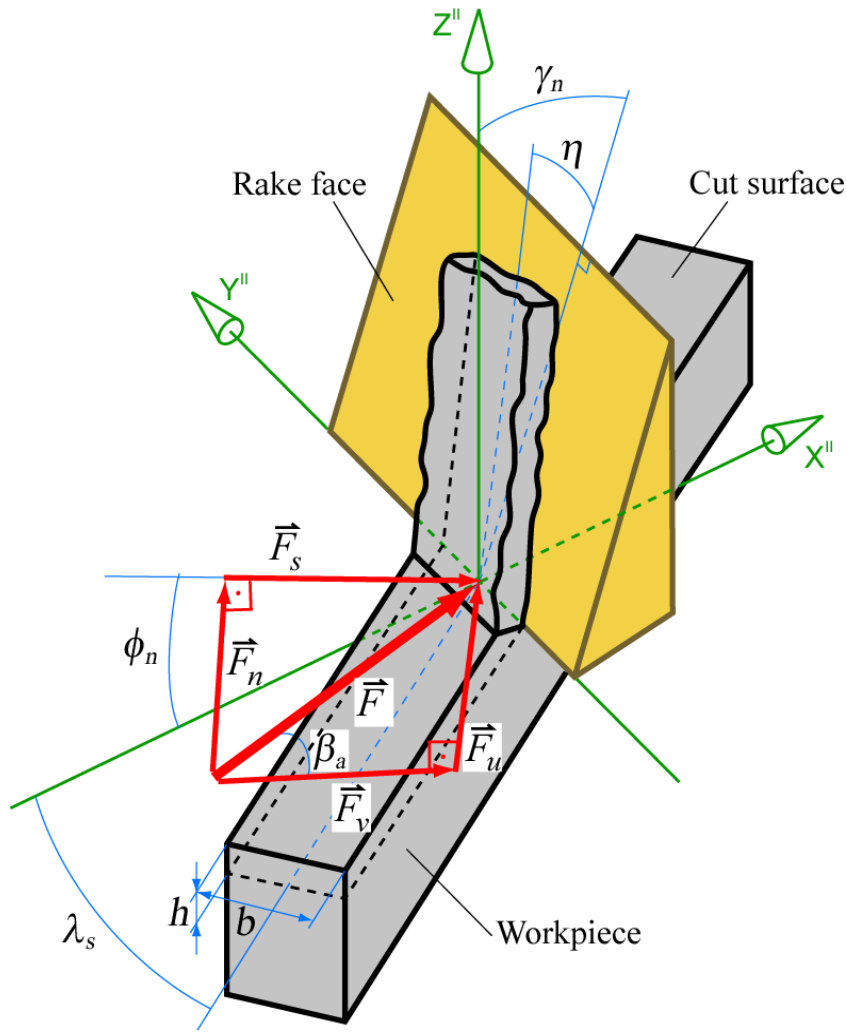

Figure 5-1: Mechanics of Oblique Cutting [11].

For a differential chip load (dA_c) in an engagement with a selected point on the cutting edge of the tool, the differential friction (dF_u) and the differential normal force (dF_v) acting on the rake face can be expressed as,

$$\begin{aligned} dF_u &= K_{uc}\ dA_c + K_{ue}\ dS \\ dF_v &= K_{vc}\ dA_c + K_{ve}\ dS \end{aligned} \tag{5.1}$$

where K_{uc} and K_{vc} are the friction and normal cutting coefficients and K_{ue} and K_{ve} are the related edge coefficients. These specific cutting coefficients depend on the tool – workpiece combination. For a specific workpiece, these cutting coefficients can be described as a function of chip thickness, rake angle, and the cutting speed (V_c), they are called size, geometry and speed effects, respectively. The identification of the cutting

force coefficients are explained in the following sections. In Eq. (5.1), dA_c and dS are differential chip area and differential cutting edge length can be calculated with the following;

$$dA_c = h\,b$$
$$dS = b_{eff} = \frac{b}{\sin \kappa_r} \tag{5.2}$$

Once the differential friction (dF_u) and differential normal (dF_v) cutting forces are evaluated through the use of Eq. (5.1), they can be transformed into machine coordinate system (XYZ) with procedure described in Chapter 4.3. Since the tool geometry (rake, helix, cutting edge angles) may change along the cutting edge of the tool, these transformations must be repeated for each differential part of the cutting edge(s). After the transformation process, the differential forces are summed to determine the total cutting forces acting on the machine coordinates (F_x, F_y, and F_z), as:

$$\begin{bmatrix} F_x \\ F_y \\ F_z \end{bmatrix} = \sum_{n=1}^{N_f} \sum_{k=1}^{K} \begin{bmatrix} dF_x \\ dF_y \\ dF_z \end{bmatrix}\Bigg|_{k,n} \tag{5.3}$$

where N_f is the total number of cutting edges and K represents the total number of discrete points along the cutting edge n. Proposed cutting force model is summarized in Figure 5-2.

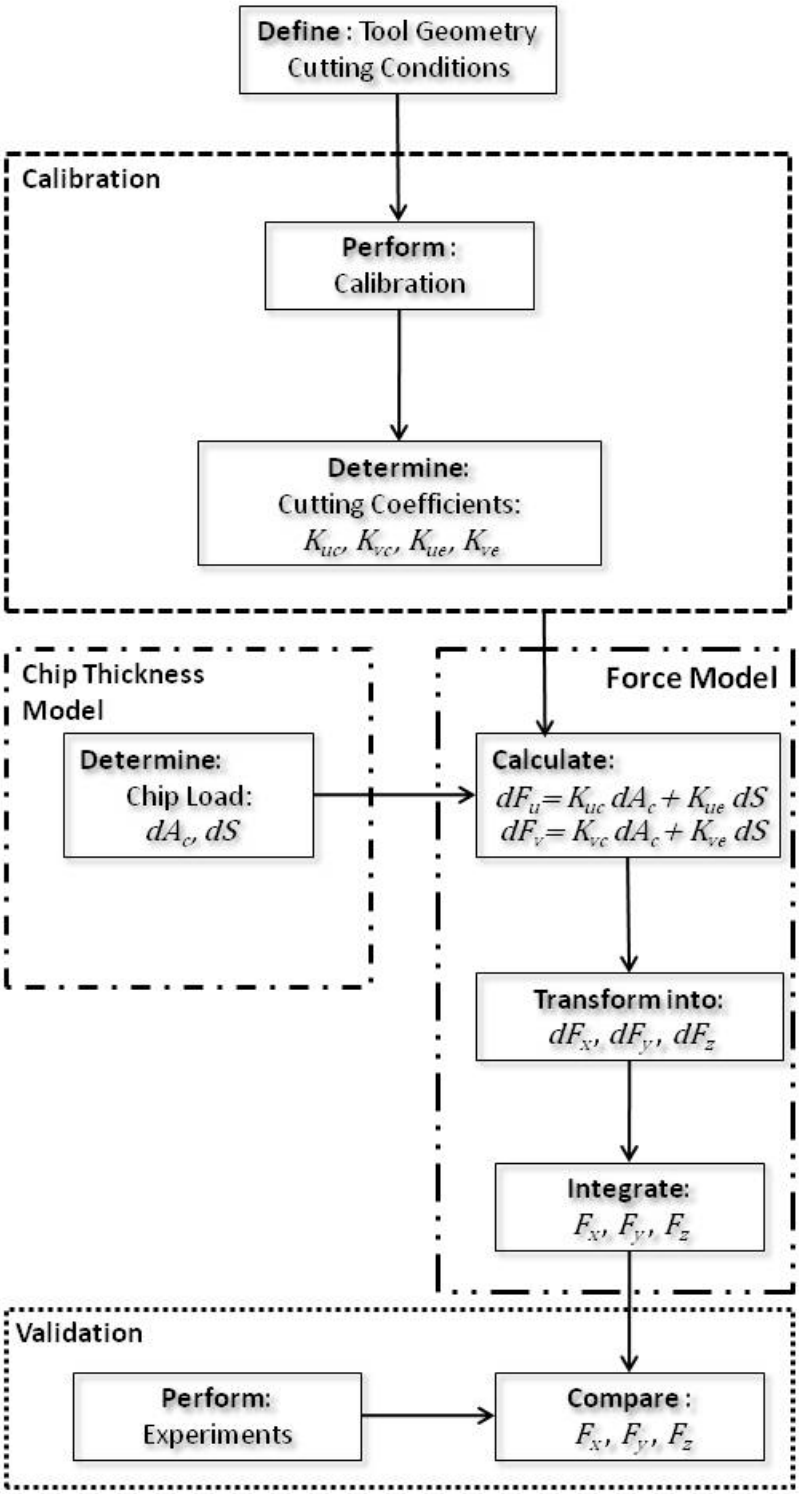

Figure 5-2: Summary of the Proposed Mechanistic Approach.

5.3 Identification of Specific Cutting Coefficients

Accurate determination of cutting force coefficients is critical to cutting force prediction. There are several parameters influencing the cutting force coefficients and they can be estimated either mechanistically or using classical orthogonal to oblique transformation method. The cutting force coefficients depend on:

- Cutting Method : constant or varying chip volume removal (Turning vs. Milling)
- Cutting Conditions: feed rate, depth of cut, cutting speed, use of coolant;
- Workpiece Material: chemical composition;
- Tool: tool material, chip breaker, tool wear.

Since it is not possible to account for all of these variables simultaneously, only the effects of chip thickness, cutting speed, and normal rake angle have been considered which are most dominant. In the following sections, both mechanistic approach and classical approach are explained in detail to determine the specific cutting coefficients in friction (K_u) and normal (K_v) directions.

5.3.1 Orthogonal to Oblique Transformation

Orthogonal cutting tests can be used to calculate the shear stress (τ_s), shear angle (ϕ_c), and the friction angle (β_a) as a function of chip thickness, rake angle, and cutting speed. However, cutting edge(s) are usually not orthogonal to the cutting velocity, but inclined with helix (λ_s) or inclination (i) angle. Thus, an orthogonal to oblique transformation needs to be applied. The same concept has been implemented stated in Shamoto and Altintas [11], except the cutting coefficients are calculated in normal and friction directions instead of radial, tangential, and axial directions.

In orthogonal cutting, the rectangular shear plane area can be calculated as (Figure 5-3):

$$A_{s,orthogonal} = \frac{b\,h}{\sin\phi_c} \tag{5.4}$$

However, due to the helix angle (λ_s) in oblique cutting, the shear plane area is a parallelogram and its area can be calculated by:

$$A_{s,oblique} = \frac{b\,h}{\cos\lambda_s \sin\phi_n} \tag{5.5}$$

Where ϕ_n is the normal shear angle, i.e. shear angle measured in the normal plane P_n. In this study, using the same assumptions stated in Altintas [5], normal shear angle (ϕ_n) has been assumed equal to the shear angle in orthogonal cutting (ϕ_c).

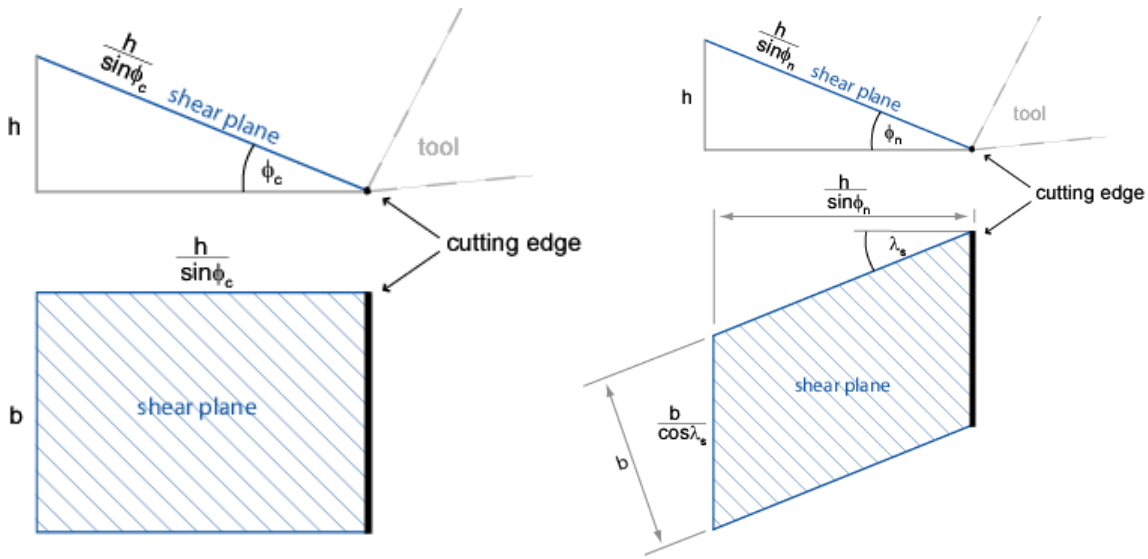

Figure 5-3: Shear Plane Area Comparison: Orthogonal Cutting (Left) and Oblique Cutting (Right).

In oblique cutting, shear force is equal to:

$$F_s = \tau_s A_s = \tau_s \frac{b\,h}{\cos\lambda_s \sin\phi_n} \tag{5.6}$$

Detailed illustration of the oblique cutting geometry is shown in Figure 5-4 [11]. When the shearing force is transformed to Cartesian coordinates, following equations can be obtained:

$$F_{X^{II}} = F_s \frac{\cos\phi_i \cos\theta_n}{\cos(\phi_n + \theta_n)} \tag{5.7}$$

$$F_{Y^{II}} = -F_s \sin\phi_i \tag{5.8}$$

$$F_{Z^{II}} = F_s \frac{\cos\phi_i \sin\theta_n}{\cos(\phi_n + \theta_n)} \tag{5.9}$$

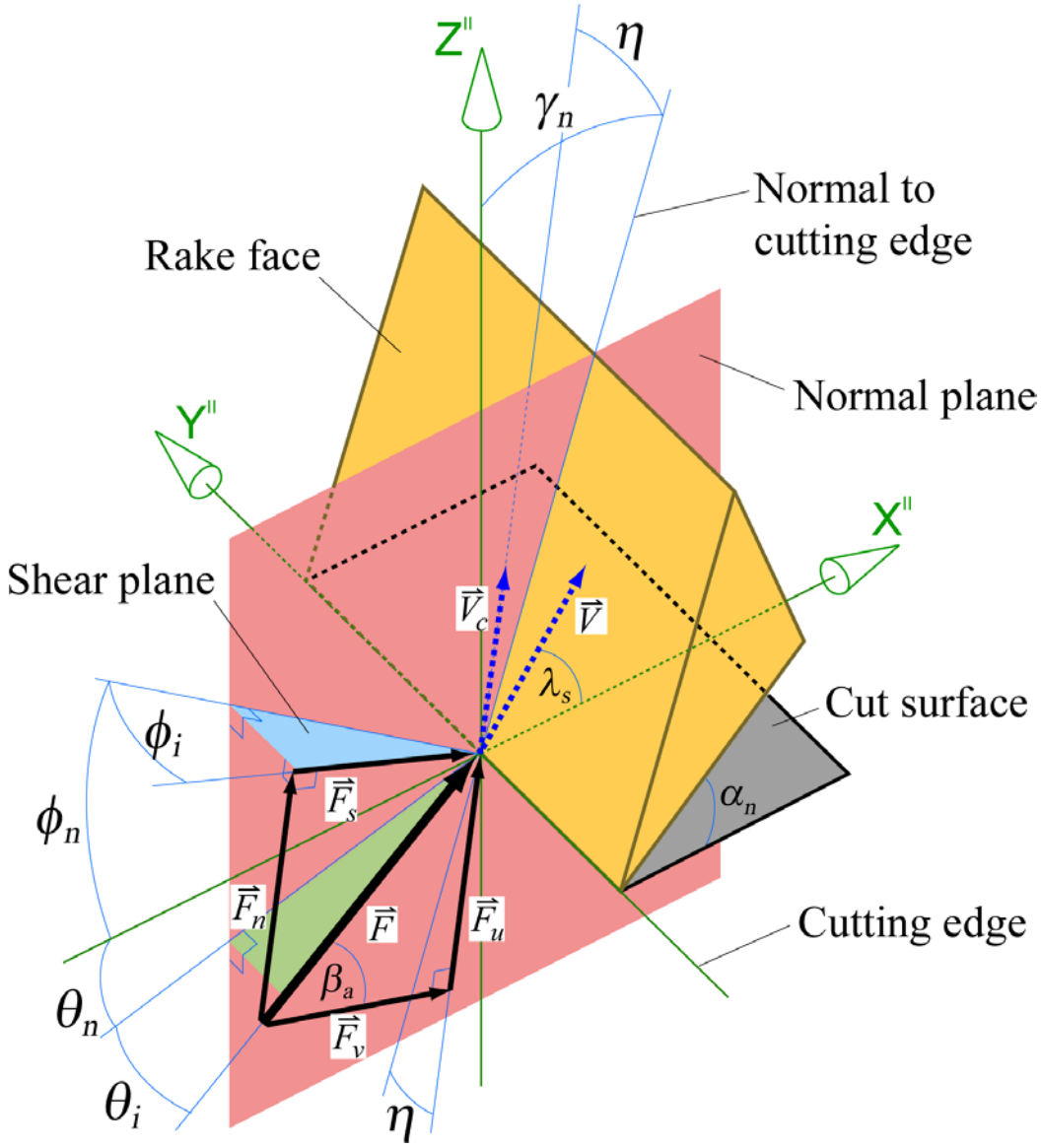

Figure 5-4: Cutting Forces, Velocities, and Angles in Oblique Cutting [11].

In order to use Eq. (5.7), Eq. (5.8), and Eq. (5.9), the unknown angles θ_n and ϕ_i must be expressed with known angles. θ_n is the angle between cut surface and the resultant cutting force F. Due to the simplified geometry in Figure 5-5:

$$\theta_n = \beta_n - \gamma_n \tag{5.10}$$

Similarly, the tangent of ϕ_i is equal to the following:

$$\tan\phi_i = \frac{F_y^{II}}{F_{sN}} \tag{5.11}$$

where F_{sN} is the projection of shear force F_s onto normal plane P_n.

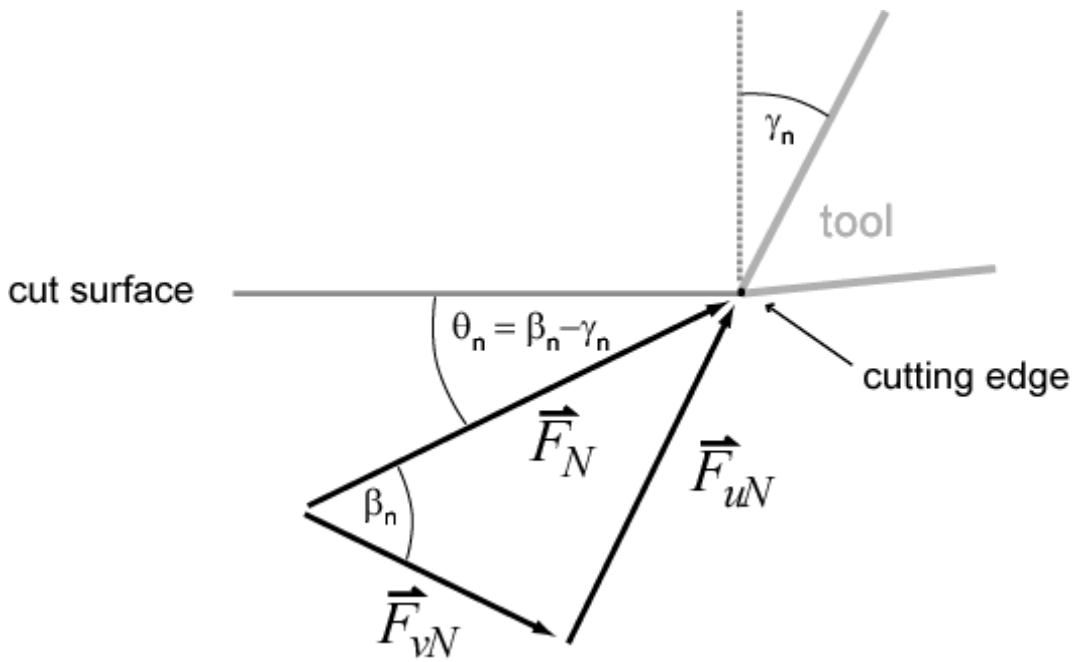

Figure 5-5: Illustration of angle θ_n. (F_N, F_{uN}, and F_{vN} Are Projections of Forces onto Normal Plane).

In Figure 5-4, F_N can be expressed as,

$$F_N = \frac{F_s\cos\phi_i}{\cos(\phi_n+\theta_n)} = \frac{F_u\cos\eta}{\sin\beta_n}$$
$$F_u = \frac{F_s\sin\phi_i}{\sin\eta} \tag{5.12}$$

Combining equations (5.10) and (5.12) gives the following relationship:

$$\tan\phi_i = \frac{\tan\eta\sin\beta_n}{\cos(\phi_n+\beta_n-\gamma_n)} \tag{5.13}$$

And furthermore:

$$\cos\phi_i = \frac{\cos(\phi_n + \beta_n - \gamma_n)}{\sqrt{\cos^2(\phi_n + \beta_n - \gamma_n) + \tan^2\eta\sin^2\beta_n}}$$
$$\sin\phi_i = \frac{\tan\eta\sin\beta_n}{\sqrt{\cos^2(\phi_n + \beta_n - \gamma_n) + \tan^2\eta\sin^2\beta_n}} \tag{5.14}$$

Combining equations (5.7), (5.8), (5.9), and (5.10) with (5.14) results in:

$$F_{X^{II}} = F_s \frac{\cos(\beta_n - \gamma_n)}{\sqrt{\cos^2(\phi_n + \beta_n - \gamma_n) + \tan^2\eta\sin^2\beta_n}}$$
$$= bh\left[\frac{\tau_s}{\cos\lambda_s\sin\phi_n}\frac{\cos(\beta_n - \gamma_n)}{\sqrt{\cos^2(\phi_n + \beta_n - \gamma_n) + \tan^2\eta\sin^2\beta_n}}\right]$$
$$F_{Z^{II}} = F_s \frac{\sin(\beta_n - \gamma_n)}{\sqrt{\cos^2(\phi_n + \beta_n - \gamma_n) + \tan^2\eta\sin^2\beta_n}}$$
$$= bh\left[\frac{\tau_s}{\cos\lambda_s\sin\phi_n}\frac{\sin(\beta_n - \gamma_n)}{\sqrt{\cos^2(\phi_n + \beta_n - \gamma_n) + \tan^2\eta\sin^2\beta_n}}\right] \tag{5.15}$$

Similarly, by substituting equations (5.6) and (5.16) into Equation (5.8):

$$F_{Y^{II}} = -F_s \frac{\tan\eta\sin\beta_n}{\sqrt{\cos^2(\phi_n + \beta_n - \gamma_n) + \tan^2\eta\sin^2\beta_n}}$$
$$= bh\left[-\frac{\tau_s}{\cos\lambda_s\sin\phi_n}\frac{\tan\eta\sin\beta_n}{\sqrt{\cos^2(\phi_n + \beta_n - \gamma_n) + \tan^2\eta\sin^2\beta_n}}\right] \tag{5.16}$$

Corresponding specific cutting coefficients in X^{II}, Y^{II}, and Z^{II} directions can be evaluated as:

$$K_{X^{II}} = \left[\frac{\tau_s}{\cos\lambda_s\sin\phi_n}\frac{\cos(\beta_n - \gamma_n)}{\sqrt{\cos^2(\phi_n + \beta_n - \gamma_n) + \tan^2\eta\sin^2\beta_n}}\right]$$
$$K_{Y^{II}} = \left[-\frac{\tau_s}{\cos\lambda_s\sin\phi_n}\frac{\tan\eta\sin\beta_n}{\sqrt{\cos^2(\phi_n + \beta_n - \gamma_n) + \tan^2\eta\sin^2\beta_n}}\right] \tag{5.17}$$
$$K_{Z^{II}} = \left[\frac{\tau_s}{\cos\lambda_s\sin\phi_n}\frac{\sin(\beta_n - \gamma_n)}{\sqrt{\cos^2(\phi_n + \beta_n - \gamma_n) + \tan^2\eta\sin^2\beta_n}}\right]$$

The cutting coefficients are transformed from the cutting edge coordinate system (System 2) to chip flow coordinate system (System 4) to calculate the cutting coefficients K_u and K_v. It is possible to accomplish this task in two different ways. Firstly, these coefficients in the cutting edge coordinate system can be geometrically transformed into the chip flow coordinate system as described in Chapter 4.3. The transformation matrix required for this task C_{42} can be obtained by:

$$C_{42} = (C_{23}\ C_{34})^T \tag{5.18}$$

Hence:

$$\begin{bmatrix} K_u \\ K_v \end{bmatrix} = C_{42} \begin{bmatrix} K_{X^{II}} \\ K_{Y^{II}} \\ K_{Z^{II}} \end{bmatrix}$$
$$\begin{bmatrix} K_u \\ K_v \end{bmatrix} = \begin{bmatrix} \sin\gamma_n \cos\eta & -\sin\eta & \cos\gamma_n \cos\eta \\ \cos\gamma_n & 0 & -\sin\gamma_n \end{bmatrix} \begin{bmatrix} K_{X^{II}} \\ K_{Y^{II}} \\ K_{Z^{II}} \end{bmatrix} \tag{5.19}$$

As a result:

$$K_u = \sin\gamma_n \cos\eta\ K_{X^{II}} - \sin\eta\ K_{Y^{II}} + \cos\gamma_n \cos\eta\ K_{Z^{II}}$$
$$K_v = \cos\gamma_n\ K_{X^{II}} - \sin\gamma_n\ K_{Z^{II}} \tag{5.20}$$

Alternatively, specific cutting coefficients in chip flow coordinate system can be calculated by evaluating the resultant force:

$$F = \sqrt{F_{X^{II}}^2 + F_{Y^{II}}^2 + F_{Z^{II}}^2} \tag{5.21}$$

By assuming that the average friction angle (β_a) is equal to the friction angle (β) in orthogonal cutting [5].

$$K_u = \frac{F}{bh} \sin\beta_a$$
$$K_v = \frac{F}{bh} \cos\beta_a \tag{5.22}$$

Figure 5-6 illustrates and summarizes the procedure outlined above. As result, specific cutting coefficients K_u and K_v on friction and normal directions can be evaluated with the following equations:

$$K_u = \frac{\tau_s\sqrt{1-\tan^2\eta\sin^2\beta_n}}{\cos\lambda_s\sin\phi_n\sqrt{\cos^2(\phi_n+\beta_n-\gamma_n)+\tan^2\eta\sin^2\beta_n}}\sin\beta_a$$
$$K_v = \frac{\tau_s\sqrt{1-\tan^2\eta\sin^2\beta_n}}{\cos\lambda_s\sin\phi_n\sqrt{\cos^2(\phi_n+\beta_n-\gamma_n)+\tan^2\eta\sin^2\beta_n}}cos\,\beta_a \tag{5.23}$$

Or applying the geometrical transformation in Equation (5.20):

$$K_u = \frac{\tau_s cos\eta(\sin\gamma_n\cos(\beta_n-\gamma_n)+\tan^2\eta\sin\beta_n+\cos\gamma_n\sin(\beta_n-\gamma_n))}{\cos\lambda_s\sin\phi_n\sqrt{\cos^2(\phi_n+\beta_n-\gamma_n)+\tan^2\eta\sin^2\beta_n}}$$
$$K_v = \frac{\tau_s\cos\gamma_n\cos(\beta_n-\gamma_n)\,(1-\tan\gamma_n\tan(\beta_n-\gamma_n))}{\cos\lambda_s\sin\phi_n\sqrt{\cos^2(\phi_n+\beta_n-\gamma_n)+\tan^2\eta\sin^2\beta_n}} \tag{5.24}$$

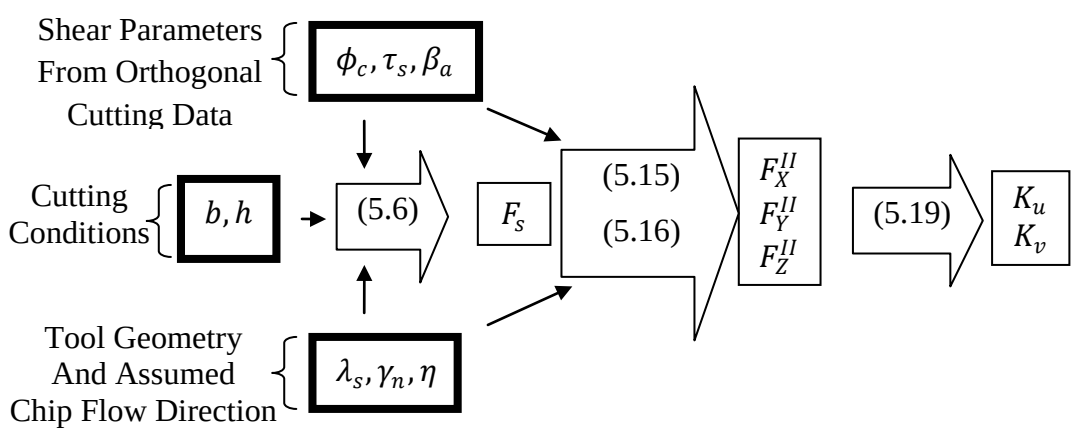

Figure 5-6: Summary of the Classical Approach in Cutting Coefficient Identification.

In summary, cutting coefficients in friction and normal directions can be evaluated using orthogonal shear parameters by Eq. (5.24). After obtaining the cutting coefficients, cutting force model explained in Section 5.2 can be applied. The edge coefficients K_{ue} and K_{ve} can be calculated by transforming the edge coefficients from RTA coordinate system to UV coordinate system. Alternatively, they can be added when the cutting forces are calculated and transformed back to the RTA coordinate system or machine coordinate system. In the simulations and validations shown in the following sections, second method has been used.

5.3.2 Mechanistic Identification

Currently, the most commonly used approach to determine the cutting coefficients is the mechanistic identification. Although this approach cannot provide the detailed microscopic effects of the machining process, such as shearing and chip flow, it allows predicting the cutting forces without extensive turning tests. However, in mechanistic modeling, accurate determination of these cutting coefficients over a wide range of cutting conditions is time consuming, since it requires a large number of experiments with many parameters such as cutting tool – workpiece material combination, cutting tool geometry, cutting speed, and depth of cut. In the following sections, two different cases to identify the cutting coefficients K_u and K_v are discussed.

Empirical Approach

In the first case, calculations that are needed to identify the cutting coefficients from experiments are presented. By using this method, it is also possible to calculate the true chip flow angle (η).

Since edge forces have no effect on shearing, they must be calculated and subtracted from total cutting forces in radial, tangential, and axial directions [5]. Thus, it is possible to reduce the cutting force equations as the following:

$$\begin{aligned} F_{rc} &= K_r\, A_c \\ F_{tc} &= K_t\, A_c \\ F_{ac} &= K_a\, A_c \end{aligned} \tag{5.25}$$

where F_{ic} is the cutting force in $i \in (r, t, a)$ direction, K_i is the specific cutting coefficient in i direction, and A_c is the chip load. In order to evaluate the coefficients in normal and friction directions, the transformation equations derived in Chapter 4.3 are applied.

$$\begin{aligned} K_r &= (K_u \cos\gamma_n \cos\eta - K_v \sin\gamma_n) \\ K_t &= (K_u \sin\lambda_s \sin\eta + K_u \cos\lambda_s \sin\gamma_n \cos\eta + K_v \cos\lambda_s \cos\gamma_n) \\ K_a &= (-K_u \cos\lambda_s \sin\eta + K_u \sin\lambda_s \sin\gamma_n \cos\eta + K_v \sin\lambda_s \cos\gamma_n) \end{aligned} \tag{5.26}$$

In Equation (5.26), K_r, K_t, and K_a can be obtained from cutting tests, normal rake (γ_n) and oblique / helix angle (λ_s) can be obtained from tool geometry, and K_u, K_v, and chip flow angle (η) are unknown. There are three equations and three unknowns, however, chip flow angle (η) is nonlinear. To overcome this problem, two new variables, K_{u1} and K_{u2} were introduced:

$$\begin{aligned} K_{u\,1} &= K_u \cos\eta \\ K_{u\,2} &= K_u \sin\eta \end{aligned} \tag{5.27}$$

Substituting Equation (5.27) into Equation (5.26):

$$\begin{aligned} K_r &= C_{ur\,1} K_{u\,1} + C_{vr} K_v \\ K_t &= C_{ut\,1} K_{u\,1} + C_{ut\,2} K_{u\,2} + C_{vt} K_v \\ K_a &= C_{ua\,1} K_{u\,1} + C_{ua\,2} K_{u\,2} + C_{va} K_v \end{aligned} \tag{5.28}$$

where

$$C_{ur\,1} = \cos\gamma_n\,, C_{vr} = -\sin\gamma_n\,, C_{ut\,1} = \cos\lambda_s \sin\gamma_n\,, C_{ut\,2} = \sin\,\lambda_s\,, C_{vt} = \cos\lambda_s \cos\gamma_n$$

$$C_{ua\,1} = \sin\lambda_s \sin\gamma_n\,, C_{ua\,2} = -\cos\lambda_s\,, C_{va} = \sin\lambda_s \cos\gamma_n$$

These coefficients are only functions of tool geometry, and they are constant for a specific experiment. As a result, there are 3 linear equations with three unknowns. In matrix form:

$$\begin{bmatrix} K_r \\ K_t \\ K_a \end{bmatrix} = \begin{bmatrix} C_{ur\,1} & 0 & C_{vr} \\ C_{ut\,1} & C_{ut\,2} & C_{vt} \\ C_{ua\,1} & C_{ua\,2} & C_{va} \end{bmatrix} \begin{bmatrix} K_{u\,1} \\ K_{u\,2} \\ K_v \end{bmatrix} \tag{5.29}$$

Solving these equations in Eq. (5.29) results in K_{u1}, K_{u2}, and K_v. It should be noted that:

$$K_u = \sqrt{K_{u\,1}^{\,2} + K_{u\,2}^{\,2}} \tag{5.30}$$

$$\eta = \tan^{-1}\frac{K_{u\,2}}{K_{u\,1}} \tag{5.31}$$

Consequently, a set of simple experiments with known cutting conditions and tool geometry are sufficient to calculate the cutting coefficients and chip flow angle. Since most of the chip flow models in the literature are based on empirical equations, and the

theoretical models are difficult to apply and generalize, this method provides a quick way to determine the chip flow angle.

During milling, chip thickness varies continuously as tool motion is a trochoidal motion. In order to apply proposed mechanistic identification method, cutting force coefficients can be obtained in terms of the average chip thickness defined as [45]:

$$\overline{A_c} = \frac{1}{\theta_{ex} - \theta_{st}} \int_{\theta_{st}}^{\theta_{ex}} A_c(\theta)\, d\theta \tag{5.32}$$

where θ_{st} and θ_{ex} are tool entry and exit angles, respectively.

Theoretical Approach

In the second case, it has been assumed that the cutting coefficients in radial, tangential, and axial directions as well as tool geometry are known, but the objective is to calculate the shear parameters (shear stress τ_s, shear angle ϕ_c, and friction angle β_a) only using this set of experiments. There have been two fundamental approaches for the solution of oblique cutting parameters, namely maximum shear stress principle and the minimum energy principle. Although these principles are iterative models, it is possible to obtain an approximate solution using Stabler's chip flow assumption ($\eta = \lambda_s$).

Maximum Shear Stress Principle

Maximum shear stress principle states that the resultant cutting force (F) makes an angle amount of ($\phi_c + \beta_a - \gamma_n$) with the shear plane, and the angle between the maximum shear stress and the principal stress is 45° [57]. So:

$$\begin{gathered} F_s = F(\cos\theta_i \cos(\theta_n + \phi_n) \cos\phi_i + \sin\theta_i \sin\phi_i) \\ F_s = F \cos 45° \end{gathered} \tag{5.33}$$

Moreover, another statement of this principle dictates that the projection of the resultant force to the shear plane coincides with the shear direction. This results in:

$$F(\cos\theta_i \cos(\theta_n + \phi_n) \sin\phi_i - \sin\theta_i \cos\phi_i) = 0 \tag{5.34}$$

Eq. (5.33) and Eq. (5.34) are used to derive the following relationships:

$$\phi_i = \sin^{-1}\left(\sqrt{2}\sin\theta_i\right) \tag{5.35}$$

$$\phi_n = \cos^{-1}\left(\frac{\tan\theta_i}{\tan\phi_i}\right) - \theta_n \tag{5.36}$$

Figure 5-4 illustrates the oblique cutting mechanics. In order to avoid dividing by zero for orthogonal cases, Eq. (5.36) can be rewritten as:

$$\phi_n = \cos^{-1}\left(\frac{1}{\sqrt{2}}\frac{\cos\phi_i}{\cos\theta_i}\right) - \theta_n \tag{5.37}$$

Using Eq. (5.35), Eq. (5.37), and the tool geometry (γ_n, λ_s), new chip flow angle (η_e) can be calculated using the velocity relation:

$$\eta_e = \tan^{-1}\left(\frac{\tan\lambda_s\cos(\phi_n - \gamma_n) - \cos\gamma_n\tan\phi_i}{\sin\phi_n}\right) \tag{5.38}$$

In order to calculate the true chip flow angle, following interpolation algorithm is applied by using new and previous chip flow angles:

$$\eta(k) = \upsilon\,\eta(k-1) + (1-\upsilon)\,\eta_e \tag{5.39}$$

Using the above equations, true chip flow angle can be calculated iteratively. In this equation, ν is the convergence parameter. When the iteration is completed, the shear stress can be calculated as the following:

$$F = \sqrt{F_u^2 + F_v^2} = bh\sqrt{K_u^2 + K_v^2} \tag{5.40}$$

$$F_s = \tau_s A_s = \tau_s\left(\frac{b}{\cos\lambda_s}\right)\left(\frac{h}{\sin\phi_n}\right) = F\cos 45° \tag{5.41}$$

$$\tau_s = \sqrt{\frac{K_u^2 + K_v^2}{2}}\cos\lambda_s\sin\phi_n \tag{5.42}$$

Results and discussions about this approach are given in the following sections.

Minimum Energy Principle

In this approach work done by Shamoto and Altintas [11] is used. In their study, resultant cutting force is expressed as:

$$F = \frac{\tau_s bh}{[\cos(\theta_n + \phi_n)\cos\theta_i \cos\phi_i + \sin\theta_i \sin\phi_i]\cos\lambda_s \sin\phi_n} \tag{5.43}$$

And the cutting power (P_t) required during cutting can be expressed as:

$$P_t = F(\cos\theta_i \cos\theta_n \cos\lambda_s + \sin\theta_i \sin\lambda_s)\, V \tag{5.44}$$

where V is the cutting speed. Non-dimensional cutting power ($P_t^{'}$) can be derived by substituting Eq. (5.43) into Eq. (5.44).

$$P_t^{'} = \frac{P_t}{V\tau_s bh} = \frac{\cos\theta_n \tan\theta_i \tan\lambda_s}{[\cos(\theta_n + \phi_n)\cos\phi_i + \tan\theta_i \sin\phi_i]\sin\phi_n} \tag{5.45}$$

Minimum energy principle states that the cutting power drawn must be minimal for a unique shear angle solution [11]. Therefore:

$$\begin{aligned} \frac{\partial P_t^{'}}{\partial \phi_n} &= 0 \\ \frac{\partial P_t^{'}}{\partial \phi_i} &= 0 \end{aligned} \tag{5.46}$$

Using Stabler's chip flow angle rule and maximum shear stress equations for the initial guess, shear angles (ϕ_n and ϕ_i) are iterated to minimize the non-dimensional cutting power $P_t^{'}$ using the following iterative equations:

$$\begin{Bmatrix} \phi_n(k) \\ \phi_i(k) \end{Bmatrix} = \begin{Bmatrix} \phi_n(k-1) \\ \phi_i(k-1) \end{Bmatrix} - \zeta \begin{Bmatrix} \Delta P_t^{'}/\Delta\phi_n \\ \Delta P_t^{'}/\Delta\phi_i \end{Bmatrix} \tag{5.47}$$

In this method, convergence depends on the step size ζ and the marginal increase during the perturbation ($\Delta\phi_{n,i}$). After the iterations are completed, shear stress can be calculated by the following equations:

$$\begin{aligned} F_s &= F[\cos(\theta_n + \phi_n)\cos\phi_i \cos\theta_i + \sin\theta_i \sin\phi_i] \\ \tau_s &= \sqrt{K_u^2 + K_v^2}\,[\cos(\theta_n + \phi_n)\cos\phi_i \cos\theta_i + \sin\theta_i \sin\phi_i]\cos\lambda_s \sin\phi_n \end{aligned} \tag{5.48}$$

Enhancement of the Theoretical Models

Stabler's rule of chip flow is used as the initial guess in most theoretical models. However, since it is possible to obtain true chip flow angle using maximum shear stress and minimum energy principles, an iterative method was adapted to improve the calculation of chip flow angle and cutting coefficients. Block diagram of this enhancement is illustrated in Figure 5-7. Stabler's rule ($\eta = \lambda_s$) was used as the initial value and cutting coefficients in UV coordinate system were calculated by using geometrical transformations. Then using the minimum energy or maximum shear stress principle, new chip flow angle was calculated and the procedure was repeated until the difference between the new and previous chip flow angle is less than the specified tolerance value.

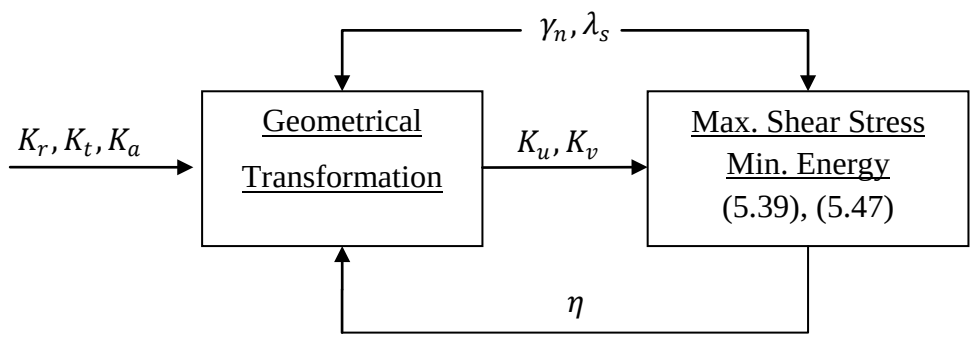

Figure 5-7: Block Diagram of the Iterative Method to Enhance the Theoretical Models.

By using the proposed method, it is possible to determine the inclination angle λ_s of the tool used to obtain the mechanistically determined cutting, K_r, K_t, and K_a. In order to accomplish this task, following procedure was applied:

1. Cutting coefficients in radial, tangential, and axial directions were transformed to friction and normal coefficients K_u and K_v using the geometrical transformation equations described in Chapter 4.3. In order to complete the transformations, an arbitrary value for λ_s was selected. Since λ_s is unknown, this procedure must be repeated for each value of λ_s in a predetermined range.

2. Using the minimum energy principle, shear parameters (τ_s, ϕ_n, and β_a) as well as true chip flow angle η were calculated.

3. Following that, K_r, K_t, and K_a were calculated back using the orthogonal to oblique transformation using the following equations [5]:

$$K_r = \frac{\tau_s}{\sin\phi_n \cos\lambda_s} \frac{\sin(\beta_n - \gamma_n)}{\sqrt{\cos^2(\phi_n + \beta_n - \gamma_n) + \tan^2\eta \sin^2\beta_n}}$$
$$K_t = \frac{\tau_s}{\sin\phi_n} \frac{\cos(\beta_n - \gamma_n) + \tan\lambda_s \tan\eta \sin\beta_n}{\sqrt{\cos^2(\phi_n + \beta_n - \gamma_n) + \tan^2\eta \sin^2\beta_n}} \tag{5.49}$$
$$K_a = \frac{\tau_s}{\sin\phi_n} \frac{\cos(\beta_n - \gamma_n)\tan\lambda_s - \tan\eta \sin\beta_n}{\sqrt{\cos^2(\phi_n + \beta_n - \gamma_n) + \tan^2\eta \sin^2\beta_n}}$$

4. Calculated and original values of the cutting coefficients were compared and the errors for each λ_s were calculated using Eq. (5.50).

$$\%\, Error = \frac{\left|K_{calculated} - K_{original}\right|}{K_{original}} \times 100 \tag{5.50}$$

It can be observed that for a unique oblique angle, percentage error for axial cutting coefficient K_a is minimal.

Mechanistically determined cutting coefficients for two different workpiece materials are used as inputs. Although the tool geometry (rake and helix angles) was known, helix angle (λ_s) has been assumed to be unknown to check the validity of the proposed method.

The first analysis was made on Ti6Al4V workpiece. Results of Budak's cutting coefficient identification [58] were used. Tool used for the mechanistic calibration has 15° rake angle ($\gamma_n = 15°$) and 30° helix angle ($\lambda_s = 30°$). In order to apply the model, helix angle is assumed to be unknown and all angles between 0° and 40° were scanned in the analysis and errors were calculated using the procedure outlined above. Table 5-I presents the cutting coefficients and tool workpiece used in both cases.

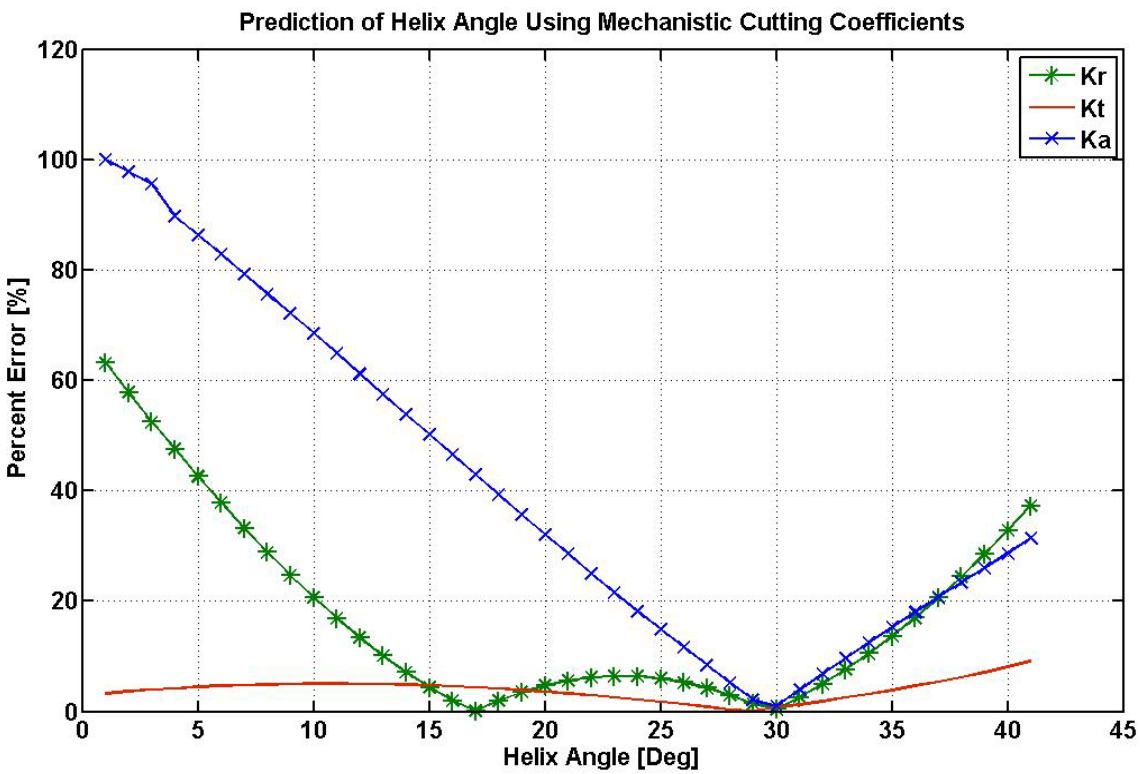

Figure 5-8: Results of Helix Angle Predictions for Ti6Al4V.

Table 5-I: Cutting Coefficients and Tool Geometry Used in the Analysis.

Material	K_r [MPa]	K_t [MPa]	K_a [MPa]	Helix λ_s [°]	Rake γ_n [°]
Ti6Al4V	340	1630	608	30	15
Al7075	788.83	1319.41	48.751	5	0

Second analysis was performed using the coefficients calculated in Engin's study [44]. Workpiece material has been Al7075, and the tool used in mechanistic identification has been a bull-nose end mill with 5/4" diameter, 0° rake angle, and 5° helix angle. Cutting coefficients are listed in Table 5-I and error results are presented in Figure 5-9.

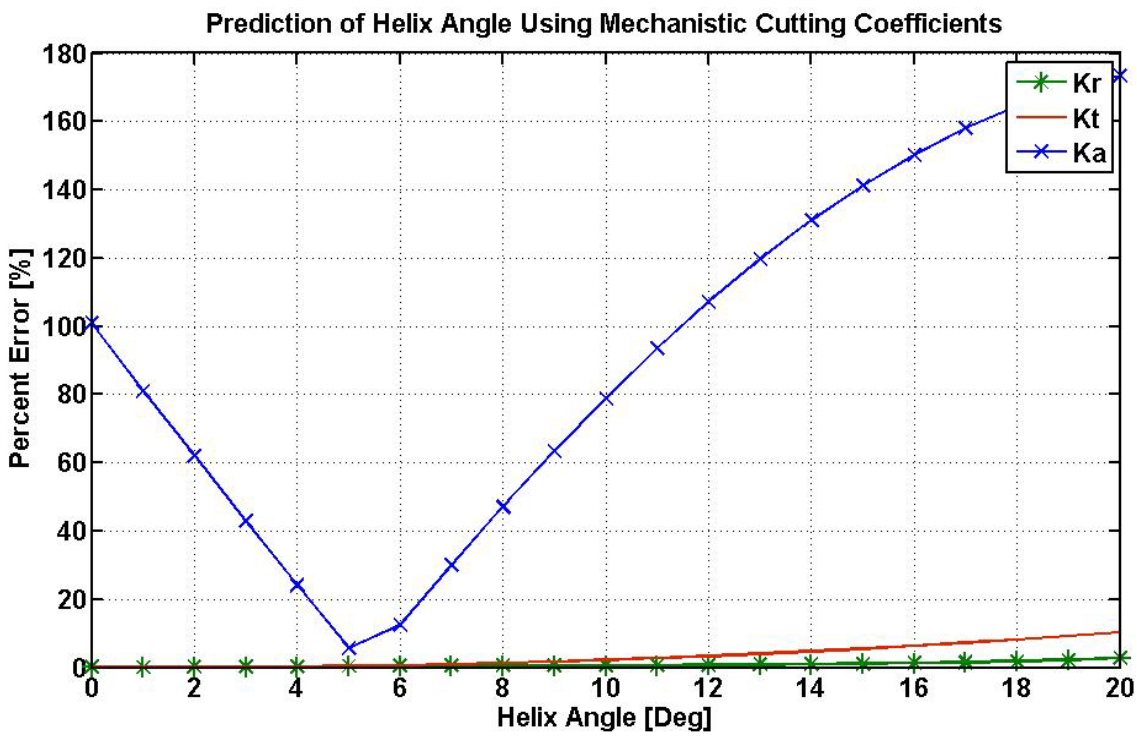

Figure 5-9: Results of Helix Angle Predictions for Al7075.

It can be observed from Figure 5-8 and Figure 5-9 that K_a is very sensitive to the changes in the helix angle and it is possible to accurately determine the helix angle by applying the proposed method.

On the other hand, theoretical proof of this method is rather difficult, because chip flow angle also depends on the helix angle and the equations used in minimum energy principle is rather complex and they can be solved only using numerical methods.

Results and Summary

Block diagram of the procedures explained in this section is illustrated in Figure 5-10. As a case study, to validate the models discussed in this section, mechanistically determined average cutting coefficients in RTA coordinate system were transformed to UV coordinate system and shear parameters were calculated using both maximum shear stress principle and minimum energy principle. Table 5-II summarizes the results:

Table 5-II: Comparison of the Methods for the Solution of Oblique Shear Parameters.

Maximum Shear Stress Principle								
Cutting Tool	Rake Angle γ_n [°]	Oblique Angle λ_s [°]	Friction Angle β_a [°]	Shear Angle ϕ_n [°]	Shear Stress τ_s[MPa]	Chip Flow Angle η [°]	Comp. Time [ms]	# of Iterations
CTGP	5	0	26.9	23	508	0	6.6 ms	2
SCGP	3.5	3.5	32	16.5	459.2	3.3	6.4 ms	31
MTGN	-5	-5	20.3	17.1	477.8	-5.4	7.4 ms	14
Orthogonal	5	0	28.1	31.2	549	0	-	-
Minimum Energy Principle								
Cutting Tool	Rake Angle γ_n [°]	Oblique Angle λ_s [°]	Friction Angle β_a [°]	Shear Angle ϕ_n [°]	Shear Stress τ_s[MPa]	Chip Flow Angle η [°]	Comp. Time [ms]	# of Iterations
CTGP	5	0	26.9	33.1	573.8	0	13.2	140
SCGP	3.5	3.5	32	30.1	596	1.72	14.5	115
MTGN	-5	-5	20.3	31.6	600	-3.1	14.4	124
Orthogonal	5	0	28.1	31.2	549	0	-	-

Workpiece used in these experiments was AISI Steel 1045, and Kennametal tools were used. Cutting speed (V) was 150 m/min and the width of cut (b) was 3.05 mm. Highlighted row is the experimentally measured orthogonal reference data. From Table 5-II, it can be observed that the minimum energy principle gives more accurate results than the maximum shear stress principle, since maximum shear stress principle is more conservative approach. However, minimum energy principle needs more iteration to calculate the shear parameters than the maximum shear stress principle.

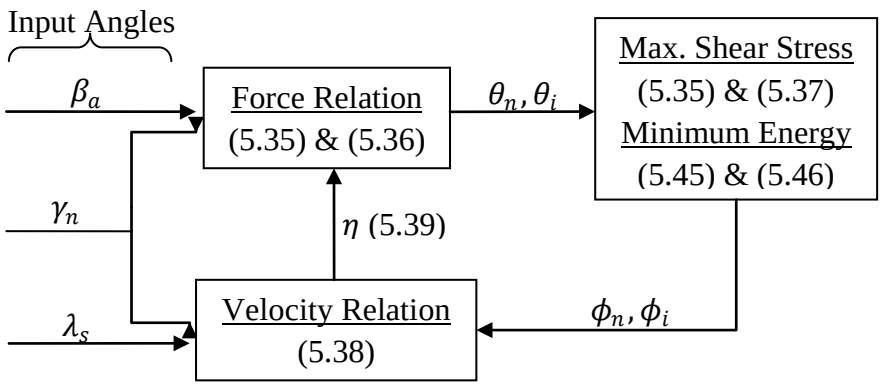

Figure 5-10: Theoretical Identification Procedure.

In mechanistic modeling, it is possible to determine the cutting coefficients by using a single test. Therefore, it provides an opportunity to observe the effect of chip thickness on the cutting coefficients. On the other hand, theoretical methods use average cutting coefficients, in which one set of coefficients can be obtained by conducting tests with different chip thicknesses. Figure 5-11 demonstrates this argument with SCGP tool. Tool geometry and cutting conditions are listed above. In Figure 5-11, it can be observed that specific cutting coefficients increase exponentially as the chip thickness decreases. This phenomenon is called size effect.

Figure 5-12 shows the comparison of chip flow angle of different methods. Stabler rule states that the chip flow angle is equal to the inclination angle λ_s. It can be seen that according to the mechanistic approach, there is also an exponential relationship between chip thickness and chip flow angle, similar to the size effect.

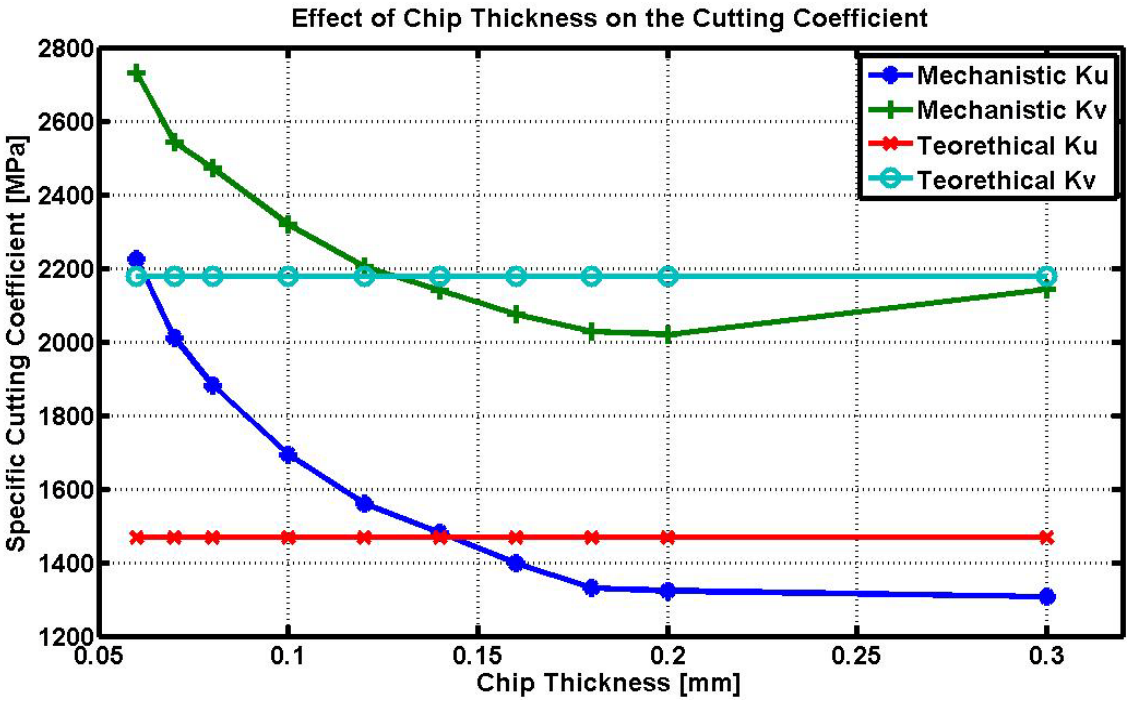

Figure 5-11: Effect of Chip Thickness on the Cutting Coefficients.

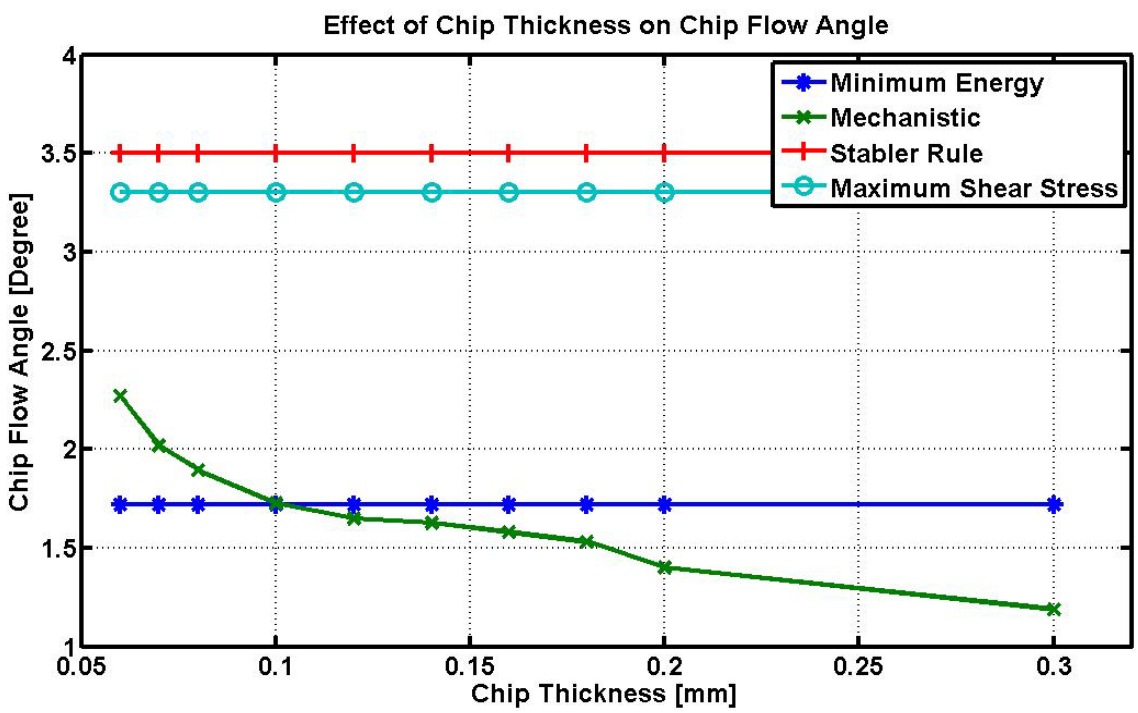

Figure 5-12: Effect of Chip Thickness on the Chip Flow Angle.

5.4 Cutting Force Simulations and Validations

Proposed insert geometry and mechanics models discussed in previous chapter are combined to simulate cutting forces in turning and milling using different tools. Several different insert geometries are considered for each type of cutting process.

5.4.1 Turning Process Simulations

To validate the model in turning, two different cases are selected. First case is orthogonal cutting with a triangular insert, and the second case is oblique cutting with a square insert.

Experimental Setup

Validation experiments for turning process have been performed on Hardinge Superslant lathe. The workpiece material was AISI Steel 1045 bar with 255HB hardness. The diameter of the workpiece was 38.1 mm. Kistler three component dynamometer (Model 9121) and charge amplifier were used to measure the cutting forces. The dynamometer was mounted on the turret as shown in Figure 5-13.

Displaying and recording of the measured data were performed with data acquisition software, MalDAQ module of CutPro 8.0. Figure 5-14 shows a sample output screen of MalDAQ.

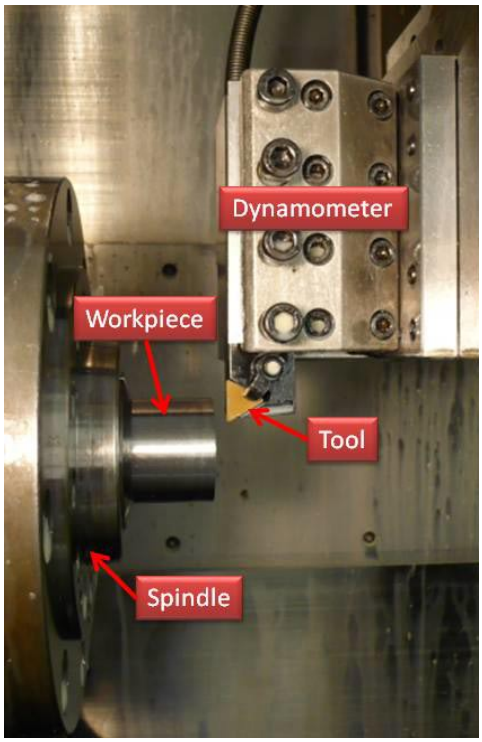

Figure 5-13: Workpiece and 3- Component Dynamometer Fixed to Turret for Cutting Tests.

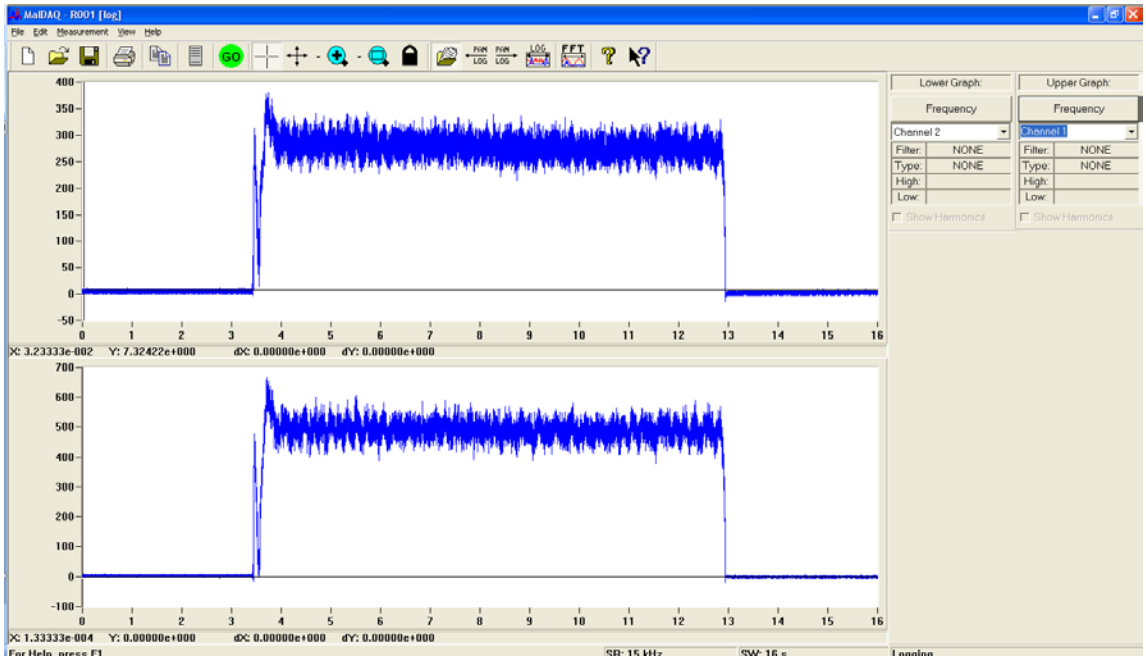

Figure 5-14: Sample Output Screen in CutPro 8.0 for Cutting Forces.

Orthogonal Cutting Tests

A carbide triangular insert (TPG322) from Kennametal and a shank style tool holder (CTGP) with 5° normal rake angle (γ_n), 75° cutting edge angle (κ_r) and 0° inclination angle (λ_s) was used in orthogonal cutting tests. The influence of nose radius was avoided by using a tube with a wall thickness of 3.05 mm. Orthogonal cutting parameters were used to calculate cutting coefficients in friction and normal directions at each selected point on the cutting edge. The tests were performed at different cutting speeds and feed rates. Cutting conditions for orthogonal cutting validation experiments are summarized in Table 5-III. As the cutting speed changes along the cutting edge, cutting coefficients become different at each differential disk on the tool. Therefore, at each differential disk, cutting coefficients K_u and K_v are calculated by using the following equations:

$$\begin{aligned} \phi_n &= e^{(0.6123\ h - 0.6988)} \\ \beta_a &= e^{(-0.1515\ h - 0.5453)} \\ \tau_s &= e^{0.0417\ h - 0.0079\ V + 6.2938} \end{aligned} \tag{5.51}$$

The model is validated by comparing the predicted forces against new experimental results as shown in Simulated and experimental forces are plotted versus chip thickness in Figure 5-15 and Figure 5-16.

Table 5-III: Orthogonal Turning Validation Experiments Cutting Conditions.

Tool Geometry			
$\boldsymbol{L}$ (Insert Length)	12 mm	$\boldsymbol{\kappa_r}$ (Cutting Edge Angle)	75°
$\boldsymbol{iW}$ (Insert Width)	-	$\boldsymbol{\gamma_f}$ (Radial Rake Angle)	0°
$\boldsymbol{b_s}$ (Wiper Edge Length)	-	$\boldsymbol{\gamma_p}$ (Axial Rake Angle)	0°
$\boldsymbol{r_\varepsilon}$ (Corner Radius)	-	$\boldsymbol{\varepsilon_r}$ (Tool Included Angle)	60°
Cutting Conditions			
Width Of Cut	3.05 mm		
Feed Rate	0.1 – 0.3 mm/rev		
Cutting Speed	100 – 150 m/min		
Workpiece Material	AISI 1045 Steel		

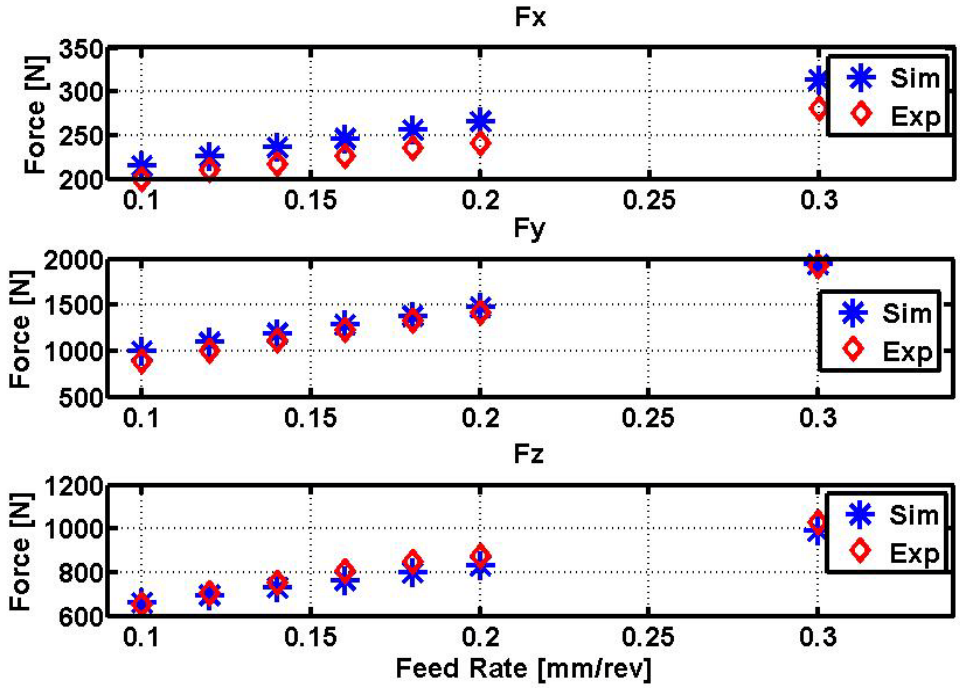

Figure 5-15: Forces simulated and measured for an orthogonal tool with 75° cutting edge angle for V=100 m/min.

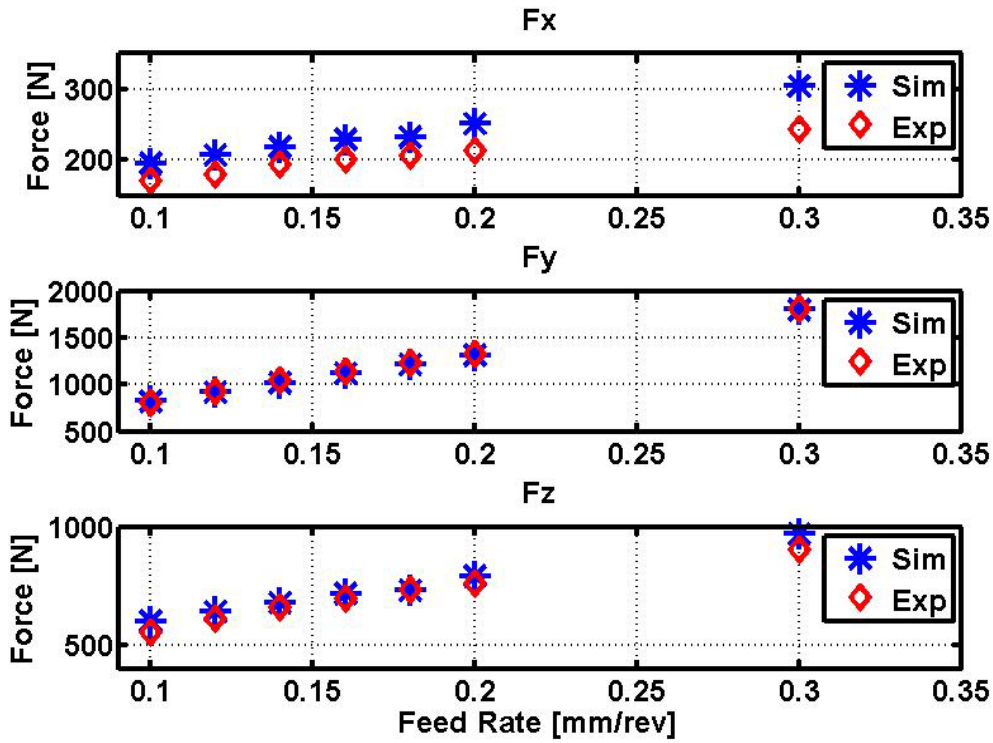

Figure 5-16: Forces simulated and measured for an orthogonal tool with 75° cutting edge angle for V=150 m/min.

Oblique Cutting Tests

After obtaining satisfactory validation results in orthogonal cutting validation tests, mechanics model has been tested for oblique tools with nose radius. Several tests were performed with different tools and the results are presented in the following sections.

Rhombic (ISO Style C) Insert: A rhombic insert with a tool included angle of 80° with -8° rake angle and -8° inclination angle was simulated and tested. The tool holder was Sandvik DCKNL 2020K 12, and the insert was Sandvik CNMA 12 04 08 rhombic insert with 0.8 mm nose radius. Insert geometry and cutting conditions are listed in Table 5-IV.

Table 5-IV: Tool Geometry and Cutting Conditions for Rhombic Insert.

Tool Geometry			
$\boldsymbol{L}$ (Insert Length)	12 mm	$\boldsymbol{\kappa_r}$ (Cutting Edge Angle)	75°
$\boldsymbol{iW}$ (Insert Width)	-	$\boldsymbol{\gamma_f}$ (Radial Rake Angle)	-8°
$\boldsymbol{b_s}$ (Wiper Edge Length)	-	$\boldsymbol{\gamma_p}$ (Axial Rake Angle)	-8°
$\boldsymbol{r_\varepsilon}$ (Corner Radius)	0.8 mm	$\boldsymbol{\varepsilon_r}$ (Tool Included Angle)	80°
Cutting Conditions			
Width Of Cut	2 – 4 mm		
Feed Rate	0.1 – 0.24 mm/rev		
Cutting Speed	150 m/min		
Workpiece Material	AISI 1045 Steel		

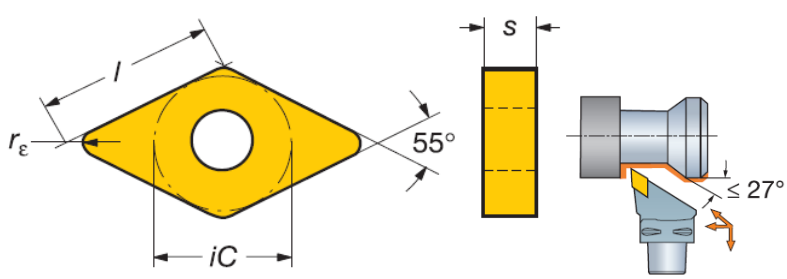

Figure 5-17: Illustration of Insert and the Holder Body [55].

The equations for the control points of this type of insert are given in Section 4.5.3. Hence, the locations of the geometric control points are (Figure 5-18):

Global coordinate system origin (Point A):

$$A_x = 0, \quad A_z = 0 \tag{5.52}$$

Insert center (Point I):

$$I_x = -3.359\,, \quad I_z = 8.076 \tag{5.53}$$

Insert cutting reference point (Point CRP):

$$CRP_x = 0.613\,, \quad CRP_z = 0 \tag{5.54}$$

Control Points (Points A, B, and D):

$$\begin{gathered} A_x = 0, \quad A_z = 0 \\ B_x = 0.772, \quad B_z = 0.592 \\ D_x = 3.651, \quad D_z = 11.336 \end{gathered} \tag{5.55}$$

Using the orientation angles ($\kappa_r = 75°, \gamma_f = \gamma_p = -8°$), control points are transformed and described in the global coordinate system by implementing the procedure presented in Section 4.3. After the transformations, the locations of the control points become:

$$\begin{gathered} A_x = 0, \quad A_y = 0, \;\; A_z = 0 \\ B_x = 0.753, \;\; B_y = -0.189, \;\; B_z = 0.587 \\ D_x = 3.396, \;\; D_y = -2.070, \;\; D_z = 11.226 \end{gathered} \tag{5.56}$$

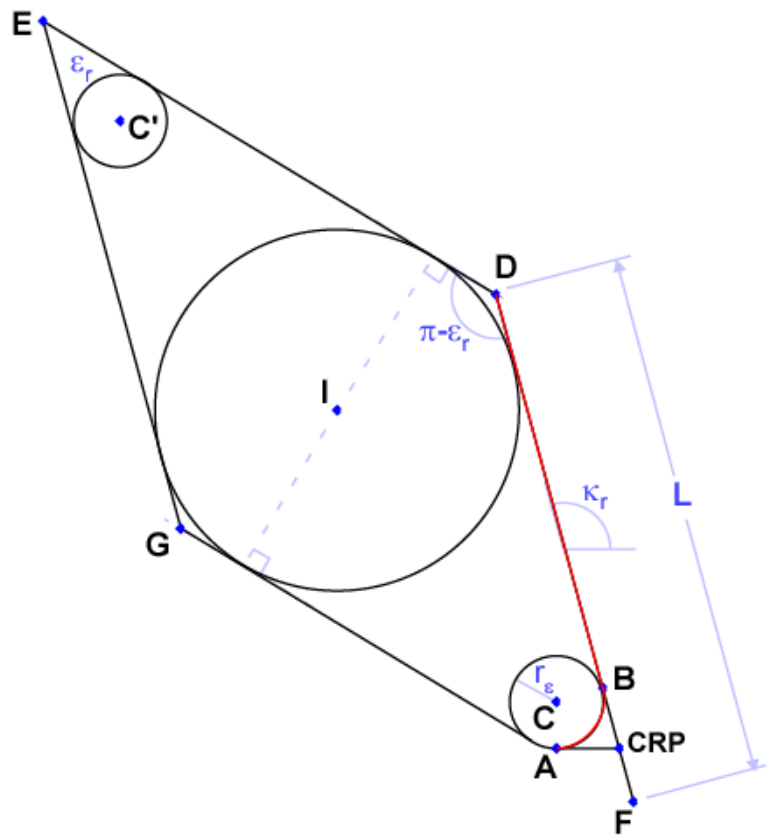

Figure 5-18: Geometric Control Points of a Rhombic Turning Insert.

For the arc between points A and B, following parametric arc equation is employed:

$$P_{AB} = R\cos t\,\vec{u} + R\sin t\;\vec{n}\times\vec{u} + C,\;\; 0 \le t \le \frac{\pi}{2}$$

$$R = 0.8, \qquad \vec{u} = \begin{bmatrix} 0.019 \\ 0.138 \\ -0.99 \end{bmatrix},\;\; \vec{n} = \begin{bmatrix} -0.138 \\ -0.980 \\ -0.139 \end{bmatrix},\;\; C = \begin{bmatrix} -0.015 \\ -0.110 \\ 0.792 \end{bmatrix} \tag{5.57}$$

$$P_{AB} = \begin{bmatrix} 0.015\cos t + 0.792\sin t - 0.015 \\ 0.110\cos t - 0.111\sin t - 0.110 \\ 0.792 - 0.792\cos t \end{bmatrix}$$

For the linear edge between points B and D, linear parametric equation was used:

$$P_{BD} = \vec{P}_B + \left(\vec{P}_D - \vec{P}_B\right) t \quad , \quad 0 \leq t \leq 1$$

$$\vec{P}_B = \begin{bmatrix} 0.753 \\ -0.189 \\ 0.587 \end{bmatrix}, \quad \vec{P}_D = \begin{bmatrix} 3.396 \\ -2.070 \\ 11.226 \end{bmatrix} \tag{5.58}$$

$$P_{BD} = \begin{bmatrix} 2.642\, t + 0.753 \\ -1.881\, t - 0.189 \\ 10.639\, t + 0.587 \end{bmatrix}$$

By changing the parameter t from 0 to 1 for each equation, the location of any point on the cutting edge can be calculated. Moreover, using the equations presented in Section 4.4, physical angles along the cutting edge were calculated. Finally, orthogonal parameters shown in (5.51) were used to calculate cutting coefficients K_u and K_v. Cutting forces were calculated using the rake face based force model which is described in Section 5.2. Simulated and experimental cutting forces for rhombic insert are shown in Figure 5-19 and Figure 5-20. The simulated forces showed good agreement with the experimental forces.

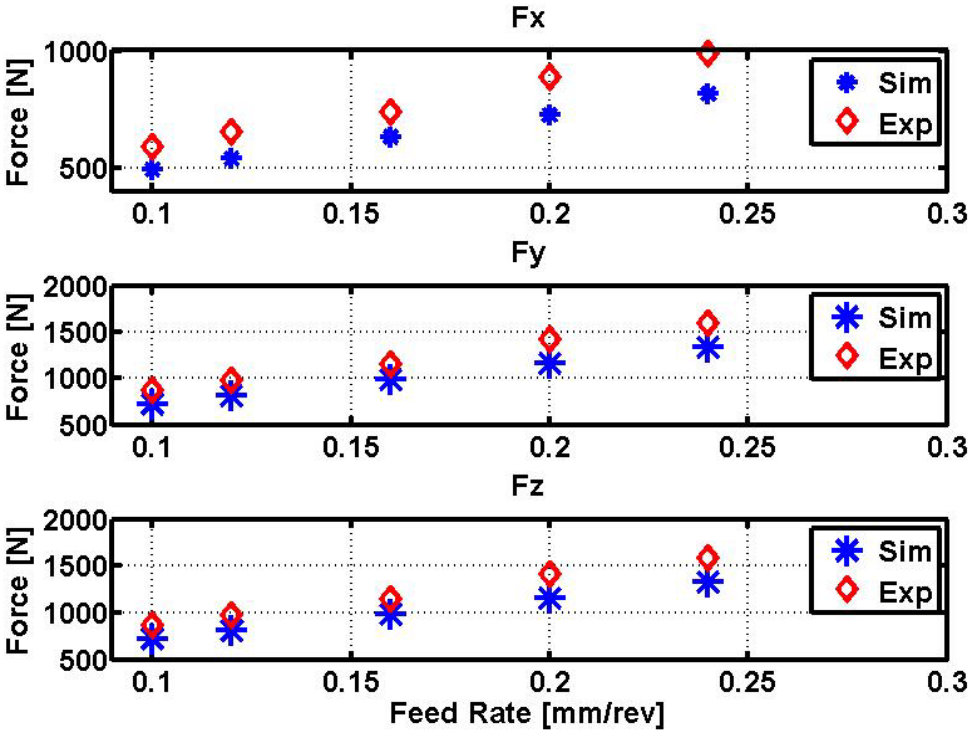

Figure 5-19: Comparison of Measured and Calculated Forces for the Rhombic Tool while the Width of Cut is 2 mm.

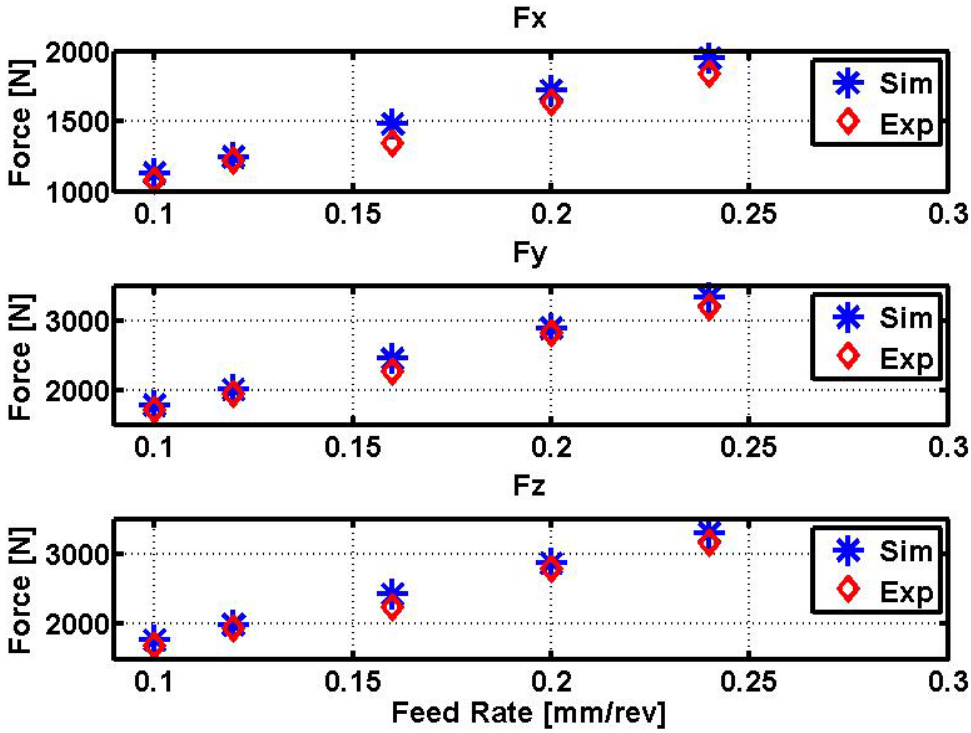

Figure 5-20: Comparison of Measured and Calculated Forces for the Rhombic Tool while the Width of Cut is 4 mm.

Square (ISO Style S) Insert: Next tool used to validate the cutting force model in turning was a Sandvik DSBNL 2020K 12 holder with 75° cutting edge angle, -6° rake and inclination angle and Sandvik SNMA 12 04 08 insert with 0.8 mm corner radius. Geometry inputs and experiment conditions are listed in Table 5-V. Tool geometry is illustrated in Figure 5-21. Similar to rhombic insert 2 sets of experiments were conducted with 2 mm and 4 mm widths of cut.

Using the same procedure described in the previous example, position of each selected point is calculated with the associated physical angles. Orthogonal cutting parameters shown in Eq. (5.51) and same cutting force model used to simulate the cutting forces. Although the validations are not as accurate as orthogonal cutting, results are satisfactory. The main reason behind the error is that cutting coefficients were determined using a positive rake tool, however the tools used in oblique cutting have negative rake angles. Following figures can be seen to compare the simulations and measured forces.

Table 5-V: Tool Geometry and Cutting Conditions for Square Insert.

Tool Geometry			
$\boldsymbol{L}$ (Insert Length)	12 mm	$\boldsymbol{\kappa_r}$ (Cutting Edge Angle)	75°
$\boldsymbol{iW}$ (Insert Width)	-	$\boldsymbol{\gamma_f}$ (Radial Rake Angle)	-6°
$\boldsymbol{b_s}$ (Wiper Edge Length)	-	$\boldsymbol{\gamma_p}$ (Axial Rake Angle)	-6°
$\boldsymbol{r_\varepsilon}$ (Corner Radius)	0.8 mm	$\boldsymbol{\varepsilon_r}$ (Tool Included Angle)	90°
Cutting Conditions			
Width Of Cut	2 – 4 mm		
Feed Rate	0.12 – 0.24 mm/rev		
Cutting Speed	150 m/min		
Workpiece Material	AISI 1045 Steel		

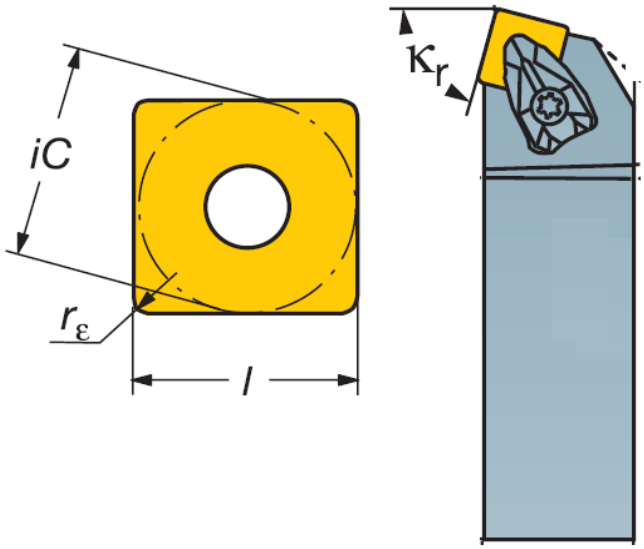

Figure 5-21: Illustration of Insert and the Holder Body [55].

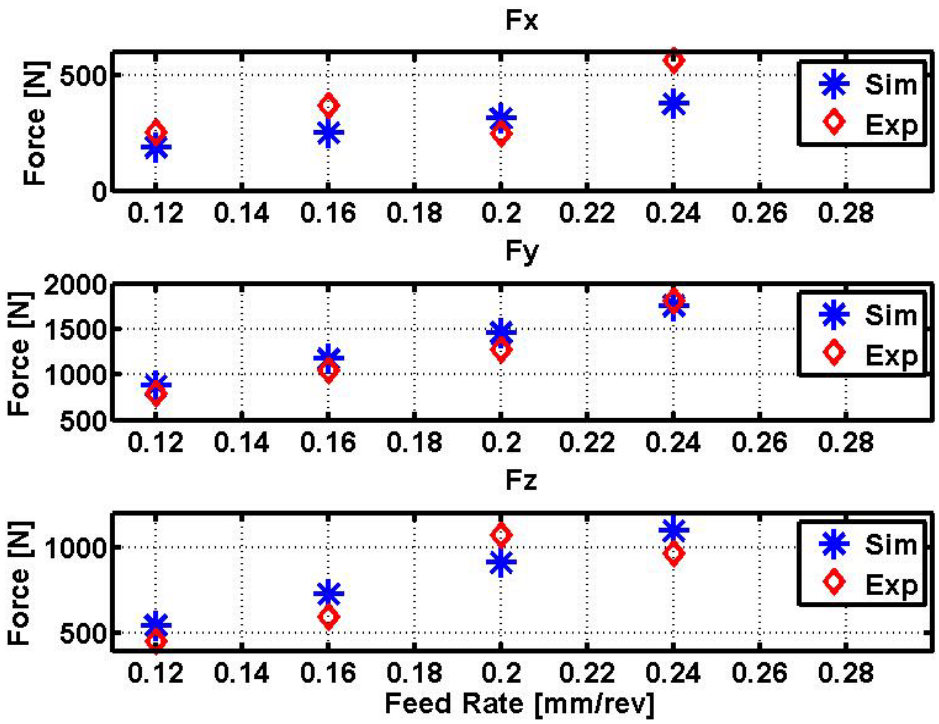

Figure 5-22: Comparison of Measured and Calculated Forces for the Square Insert while the Width of Cut is 2 mm.

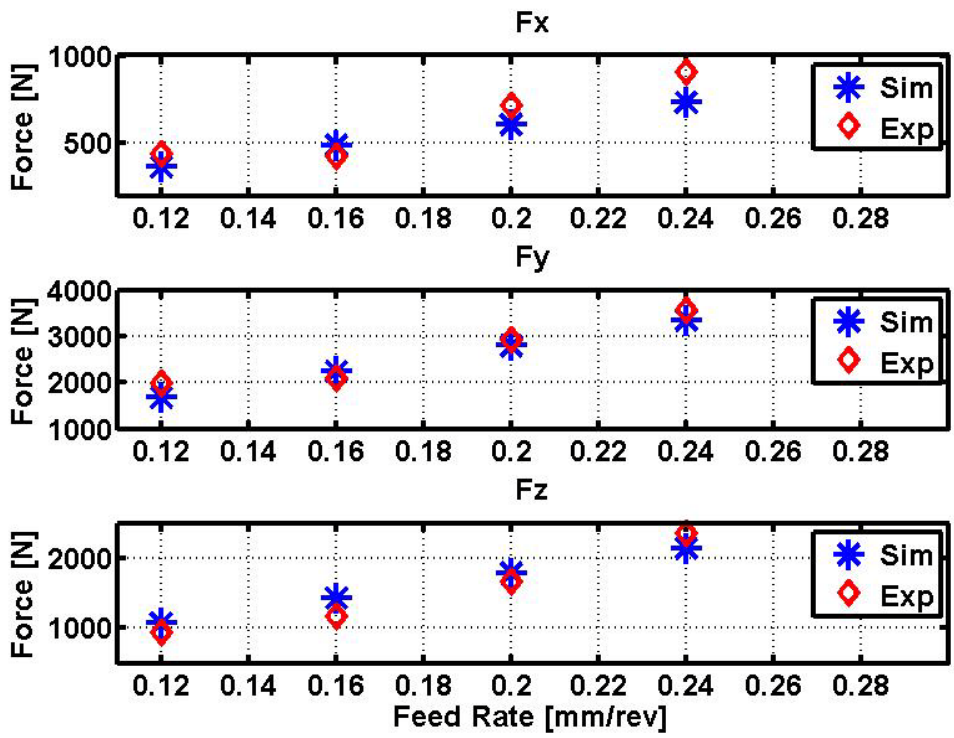

Figure 5-23: Comparison of Measured and Calculated Forces for the Square Insert while the Width of Cut is 4 mm.

5.4.2 Milling Process Simulations

Experimental Setup

The experiments for milling force validations have been performed on Mori Seiki NMV5000DCG 5 – axis machining center with 20000 rpm spindle. Various inserted milling tools were used from Sandvik Coromant. The workpiece material was aluminum blocks (Al7050-T451) with dimensions of 160x100x100 mm. Kistler three component dynamometer (Model 9257B) and a charge amplifier was used to measure the cutting forces. The dynamometer was mounted on the machine table using fixtures and the aluminum block was attached to the dynamometer as seen in Figure 5-24.

Similarly, displaying and recording the measured data was performed with data acquisition software MalDAQ module of CutPro 9.0. The complete actual testing environment is illustrated in Figure 5-25.

Various tests were performed for validation of the proposed force model. Differential cutting edge disk height and the differential rotation angle in simulations were selected to be 0.01 mm and 4° respectively which adequately resembled the actual cutting conditions for the mathematical cutting force model. The applied conditions and the results of the performed milling tests are described throughout this section.

The cutting coefficients were described as functions of rake angle, cutting speed and chip thickness. As a result, for each differential cutting edge element, corresponding orthogonal parameter were calculated and converted to the cutting coefficients in normal and friction directions individually. The list of shear parameters used in the mathematical model is given as:

$$\begin{aligned} \phi_n &= 19.4004 + 42.0174\, h + 0.02\, V + 0.3842\, \gamma_n \\ \tau_s &= 266.8047 + 174.1289\, h - 0.0437\, V + 0.8961\, \gamma_n \\ \beta_a &= 25.8772 - 1.2837\, h - 0.0075\, V + 0.1818\, \gamma_n \end{aligned} \tag{5.59}$$

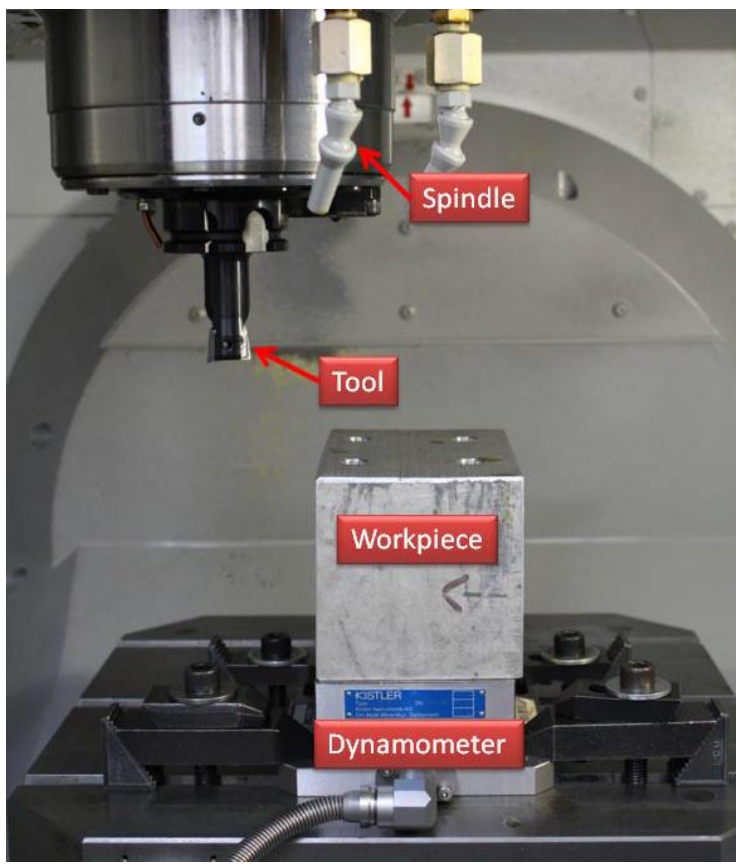

Figure 5-24: Workpiece and 3-Component Dynamometer Fixed to Machine Table for Cutting Tests.

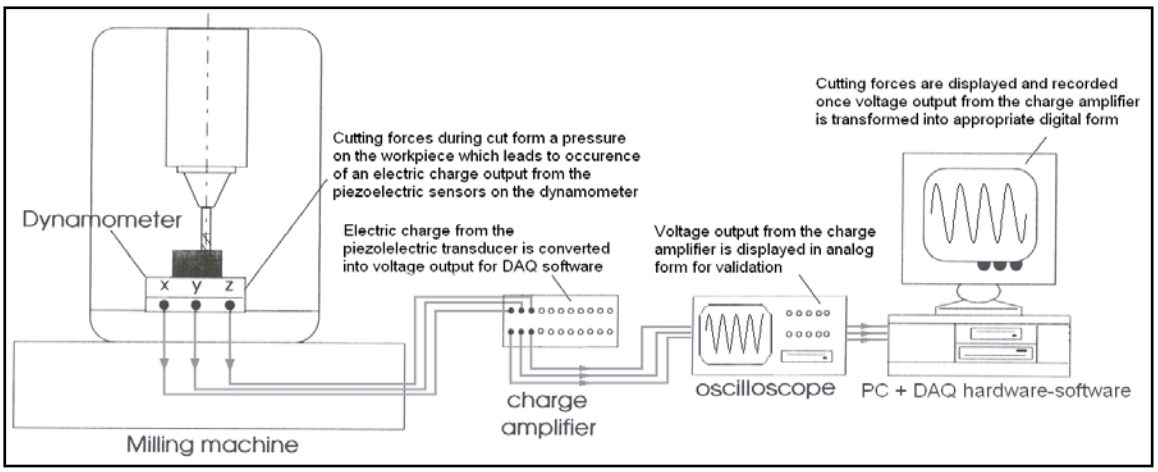

Figure 5-25: Illustration of the Experimental Setup for Measurement of Cutting Forces.

Shoulder End Mill with Rectangular Insert

A two fluted inserted cutter with built-in HSK holder and 25 mm diameter was selected. The cutter body is Sandvik R790-025HA06S2-16L and the inserts are R790-160408PH-PL with 16 mm insert length, 1 mm wiper edge, and 0.8 mm corner radius. Cutter body has 10° axial rake angle, 8° radial rake angle, and 90° cutting edge angle. Details of the cutter body can be seen in Figure 5-26.

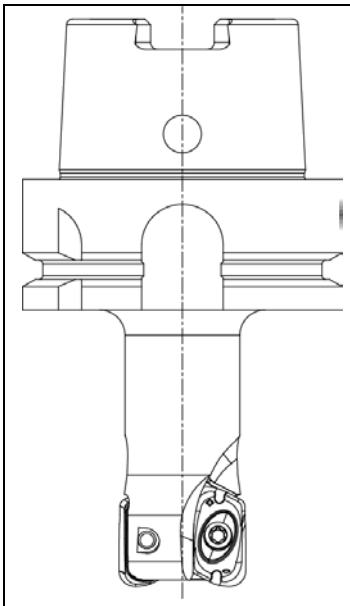

Tool	25 mm End Mill w/ 0.8 mm Nose Radius	
Axial Rake:	10°	
Radial Rake:	8°	
Insert Rake:	0°	
Insert Helix:	0°	
	Half Immersion	Full Immersion
Width of Cut:	12.5 mm	25 mm
Depth Of Cut:	4 mm	4 mm
Material:	Al7050-T541	Al7050-T541
Spindle Speed:	1500 rpm	2000 rpm
Feed Rate :	0.08 mm/tooth	0.1 mm/tooth

Figure 5-26: 25 mm Diameter Shoulder End Mill from Sandvik Coromant [55].

Control Points in global coordinate system (A, B, D, and E) (Figure 5-27):

$$\begin{aligned} A_x &= 11.2, \quad A_z = 0 \\ B_x &= 11.7, \quad B_z = 0 \\ D_x &= 12.5, \quad D_z = 0.8 \\ E_x &= 12.5, \quad E_z = 16 \end{aligned} \tag{5.60}$$

Using the orientation angles ($\kappa_r = 90°, \gamma_f = 10°,\ \gamma_p = 8°$), control points are transformed using Eq. (4.5). After the transformations, the locations of the control points become:

$$\begin{aligned} A_x &= 11.212, \quad A_y = -0.180, \ A_z = 0 \\ B_x &= 11.707, \ B_y = -0.111, \ B_z = 0 \\ D_x &= 12.480, \ D_y = 0.137, \quad D_z = 0.787 \\ E_x &= 12.113, \ E_y = 2.751, \quad E_z = 15.756 \end{aligned} \tag{5.61}$$

In this example there are two linear edges ($|AB|$ and $|DE|$) and one arc ($|BD|$). Therefore, two linear and one arc parametric equations are used:

$$\begin{aligned} P_{AB} &= \vec{P}_A + \left(\vec{P}_B - \vec{P}_A\right) t \ \ , \ \ 0 \le t \le 1 \\ P_{DE} &= \vec{P}_D + \left(\vec{P}_E - \vec{P}_D\right) t \ \ , \ \ 0 \le t \le 1 \\ P_{AB} &= \begin{bmatrix} 0.495\, t + 11.212 \\ 0.069\, t - 0.180 \\ 0 \end{bmatrix} \\ P_{DE} &= \begin{bmatrix} -0.367\, t + 12.480 \\ 2.613\, t + 0.137 \\ 14.969\, t + 0.787 \end{bmatrix} \end{aligned} \tag{5.62}$$

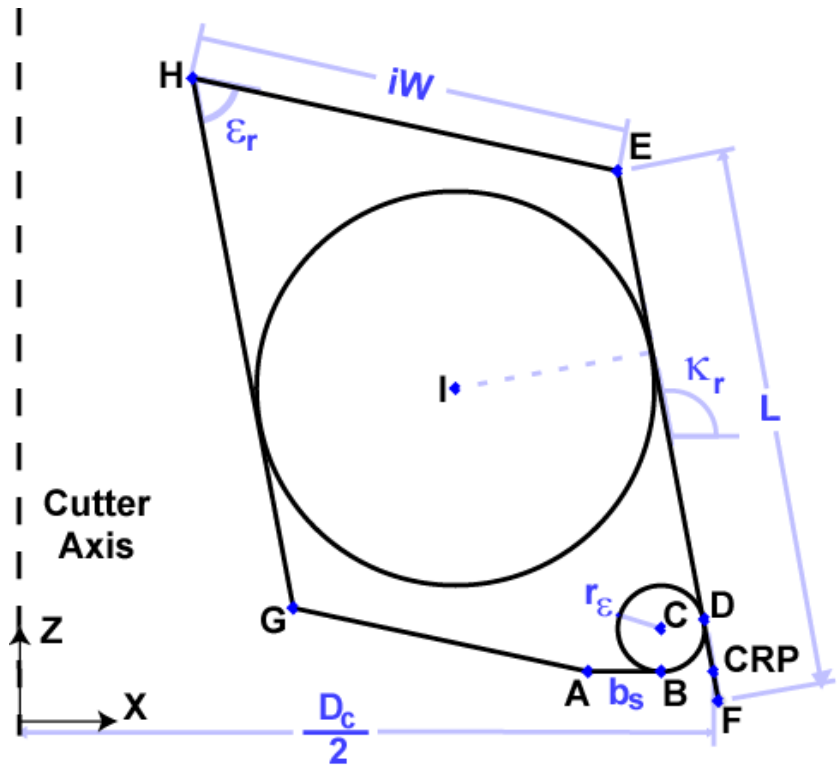

Figure 5-27: Illustration of Control Points for the Shoulder Milling Insert.

$$P_{BD} = R\cos t\,\vec{u} + R\sin t\;\vec{n}\times\vec{u} + C,\;\; 0 \le t \le \frac{\pi}{2}$$

$$R = 0.8, \qquad \vec{u} = \begin{bmatrix} 0.024 \\ -0.172 \\ -0.984 \end{bmatrix},\;\; \vec{n} = \begin{bmatrix} 0.137 \\ -0.975 \\ 0.173 \end{bmatrix},\;\; C = \begin{bmatrix} 11.688 \\ 0.026 \\ 0.787 \end{bmatrix} \tag{5.63}$$

$$P_{BD} = \begin{bmatrix} 0.019\cos t + 0.792\sin t + 11.688 \\ 0.111\cos t - 0.137\sin t + 0.0262 \\ 0.787 - 0.787\cos t \end{bmatrix}$$

Using P_{AB}, P_{BD}, and P_{DE}, local radii and physical angles of each selected point on the cutting edge were calculated and cutting forces were simulated with the same force model used in turning simulations. Validations of cutting forces were performed for half immersion up milling and full immersion slot cutting tests. In simulations, orthogonal parameters shown in Eq. (5.59) are used. The tests were conducted for different feed rates and spindle speeds. Cutting conditions for validation tests are summarized also in Figure 5-26. Simulated and experimental cutting forces are plotted versus time for two revolution of the tool in Figure 5-28 and Figure 5-29 for 4 mm axial depth of cut.

Although there was a forced vibration during cutting tests due to the vibration of the dynamometer, simulated cutting force patterns and their magnitudes showed very good agreement with the measurements. The tool was two fluted end mill, as a result two peaks can be observed in a single rotation of the tool. For consistency, cutting force of two rotations (720°) of the tool is presented for each width of cut.

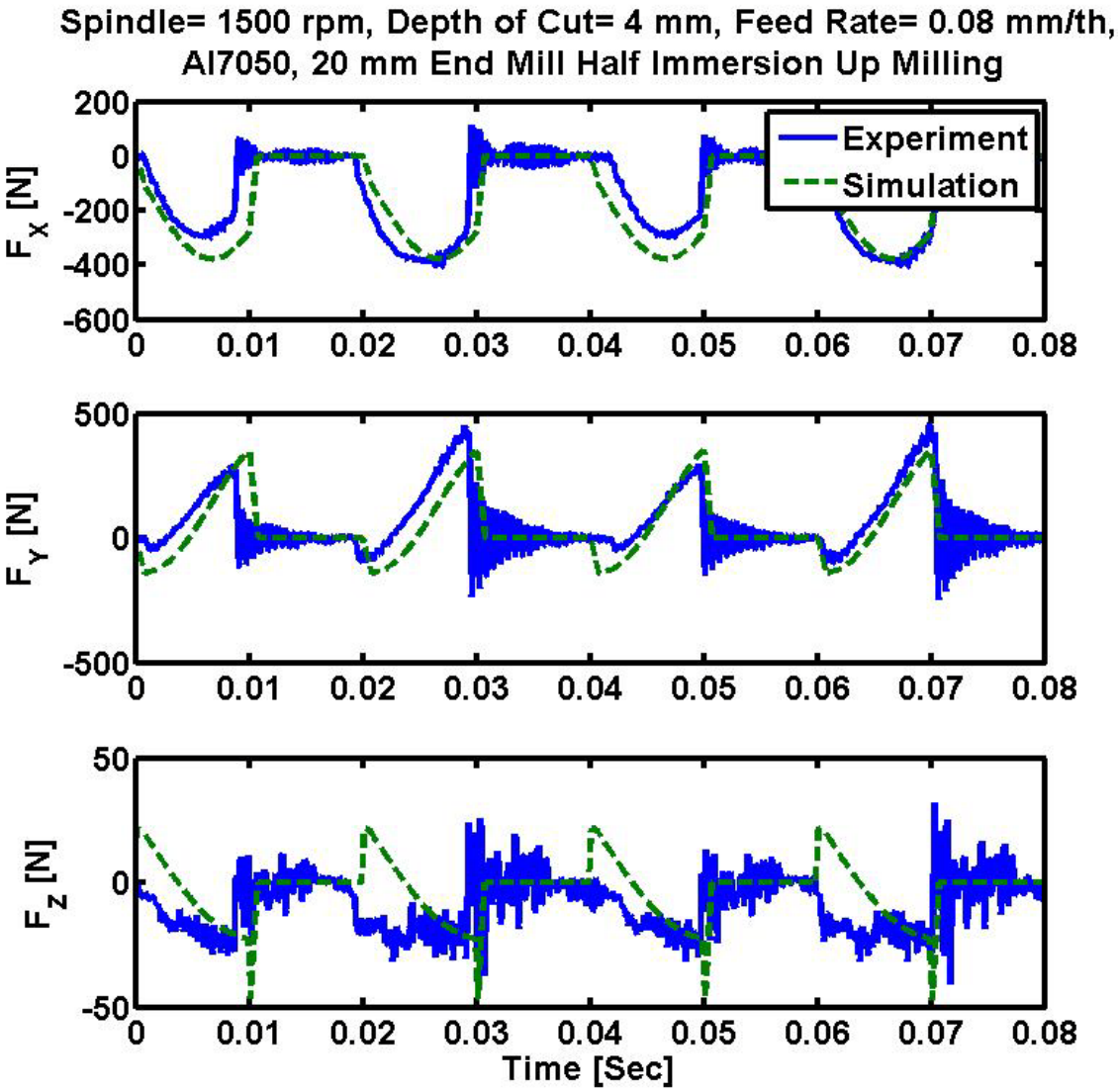

Figure 5-28: Measured and Predicted Forces for Al7050 Half Immersion Up-Milling.

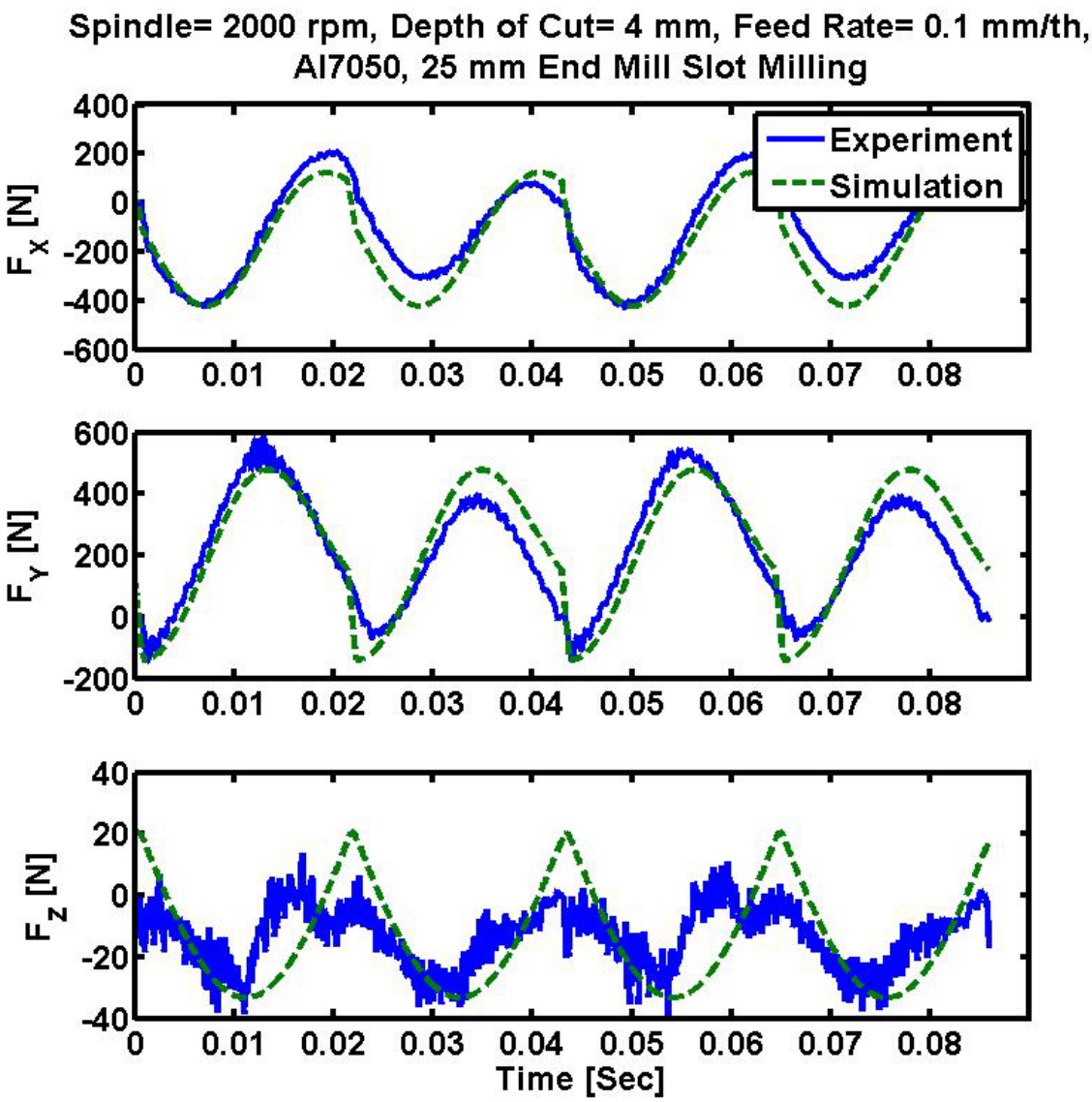

Figure 5-29: Measured and Predicted Forces for Al7050 Slot Milling.

Bull-Nose End Mill with Parallelogram Insert

In the second case, same workpiece (Al7050 – T451) was used to validate the cutting force model using a 20 mm diameter Sandvik R216-20B25-050 cutter with two flutes and two parallelogram inserts (Sandvik R216-20 T3 M-M 1025) with 10 mm nose radius. Cutter body has 10° axial rake angle and 5° radial rake angle.

For the sake of simplicity, control points and parametric equations are not shown in this insert; hence cutting edges are very similar to the shoulder end mill. Only difference between two inserts is that bull nose insert has a bigger corner radius. One slot milling and one half immersion up-milling tests were performed with different spindle speeds, feed rates, and depth of cuts. Cutting conditions are listed in Figure 5-30. Comparison of the measured and calculated cutting forces can be seen Figure 5-31 and Figure 5-32. It can be observed from the figures that the simulations and the experimental values are in good agreement; this proves that the cutting force model proposed in this chapter is valid not only for straight but also for round cutting edges.

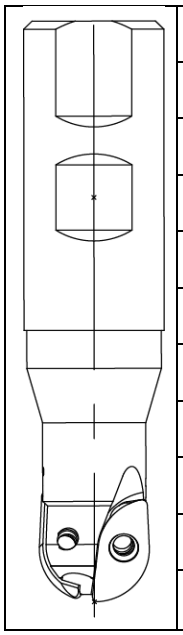

Tool	20 mm Bull Nose Mill w/ 10 mm Nose Radius	
Axial Rake:	12°	
Radial Rake:	5°	
Insert Rake:	0°	
Insert Helix:	0°	
	Half Immersion	Full Immersion
Width of Cut:	10 mm	20 mm
Depth Of Cut:	2 mm	3 mm
Material:	Al7050-T541	Al7050-T541
Spindle Speed:	2000 rpm	1000 rpm
Feed Rate :	0.1 mm/tooth	0.05 mm/tooth

Figure 5-30: 20 mm Diameter Bull-Nose Mill from Sandvik Coromant [55].

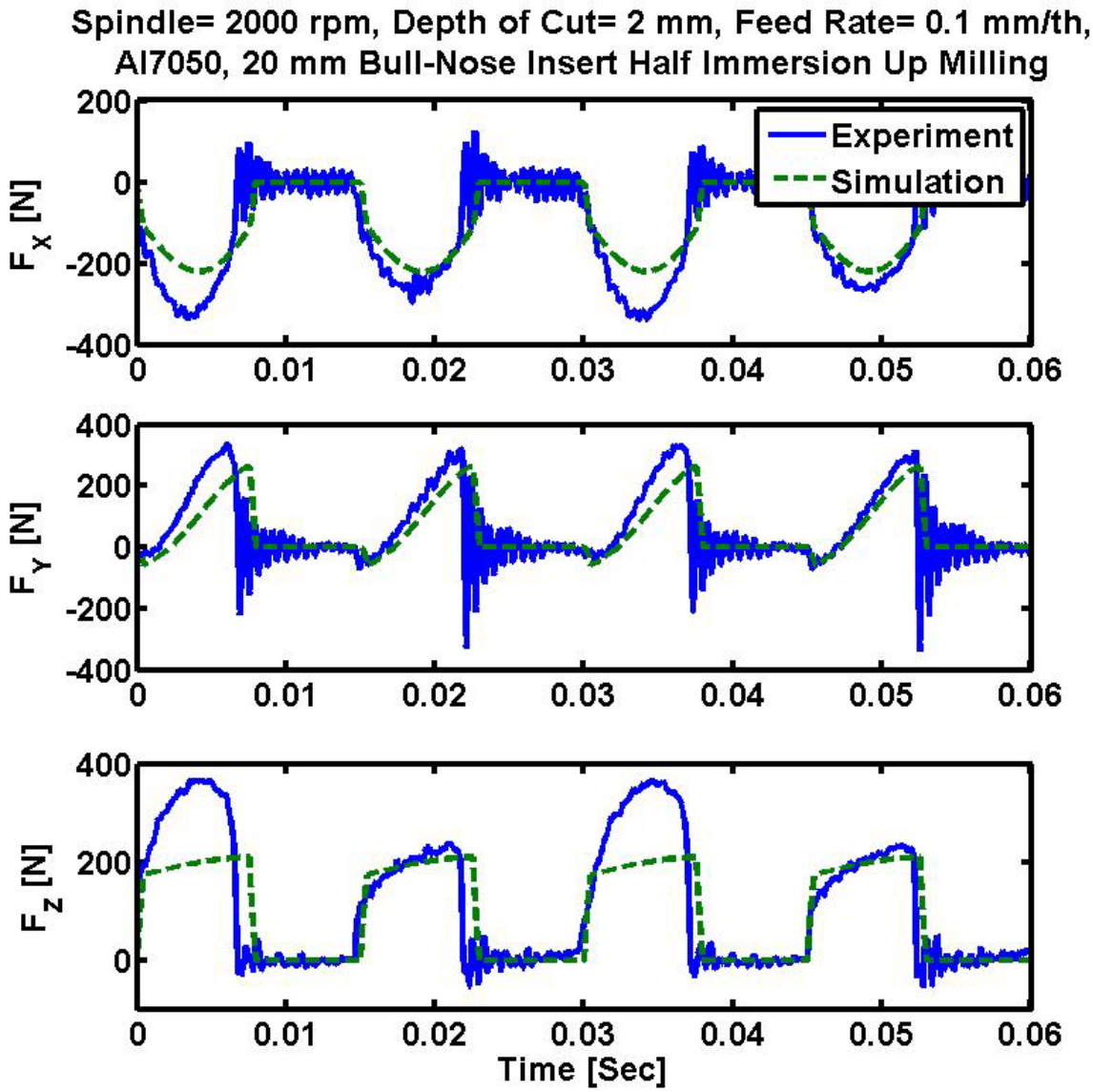

Figure 5-31: Measured and Predicted Forces for Al7050 Half Immersion Up-Milling.

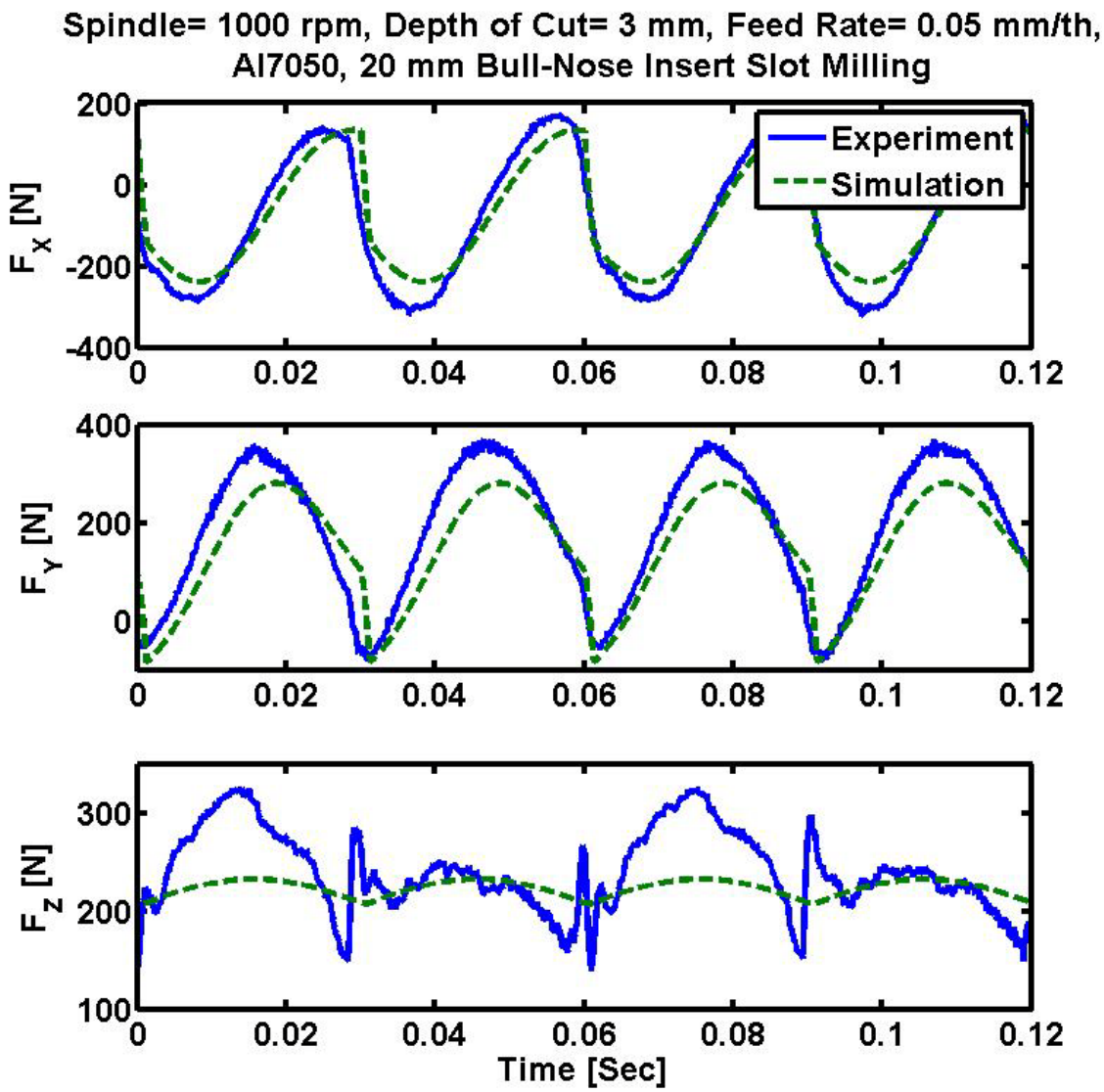

Figure 5-32: Measured and Predicted Forces for Al7050 Slot Milling.

Ball-End Mill with a Circular Insert

In the final case of milling validation tests, a ball end mill was selected with a circular (round) insert. Cutter body was Sandvik RF216F-20A20S-038, a 20 mm ball-end mill cutter. Unlike the other cutters presented in this section, this cutter has some unique properties. First of all, although it is a two fluted cutter, it has only one flat insert that cuts with both sides. Therefore, it does not have any axial or radial rake. The insert used with this cutter was Sandvik R216F-20 50E-L P10A circular insert with diameter of 20 mm.

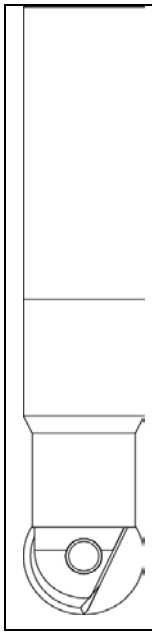

Tool	20 mm Ball End Mill	
Axial Rake:	0°	
Radial Rake:	0°	
Insert Rake:	0°	
Insert Helix:	0°	
	Half Immersion	Full Immersion
Width of Cut:	10 mm	20 mm
Depth Of Cut:	3 mm	3 mm
Material:	Al7050-T541	Al7050-T541
Spindle Speed:	5000 rpm	2000 rpm
Feed Rate :	0.1 mm/tooth	0.08 mm/tooth

Figure 5-33: 20 mm Diameter Ball-End Mill from Sandvik Coromant [55].

Control points in global coordinate system (A and B) (Figure 5-34):

$$A_x = 0, \quad A_y = 0, \quad A_z = 0$$
$$B_x = 10, \quad B_y = 0, \quad B_z = 10 \tag{5.64}$$

In this inserted cutter, since all orientation angles are 0°, the transformation matrices will be identity; therefore, the final positions of the control points do not change. There is only one parametric equation used in this type of insert:

$$P_{AB} = R\cos t\,\vec{u} + R\sin t\;\vec{n}\times\vec{u} + C,\;\; 0 \le t \le \frac{\pi}{2}$$

$$R = 10, \qquad \vec{u} = \begin{bmatrix} 0 \\ 0 \\ -1 \end{bmatrix},\;\; \vec{n} = \begin{bmatrix} 0 \\ -1 \\ 0 \end{bmatrix},\;\; C = \begin{bmatrix} 0 \\ 0 \\ 10 \end{bmatrix} \tag{5.65}$$

$$P_{AB} = \begin{bmatrix} 10\sin t \\ 0 \\ 10 - 10\cos t \end{bmatrix}$$

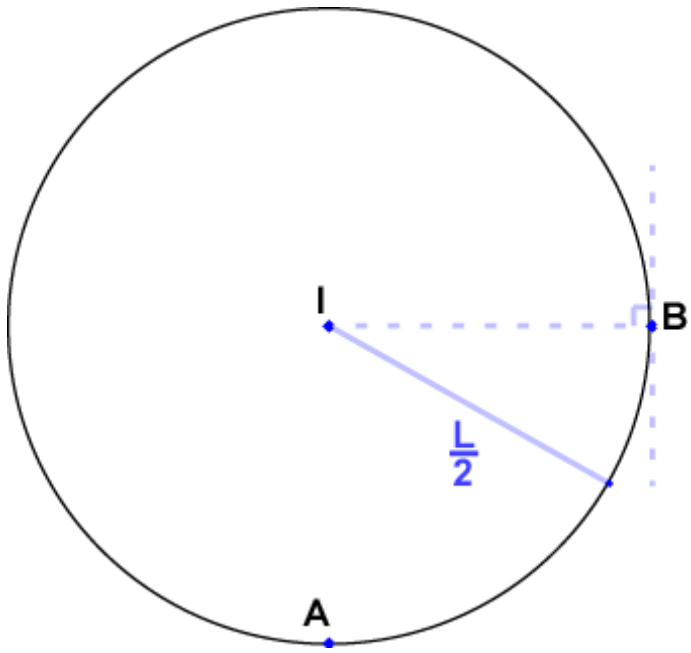

Figure 5-34: Control Points of a Round Milling Insert

By changing parameter t from 0 to 1, local radii and physical angles along the cutting edge can be determined. Similar to the previous milling examples, one half immersion and one full immersion slot milling tests were conducted with different spindle speeds and feed rates. Cutter geometry and tests conditions can be seen in Figure 5-33. Figure 5-35 and Figure 5-36 show the comparison of simulated values and experimental values. It can be noted that the measured and predicted cutting forces are found to be in good agreement.

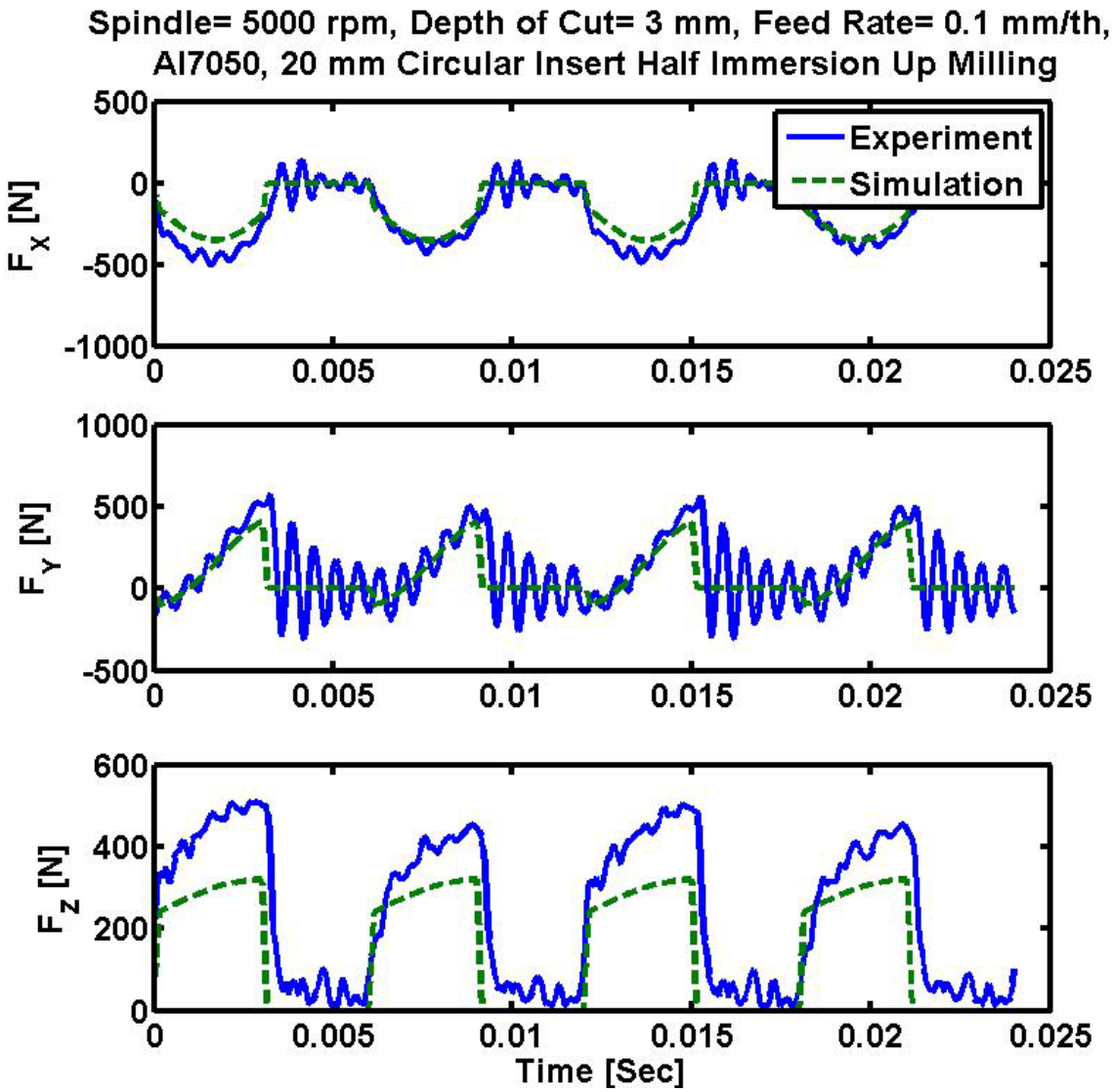

Figure 5-35: Measured and Predicted Forces for Al7050 Half Immersion Up-Milling.

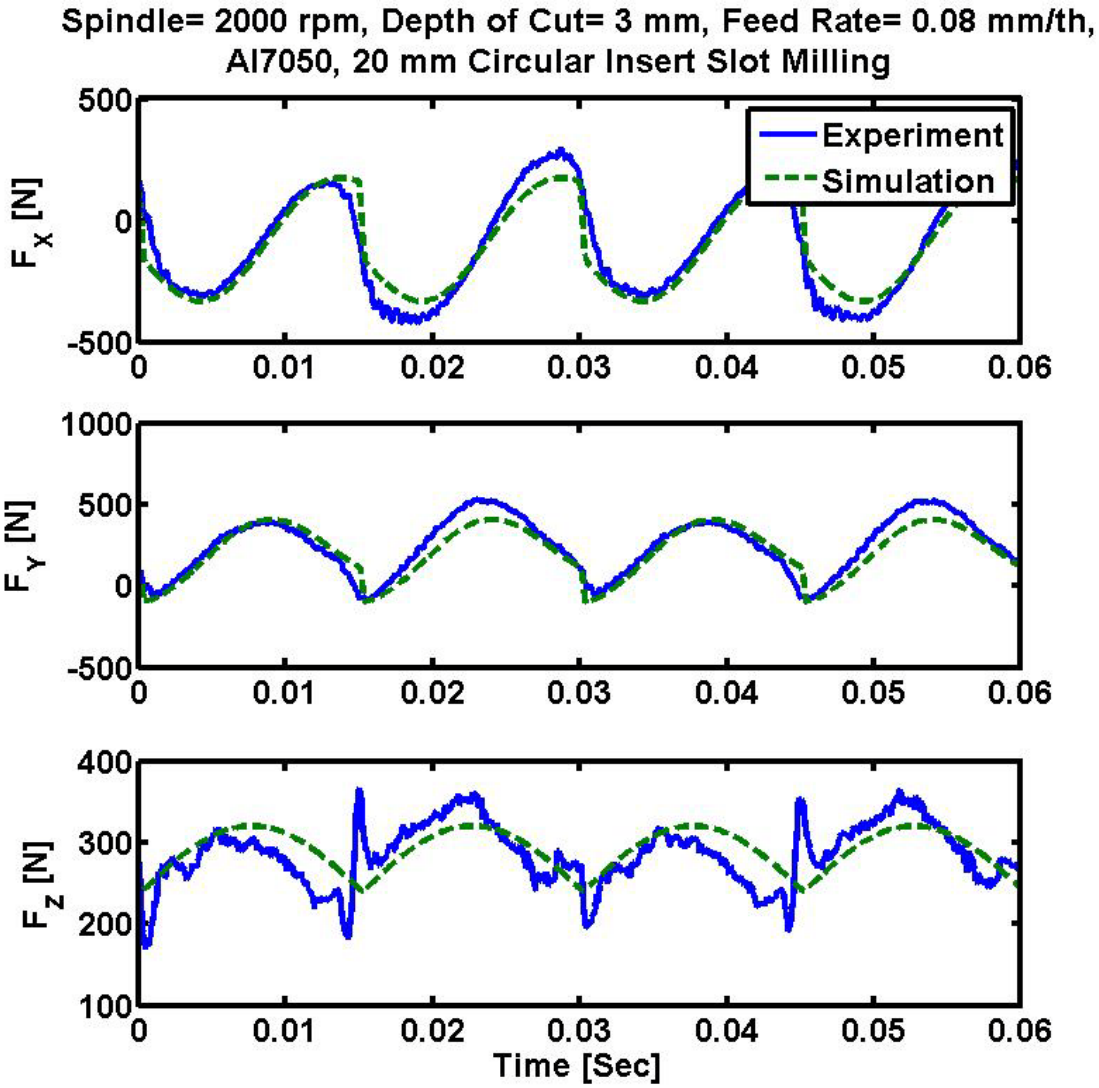

Figure 5-36: Measured and Predicted Forces for Al7050 Slot Milling.

5.5 Summary

In this chapter, generalized cutting mechanics and mathematical cutting force model for inserted cutters are presented. Mechanics model calculates the cutting forces on the rake face along the normal and friction directions. By doing so, it is possible to model any type of cutting process and tool geometry. This model also allows using any type of ISO insert as well as any insert with a custom shape. Proposed cutting force model is verified both in turning and milling operations using various tool geometries and cutting conditions.

6. Conclusions

The aim of this thesis has been to develop a generalized mathematical modeling of metal cutting mechanics which allows prediction of cutting forces for a variety of machining operations. The cutting forces are used to analyze torque, power and stiffness requirements from a machine tool. They are also primary variables in simulating and optimizing machining operations in virtual environment.

The proposed generalized model has three fundamental steps: 1) generalized geometric model of cutting tool based on ISO standards; 2) kinematic transformation of force vectors in machining systems; 3) and modeling of two principal cutting forces acting on the rake face of the tool. The two principal forces, namely the friction and normal forces on the rake face, are transformed to both cutting tool and machine tool coordinate systems. The generalized transformations allow the use of same material properties and rake face forces in predicting the loads in a variety of machining processes such as drilling, turning, boring, milling and other operations conducted with defined cutting edges.

The main contributions of the thesis can be summarized as follows:

- Instead of developing dedicated and tool geometry and cutting operation specific cutting force models as reported in the literature, an integrated geometric-mechanic and kinematic model of the process is presented. The model can be used to predict forces in various cutting operations with general tool geometry.
- A generalized geometric model of inserts and their placement on the tools have been developed using ISO standards for cutting tool geometry. The cutting edge coordinates, where the force is generated, are analytically evaluated from the common geometric model. The model allows the use of multiple cutting edges mounted on the cutter body. The required normal and oblique angles, which are needed in mechanics models, are evaluated analytically using general geometric model.

- The normal and friction forces on the rake face are used as the principal cutting forces. They are predicted either from orthogonal parameters (shear stress, shear angle and average friction coefficient) or empirical cutting force coefficients calibrated from mechanistic experiments. The principal cutting forces are transformed to both stationary and rotating tool coordinates depending on machining operations.
- Generalized coordinate transformation models are developed for both stationary and rotating tools. The cutting forces acting on the rake face are transformed to feed, normal and axial directions of the machine tool motion.
- The proposed general mechanics and geometric models are experimentally validated in turning and milling experiments with inserts having complex geometries.

The generalized mechanics model allow prediction of cutting forces, torque and power in a number of cutting operations conducted with tools having arbitrary geometries. The proposed model improves the computational efficiency and accuracy in simulating process physics and optimizing the operations in virtual machining of parts.

The most important limitation to the generalized cutting force model is the accuracy of the material model. Since the physical angles and cutting conditions significantly change along the cutting edge, material model (shear parameters or mechanistically determined cutting coefficients) should cover these changes. Otherwise, cutting coefficients will be extrapolated and simulated cutting forces will be inaccurate. This situation is already observed in the cutting force validations in Z direction.

The proposed model can be extended to drilling, boring, broaching, reaming and gear shaping in the future research. While boring, drilling and reaming require mainly extending the parametric definition of tool motion, the gear shaping and broaching require major effort in modeling the complex kinematics and tool geometries involved.

Bibliography

[1] S. Engin and Y. Altintas, "Mechanics and dynamics of general milling cutters. Part II: inserted cutters," *International Journal of Machine Tools & Manufacture*, vol. 41, p. 2213–2231, 2001.

[2] R. L. Kegg, "Cutting Dynamics in Machine Tool Chatter," *Transactions of the ASME*, pp. 464-470, November 1965.

[3] L. K. Lauderbaugh and V. Larson, "Multi-Input Discrete Time Force Model for Orthogonal Turning," *Precedings, ASME WAM, PED*, vol. 44, pp. 149-159, 1990.

[4] A. Stakhov and P. Viktor, *Metal Cutting Mechanics*.: CRC Press, 1999.

[5] Yusuf Altintas, *Manufacturing Automation: Metal Cutting Mechanics, Machine Tool Vibrations, and CNC Design*, 1st ed.: Cambridge University Press, 2000.

[6] A. E. Bayoumi, G. Yucesan, and L. A. Kendall, "An Analytical Mechanistic Cutting Force Model for Milling Operations: A Theory and Methodology," *Transactions of the ASME, Journal of Engineering for Industry*, vol. 116, pp. 324-330, 1994.

[7] M. E. Merchant, "Mechanics of the Cutting Process: Process I. Orthogonal Cutting and a Type 2 Chip," *Journal of Applied Physica*, vol. 16, pp. 267-275, 1945.

[8] M. E. Merchant, "Basic Mechanics of the Metal Cutting Process," *Journal of Applied Mechanics*, vol. 66, pp. 168-175, 1944.

[9] D. A. Stepheson and J. S. Agapiou, *Metal Cutting Theory and Practice*.: Marcel Dekker Inc., 1996.

[10] W. R. DeVries, *Analysis of Material Removal Processes*.: Springer - Verlag, 1992.

[11] E. Shamoto and Y. Altintas, "Prediction of Shear Angle in Oblique Cutting with Maximum Shear Stress and Minimum Energy Principles," *Journal of Manufacturing Science and Engineering*, vol. 121, no. 3, pp. 399-407, August 1999.

[12] E. M. Trent, *Metal Cutting*.: Butterworth-Heinemann Ltd., 1991.

[13] P.L. B. Oxley, *Mechanics of Machining: An Analytical Approach to Assesing Machinability*.: John Wiley & Sons, 1989.

[14] P.L. B. Oxley, W. F. Hastings, and M. G. Steven, "Predicting Cutting Forces, Tool Life, etc., Using Work Material Flow Stress Properties of Obtained from High Speed Compression Tests," in *Proceedings of International Conference on Production Engineering*, Tokyo, 1974, pp. 528-534.

[15] W. J. Endres, R. E. Devor, and S. G. Kapoor, "A Dual Mechanism Approach to the Prediction of Machining Forces, Part I & II," *Transactions of the ASME, Journal of Engineering for Industry*, vol. 117, pp. 526-541, 1995.

[16] E. H. Lee and B. W. Shaffer, "The Theory of Plasticity Applied to a Problem of Machining," *Journal of Applied Mechanics*, vol. 73, pp. 405-413, 1951.

[17] D. M. Eggleston, R. Herzog, and E. G. Thomsen, "Observations on the Angle Relationships in Metal Cutting," *Trans. ASME: Journal of Engineering for Industry*, pp. 263-279, 1959.

[18] L. DeChiffre, "Mechanics of Metal Cutting and Cutting Fluid Action," *International Journal of Machine Tool Design Research*, vol. 17, pp. 225-234, 1977.

[19] I. Yellowley, "A Simple Model of Orthogonal Cutting," *International Journal of Machine Tools Manufacture*, vol. 27, no. 3, pp. 357-365, 1987.

[20] P.L. B. Oxley, "A Strain Hardening Solution for the Shear Angle in Orthogonal Metal Cutting," *International Journal of Machine Tool Design Research*, vol. 3, pp. 68-79, 1961.

[21] A.J. P. Sabberwal, "Chip Section and Cutting Force during the Milling Operation," *Annals of the CIRP*, vol. 10, pp. 197-203, 1961.

[22] F. Koenigsberger and A. J. P. Sabberwal, "An Investigation into the Cutting Force Pulsations During Milling Operations," *International Journal of Machine Tool Design and Research*, vol. 1, pp. 15-33, 1961.

[23] C. Bus, N.A. L. Touwen, P. C. Veenstra, and A.C. H. VanDerWolf, "On the Significance of Equivalent Chip Thickness," *Annals of the CIRP*, vol. 19, pp. 121-124, 1971.

[24] I. Yellowley, "Observations on the Mean Values of Forces, Torques, and Specific

Power in the Peripheral Milling Process," *International Journal of Machine Tool Design and Research*, vol. 25, no. 4, pp. 337-346, 1985.

[25] L. V. Colwell, "Pridicting the Angle of Chip Flow for Single Point Cutting Tools," *Transactions of ASME*, vol. 76, pp. 199-204, 1954.

[26] K. Okushima and K. Minato, "On the Behavior of Chip in Steel Cutting," *Bulletin of JSME*, vol. 2, no. 5, pp. 58-64, 1959.

[27] G. V. Stabler, "The Fundemental Geometry of Cutting Tools," *Proceedings of the Institution of Mechanical Engineers*, pp. 14-21, 1951.

[28] H. T. Young, P. Mathew, and P.L. B. Oxley, "Allowing for Nose Radius Effects in Predicting Chip Flow Direction and Cutting Forces in Bar Turning," *Proc. Inst. Mech. Engrs*, vol. 201, no. 3, pp. 213-226, 1987.

[29] J. Wang, "Development of a Chip Flow Model for Turning Operations," *International Journal of Machine Tools and Manufacture*, vol. 41, no. 9, pp. 1265-1274, July 2001.

[30] E. Usui, A. Hirota, and M. Masuko, "Analytical Prediction of Three Dimensional Cutting Process: Part 1 Basic Cutting Model and Energy Approach," *Transactions of the ASME: Journal of Engineering for Industry*, vol. 100, pp. 222-228, 1978.

[31] E. Usui and A. Hirota, "Analytical Prediction of Three Dimensional Cutting Process: Part 2 Chip Formation and Cutting Force with Conventional Single Point Tool," *Transaction of the ASME Journal of Engineering for Industry*, vol. 100, pp. 229-235, 1978.

[32] M. E. Martelotti, "Analysis of the Milling Process," *Transactions of the ASME*, vol. 63, p. 677, 1941.

[33] M. E. Martelotti, "Analysis of the Milling Process," *Transactions of the ASME*, vol. 67, p. 233, 1945.

[34] J. Tlusty and P. McNeil, "Dynamics of Cutting Forces in End Milling," *Annals of the CIRP*, vol. 24, pp. 21-25, 1975.

[35] W. A. Kline, R. E. DeVor, and W. J. Zdeblick, "A Mechanistic Model for the Force System in End Milling with Application to Machining Airframe Structures," in *8th*

North American Manufacturing Research Conference, Dearborn, MI, 1980, p. 297.

[36] J. W. Sutherland and R. E. Devor, "An Improved Method for Cutting Force and Surface Error Prediction in Flexible End Milling Systems," *Transactions of the ASME, Journal of Engineering for Industry*, vol. 108, pp. 269-279, 1986.

[37] Y. Altintas and A. Spence, "End Milling Force Algorithms for CAD Systems," *Annals of the CIRP*, vol. 40, no. 1, pp. 31-34, 1991.

[38] E.J. A. Aramarego and N. P. Deshpande, "Force Prediction Models and CAD/CAM Software for Helical Tooth Milling Processes. I. Basic Approach and Cutting Analyses," *International Journal of Production Research*, vol. 31, no. 8, pp. 1991-2009, 1993.

[39] E.J. A. Armarego and C. J. Epp, "An Investigation of Zero Helix Peripheral Up-Milling," *International Journal of Machine Tool Design and Research*, vol. 10, pp. 273-291, 1970.

[40] E. Budak, Y. Altintas, and E.J. A. Armarego, "Prediction of Milling Force Coefficients from Orthogonal Cutting Data," *Journal of Manufacturing Science and Engineering*, vol. 118, no. 2, pp. 216-224, 1996.

[41] E.J. A. Armarego and R. H. Brown, *The Machining of Metals*. Englewood Cliffs, New Jersey: Prentice Hall, 1969.

[42] E.J. A. Armarego and R. C. Whitfield, "Computer Based Modelling of Popular Machining Operations for Force and Power Predictions," *Annals of the CIRP*, vol. 34, pp. 65-69, 1985.

[43] E. Budak and Y. Altintas, "Prediction of Milling Force Coefficients from Orthogonal Data," in *ASME Winter Annual Meeting*, New Orleans, 1993, pp. 453-459.

[44] S. Engin, "Mechanics and Dynamics of Milling with Generalized Geometry.," Istanbul Technical University, Istanbul, Ph.D. Thesis 1999.

[45] H. J. Fu., R. E. DeVor, and S. G. Kapoor, "A mechanistic model for the prediction of the force system in face milling operations," *Transactions of ASME, Journal of Engineering for Industry*, no. 106, pp. 81-88, 1984.

[46] H. S. Kim and K. F. Ehmann, "A Cutting Force Model for Face Milling Operations," *International Journal of Machine Tools & Manufacture*, vol. 33, no. 5, pp. 651-673, 1993.

[47] S. J. Kim, H. U. Lee, and D. W. Cho, "Feedrate Scheduling for Indexable End Milling Process Based on an Improved Cutting Force Model," *International Journal of Machine Tools & Manufacture*, vol. 46, pp. 1589-1597, 2006.

[48] F. Gu, S. N. Melkote, S. G. Kapoor, and R. E. DeVor, "A Model for the Prediction of Surface Flatness in Face Milling," *Journal of Manufacturing Science and Engineering*, vol. 119, no. 4, pp. 476-484, 1997.

[49] J. H. Ko and Y. Altintas, "Time Domain Model of Plunge Milling Operation," *International Journal of Machine Tools & Manufacture*, vol. 47, pp. 1351-1361, 2007.

[50] S. K. Choudhury and J. Mathew, "Investigations of the Effect of Non-uniform Insert Pitch on Vibration During Face Milling ," *International Journal of Machine Tools and Manufacture*, vol. 35, no. 10, pp. 1435-1444, October 1995.

[51] E.J. A. Armarego, "A Generic Mechanics of Cutting Approach to Predictive Technological Performance Modeling of the Wide Spectrum of Machining Operations," *Machining Science and Technology*, vol. 2, no. 2, pp. 191-211, 1998.

[52] E.J. A. Armarego, "The Unified-Generalized Mechanics of Cutting Approach - A Step Towards a House of Predictive Performance Models for Machining Operations," *Machining Science and Technology*, vol. 4, no. 3, pp. 319-362, 2000.

[53] ISO, "International Organization for Standardization - standard 3002/1-1982 Basic Quantities in Cutting and Grinding -- Part I & II," Geneva, 1982.

[54] ISO, "International Organization for Standardization. ISO -Standard 13399 -1:2006 Cutting Tool Data Representation and Exchange - Part I," ISO, Geneva, 2006.

[55] Sandvik Coromant, Main Catalogue, 2009.

[56] J. M. Selig, "Active Versus Passive Transformations in Robotics," *Robotics & Automation Magazine, IEEE*, vol. 13, no. 1, pp. 79-84, March 2006.

[57] J. Krystof, "Berichte uber Betriebswissenschaftliche Arbeiten, Bd.," VDI Verlag,

1939.

[58] E. Budak, "Mechanics and Dynamics of Milling Thin Walled Structures," The University of British Columbia, Vancouver, Ph.D. Thesis 1994.

[59] G. Yucesan and Y. Altintas, "Improved Modeling of Cutting Force Coefficients in Peripheral Milling," *International Journal of Machine Tools & Manufacture*, vol. 34, no. 4, pp. 473-487, 1994.

[60] R. Wertheim, A. Satran, and A. Ber, "Modifications of the Cutting Edge Geometry and Chip Formation in Milling," in *44th General Assembly of CIRP*, Singapore, 1994, pp. 63-68.

[61] M. E. Merchant, "Mechanics of the Cutting Process," *Trans. ASME Journal of Applied Mechanics*, vol. A, pp. 168-175, 1945.